UNIVERSITAT POLITÈCNICA DE VALÈNCIA

Instituto ITACA
Tecnologías de la Información y Comunicaciones

Microwave Dielectrometry Adapted to Environments

Ph. D. Thesis / Tesis Doctoral

by
José Daniel Gutiérrez Cano

Advisor:
José Manuel Catalá Civera

Thesis presented to obtain the PhD from the Universitat Politècnica de València

Valencia, June 2022

Acknowledgements

Con estas líneas completo otra etapa en la Universidad Politècnica de València, mi casa. Llegué a ella hace ya veinte años, desde un pequeño pueblo de la provincia de Albacete, Molinicos, con la ilusión de convertirme en ingeniero. Desde entonces, no he parado de visitarla casi a diario como estudiante, como trabajador, y como estudiante de doctorado y espero seguir en ella, trabajando e investigando, durante muchos años más. En estas líneas, me gustaría agradecer a todos aquellos que han formado parte de este proceso, aquellas personas que han estado a mi lado aconsejándome, ayudándome y apoyándome para la consecución de este trabajo.

En primer lugar, sin duda, me gustaría dar las gracias a mi director de tesis, José M. Catalá. Te agradezco de todo corazón la oportunidad que me diste al acogerme en el grupo de investigación DIMAS (ITACA-UPV) hace ya catorce años, han sido unos años extraordinarios. He aprendido muchísimo de ti, eres un referente tanto en lo profesional como en lo personal, un modelo a seguir. Te agradezco el apoyo y la confianza que me has demostrado durante todos estos años, y espero poder seguir junto a ti muchos años más. Me gustaría también expresar mi gratitud al resto de personas del grupo. A Felipe Peñaranda por su apoyo con los desarrollos teóricos, y a Pedro Plaza por su apoyo en el trabajo experimental, sois también un pilar fundamental de este trabajo. Al resto de compañeros, tanto a los que están en la actualidad, como a los que han decidido seguir otros caminos, gracias. Me llevo infinidad de momentos maravillosos. Ha sido un verdadero placer compartir este tiempo con todos vosotros.

Me gustaría terminar estos agradecimientos dedicando unas palabras a mi familia. A mis padres, José y Amparo, la base y razón de la persona que soy. De mi madre me llevo el cariño, y un ejemplo de tranquilidad y de trabajo en silencio. De mi padre, que sé que me está viendo desde ahí arriba, me llevo el ejemplo del trabajo, el esfuerzo y la responsabilidad. No sé cómo lo hicisteis, pero sólo deseo ser tan buen padre como lo habéis sido vosotros. Doy gracias todos los días por ser vuestro hijo, os quiero. A mi hermano, Juan Manuel, gracias por quererme y cuidarme en muchos momentos de mi vida; por tantos momentos en los que, aun siendo de edades tan diferentes, me has llevado en la mochila.

Leticia, simplemente gracias. Eres la persona más importante de mi vida, mi amor, mi amiga, mi confidente, la persona que me completa, eres una parte de mí mismo. Gracias por ayudarme, apoyarme y quererme en todo momento. Y a ti Sophie, eres el rayo de luz que ilumina mi vida, felicidad pura. Espero poder ser el padre que te mereces. Vivo por y para vosotras dos, os quiero y os querré siempre.

Financial support through the grant reference BES-2016-077296 of the call Convocatoria de las ayudas para contratos predoctorales para la formación de doctores de 2016 by Ministerio de Economía y Competitividad (MINECO) and by European Social Funds (ESF) of European Union is also gratefully acknowledged

Abstract

Permittivity is a physical property of materials describing their behavior in the presence of an electromagnetic field. Even though the permittivity of dielectric materials has been studied for many years, there is an increasing demand for novel characterization methods and devices in a considerable amount of scientific and industrial sectors.

Microwave sensors can play an essential role in detecting, monitoring, or process control tasks as some physicochemical parameters of materials produce measurable changes in dielectric properties. Besides, microwave heating technology is gaining increasing relevance for the ecological transition and decarbonization of industrial processes, and permittivity is the essential parameter for the successful development of these new processes. Permittivity depends on many factors, such as frequency, temperature, ionic content, density, or the presentation of the material. There is no universal method for determining dielectric properties under any condition; permittivity measurement methods must be adapted to the needs of the material and the measurement environment. Typically, microwave technology and dielectric characterization techniques are highly specialized processes requiring complex and expensive devices that have historically limited the expansion of these methods outside the telecommunications field.

The number of applications that require the monitoring or measurement of dielectric properties, the high dependencies of this magnitude under different conditions, and the need to make this technology available to a broader and less specialized user justify the development of this work.

This thesis aims to develop new devices for the monitoring and characterization of dielectrics adapted to different environments, covering a wide range of materials' formats, shapes, and properties. To achieve this purpose, this work aspires to devise easy-to-use and stand-alone systems to be employed in a wide range of situations, or specific cells addressing more particular requirements. The thesis dissertation is presented as a thesis by published papers, including four original contributions describing the most relevant aspects developed during my doctoral studies. A considerable effort during the thesis period was devoted to supporting the development of the research project SEDMICRON aiming to employ microwave technology as a new approach for the authentication of markers in document security applications through a near field scanning microwave microscope (NSMM).

The first two publications included in the thesis describe two different approaches to address permittivity measurements. The first paper describes a versatile, stand-alone, and easy-to-use instrument for measuring the permittivity of liquids, semisolids, powders,

granular, and solid materials inside pyrex tubes. The device is based on a resonant bi-reentrant cavity. The design of the cavity achieved an excellent sensitivity, and the study of the coupling network allowed the characterization of low, moderate, and high-loss materials with the same setup. This device included an in-house portable vector reflectometer, making it portable and cost-affordable. The features of the developed instrument allow straightforward use by non-specialized personnel and provide versatility in many situations. The second publication presents a specific cell design to cover a particular measurement need. In particular, this paper describes a test fixture based on an open-ended coaxial probe with increased sensitivity to determine the permittivity of lossy food products as a function of temperature at RF frequencies. This paper highlight the relevance of selecting the most suitable measurement technique, adapted to the environment and particularities of the material, for the appropriate determination of permittivity.

The following two papers describe the development and use of a near-field scanning microwave microscope with micrometric resolution to determine permittivity maps of heterogeneous planar materials at microwave frequencies. The different elements comprising the microscope instrument were described throughout both works: the sharp coaxial probe to perform the near-field measurements, included in a resonant structure; an in-house vector reflectometer to achieve stand-alone and easy-to-use functionality; the positioning subsystem to perform the pixel-by-pixel scanning; and the analysis techniques to determine permittivity values from the resonance measurements. In the first paper, microwave technology was employed for the first time in anti-counterfeiting applications by obtaining the dielectric mark of a banknote watermark. Besides, this study showed the ability of microwave energy to detect hidden marks behind dielectric or metallic layers, opening new possibilities for developing optically opaque security features untraceable by optical means. The second study demonstrates the versatility of this system in determining the dielectric properties of heterogeneous planar materials by measuring the dielectric response of rock specimens.

The methods developed in this thesis dissertation increase the portfolio of dielectric characterization systems and can help a wide range of scientific and industrial sectors in dielectric monitoring and characterization tasks, making these works more convenient and accessible.

Resumen

La permitividad es una propiedad física de los materiales que describe su comportamiento en presencia de un campo electromagnético. Aunque la permitividad de los materiales dieléctricos se ha estudiado durante muchos años, existe una creciente demanda de nuevos métodos y dispositivos de caracterización en una cantidad considerable de sectores científicos e industriales.

Los sensores de microondas pueden desempeñar un papel esencial en las tareas de detección, supervisión o control de procesos, ya que algunos parámetros fisicoquímicos de los materiales producen cambios medibles en las propiedades dieléctricas. Además, la tecnología de calentamiento por microondas está adquiriendo una relevancia creciente para la transición ecológica y la descarbonización de los procesos industriales, y la permitividad es el parámetro esencial para el desarrollo exitoso de estos nuevos procesos. La permitividad depende de muchos factores, como la frecuencia, la temperatura, el contenido iónico, la densidad o la presentación del material. No existe un método universal para determinar las propiedades dieléctricas en cualquier condición; los métodos de medición de la permitividad deben adaptarse a las necesidades del material y del entorno de medición. Normalmente, la tecnología de microondas y las técnicas de caracterización dieléctrica son procesos altamente especializados que requieren dispositivos complejos y costosos que históricamente han limitado la expansión de estos métodos fuera del ámbito de las telecomunicaciones.

El número de aplicaciones que requieren la monitorización o medida de las propiedades dieléctricas, las altas dependencias de esta magnitud bajo diferentes condiciones, y la necesidad de poner esta tecnología al alcance de un usuario más amplio y menos especializado, justifican el desarrollo de este trabajo.

Esta tesis pretende desarrollar nuevos dispositivos para la monitorización y caracterización de dieléctricos adaptados a diferentes entornos, cubriendo un amplio rango de formatos, formas y propiedades de los materiales. Para lograr este propósito, este trabajo aspira a idear tanto sistemas autónomos y fáciles de usar para ser empleados en un amplio rango de situaciones, como celdas específicas que aborden requerimientos más particulares. La tesis se presenta como una tesis por compendio de artículos, incluyendo cuatro contribuciones originales que describen los aspectos más relevantes desarrollados durante mis estudios de doctorado. Un esfuerzo considerable durante el período de la tesis se dedicó a apoyar el desarrollo del proyecto de investigación SEDMICRON, cuyo objetivo es emplear la tecnología de microondas como un nuevo enfoque para la autenticación de marcadores en aplicaciones de seguridad documental a través de un microscopio de microondas en campo cercano (NSMM).

Las dos primeras publicaciones incluidas en la tesis describen dos enfoques diferentes para abordar las mediciones de permitividad. El primer artículo describe un instrumento versátil, autónomo y fácil de usar para medir la permitividad de materiales líquidos, semisólidos, en polvo, granulares y sólidos dentro de tubos de pirex. El dispositivo se basa en una cavidad resonante bi-reentrante. El diseño de la cavidad logró una excelente sensibilidad, y el estudio de la red de acoplamiento permitió la caracterización de materiales de pérdidas bajas, moderadas y altas con una misma configuración. Este dispositivo incluye un reflectómetro vectorial portátil propio, lo que lo hace portátil y asequible. Las características del instrumento desarrollado permiten un uso sencillo por parte de personal no especializado y proporcionan versatilidad en muchas situaciones. La segunda publicación presenta el diseño de una celda específica para cubrir una necesidad de medición concreta. En particular, este artículo describe un dispositivo de prueba basado en una sonda coaxial de extremo abierto con una mayor sensibilidad para determinar la permitividad de productos alimenticios de altas pérdidas en función de la temperatura a frecuencias de RF. Este artículo destaca la importancia de seleccionar la técnica de medición más adecuada, adaptada al entorno y a las particularidades del material, para la determinación apropiada de la permitividad.

Los dos artículos siguientes describen el desarrollo y la utilización de un microscopio de microondas de campo cercano con resolución micrométrica para determinar mapas de permitividad de materiales planos heterogéneos a frecuencias de microondas. En ambos trabajos se describen los diferentes elementos que componen el instrumento del microscopio: la sonda coaxial afilada para realizar las mediciones de campo cercano, incluida en una estructura resonante; un reflectómetro vectorial propio para conseguir una funcionalidad autónoma y fácil de usar; el subsistema de posicionamiento para realizar el escaneo píxel a píxel; y las técnicas de análisis para determinar los valores de permitividad a partir de las medidas de los parámetros de la resonancia. En el primer trabajo se empleó por primera vez la tecnología de microondas en aplicaciones contra la falsificación, obteniendo la marca dieléctrica de la marca de agua de un billete. Además, este estudio demostró la capacidad de la energía de microondas para detectar marcas ocultas detrás de capas dieléctricas o metálicas, lo que abre nuevas posibilidades para el desarrollo de elementos de seguridad ópticamente opacos e imposibles de rastrear por medios ópticos. El segundo estudio demuestra la versatilidad de este sistema para determinar las propiedades dieléctricas de materiales planos heterogéneos midiendo la respuesta dieléctrica de especímenes de roca.

Los métodos desarrollados en esta tesis aumentan la cartera de sistemas de caracterización dieléctrica y pueden ayudar a una amplia gama de sectores científicos e industriales en las tareas de monitorización y caracterización dieléctrica, haciendo estos trabajos más cómodos y accesibles.

Resum

La permitivitat és una propietat física dels materials que descriu el seu comportament en presència d'un camp electromagnètic. Encara que la permitivitat dels materials dielèctrics s'ha estudiat durant molts anys, existeix una creixent demanda de nous mètodes i dispositius de caracterització en una quantitat considerable de sectors científics i industrials.

Els sensors de microones poden exercir un paper essencial en les tasques de detecció, supervisió o control de processos, ja que alguns paràmetres fisicoquímics dels materials produeixen canvis mesurables en les propietats dielèctriques. A més, la tecnologia de calfament per microones està adquirint una rellevància creixent per a la transició ecològica i la descarbonització dels processos industrials, i la permitivitat és el paràmetre essencial per al desenvolupament reeixit d'aquests nous processos. La permitivitat depén de molts factors, com la freqüència, la temperatura, el contingut iònic, la densitat o la presentació del material. No existeix un mètode universal per a determinar les propietats dielèctriques en qualsevol condició; els mètodes de mesurament de la permitivitat han d'adaptar-se a les necessitats del material i de l'entorn de mesurament. Normalment, la tecnologia de microones i les tècniques de caracterització dielèctrica són processos altament especialitzats que requereixen dispositius complexos i costosos que històricament han limitat l'expansió d'aquests mètodes fora del àmbit de les telecomunicacions.

El nombre d'aplicacions que requereixen el monitoratge o mesura de les propietats dielèctriques, les altes dependències d'aquesta magnitud sota diferents condicions, i la necessitat de posar aquesta tecnologia a l'abast d'un usuari més ampli i menys especialitzat, justifiquen el desenvolupament d'aquest treball.

Aquesta tesi pretén desenvolupar nous dispositius per al monitoratge i caracterització de dielèctrics adaptats a diferents entorns, cobrint un ampli rang de formats, formes i propietats dels materials. Per a aconseguir aquest propòsit, aquest treball aspira a idear tant sistemes autònoms i fàcils d'usar per a ser emprats en un ampli rang de situacions, com a cel·les específiques que aborden requeriments més particulars. La tesi es presenta com una tesi per compendi d'articles, incloent quatre contribucions originals que descriuen els aspectes més rellevants desenvolupats durant els meus estudis de doctorat. Un esforç considerable durant el període de la tesi es va dedicar a donar suport al desenvolupament del projecte d'investigació SEDMICRON, l'objectiu del qual és emprar la tecnologia de microones com un nou enfocament per a l'autenticació de marcadors en aplicacions de seguretat documental a través d'un microscopi de microones en camp pròxim (NSMM).

Les dues primeres publicacions incloses en la tesi descriuen dos enfocaments diferents per a abordar els mesuraments de permitivitat. El primer article descriu un instrument versàtil, autònom i fàcil d'usar per a mesurar la permitivitat de materials líquids, semisòlids, en pols, granulars i sòlids dins de tubs de pirex. El dispositiu es basa en una cavitat ressonant bi-reentrant. El disseny de la cavitat va aconseguir una excel·lent sensibilitat, i l'estudi de la xarxa d'acoblament va permetre la caracterització de materials de pèrdues baixes, moderades i altes amb una mateixa configuració. Aquest dispositiu inclou un reflectòmetre vectorial portàtil propi, la qual cosa el fa portàtil i assequible. Les característiques de l'instrument desenvolupat permeten un ús senzill per part de personal no especialitzat i proporcionen versatilitat en moltes situacions. La segona publicació presenta el disseny d'una cel·la específica per a cobrir una necessitat de mesurament concret. En particular, aquest article descriu un dispositiu de prova basat en una sonda coaxial d'extrem obert amb una major sensibilitat per a determinar la permitivitat de productes alimentaris d'altes pèrdues en funció de la temperatura a freqüències de RF. Aquest article destaca la importància de seleccionar la tècnica de mesurament més adequat, adaptada a l'entorn i a les particularitats del material, per a la determinació apropiada de la permitivitat.

Els dos articles següents descriuen el desenvolupament i la utilització d'un microscopi de microones de camp pròxim amb resolució micromètrica per a determinar mapes de permitivitat de materials plans heterogenis a freqüències de microones. En tots dos treballs es descriuen els diferents elements que componen l'instrument del microscopi: la sonda coaxial esmolada per a realitzar els mesuraments de camp pròxim, inclosa en una estructura ressonant; un reflectòmetre vectorial propi per a aconseguir una funcionalitat autònoma i fàcil d'usar; el subsistema de posicionament per a realitzar l'escaneig píxel a píxel; i les tècniques d'anàlisis per a determinar els valors de permitivitat a partir de les mesures dels paràmetres de la ressonància. En el primer treball es va emprar per primera vegada la tecnologia de microones en aplicacions contra la falsificació, obtenint la marca dielèctrica de la marca d'aigua d'un bitllet. A més, aquest estudi va demostrar la capacitat de l'energia de microones per a detectar marques ocultes darrere de capes dielèctriques o metàl·liques, la qual cosa obri noves possibilitats per al desenvolupament d'elements de seguretat òpticament opacs i impossibles de rastrejar per mitjans òptics. El segon estudi demostra la versatilitat d'aquest sistema per a determinar les propietats dielèctriques de materials plans heterogenis mesurant la resposta dielèctrica d'espècimens de roca.

Els mètodes desenvolupats en aquesta tesi augmenten la cartera de sistemes de caracterització dielèctrica i poden ajudar a una àmplia gamma de sectors científics i industrials en les tasques de monitoratge i caracterització dielèctrica, fent aquests treballs més còmodes i accessibles.

Table of Contents

Chapter 1

Introduction

A broad spectrum of scientific and industrial disciplines needs a better understanding of materials' properties. Accurate measurements of these properties can provide scientists and engineers valuable information to develop and optimize their processes. In particular, permittivity is an essential property that describes the behavior of dielectric materials when exposed to electromagnetic irradiation.

Dielectric properties have been studied for a very long time [1]. Nevertheless, there is still a significant interest and high demand for new studies, methods, and devices that allow and facilitate permittivity measurement to new and specific materials The number of scientific publications per year related to dielectric properties continues to grow, with a remarkable acceleration during the last decade [2,3].

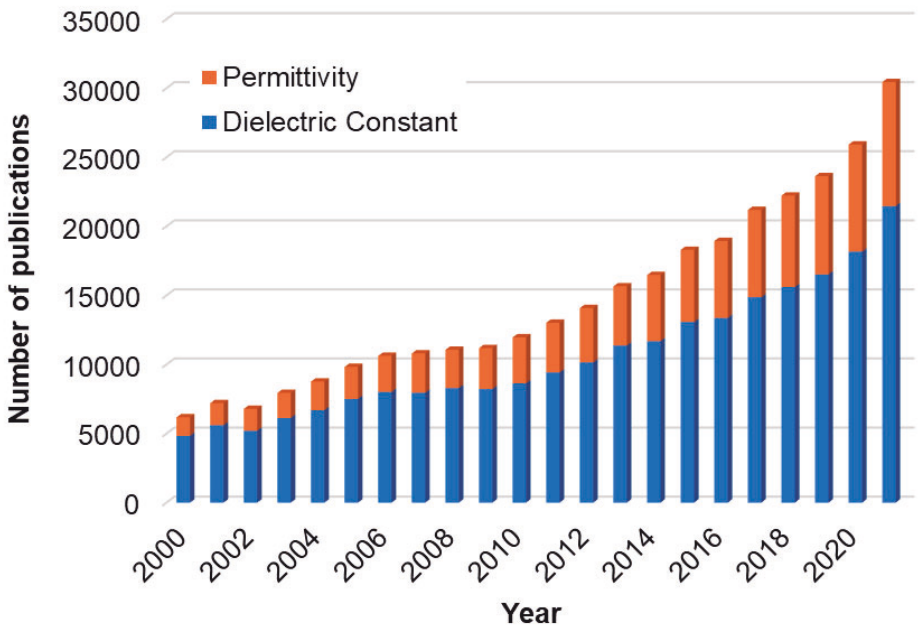

Fig. **1**: Number of scientific papers published in the period from 2000 to 2021 identified when searching for the words "dielectric properties" and "permittivity". Source: ScienceDirect [2,3]

Permittivity studies has been historically related to telecommunication engineering for selecting and evaluating the materials used in terrestrial and satellite communication systems, in elements such as waveguides, radomes, resonators, filters, or circuit boards [4]. Nevertheless, permittivity measurements and, in general, microwave sensors, have a high potential to be employed in many other applications.

There is a growing demand for sensors in many fields of knowledge to carry out detection, monitoring, or process control tasks. Microwave sensors can play an important role since some physicochemical parameters of materials produce measurable changes in dielectric properties, which can be correlated and indirectly measured by microwave techniques.

Since bound or free water is found in most materials, the radiofrequency and microwave sensors developed to measure moisture content are of great economic importance and have a very long history. The fast and accurate measurement of moisture content is a relevant element in different phases of production, storage, and processing of many natural products and raw materials. Microwave aquametry investigates the water content of solids and liquids by studying their response to electromagnetic fields at radio and microwave frequencies [5–7]. The dielectric properties of water are usually much higher than the permittivity of the majority of materials due to the high polarity of water, which enhances the sensitivity of microwave sensors to moisture measurements. Many research studies examine the relationship between the moisture content and the dielectric properties of agri-food materials, such as corn, wheat, barley, oats, or soybeans, and their moisture content [8–12].

Many other industries have also studied microwave-based sensors for moisture content determination in their processes. In the textile industry, the moisture content is relevant to monitoring product quality and reducing energy consumption, directly influencing the fabrics' strength, stiffness, and elasticity [13,14]. In the construction industry, monitoring the moisture content of fresh mixtures and the curing processes of cement pastes is critical for achieving reliable strength performance. But also, moisture has a significant impact on the durability and structure aging of concrete structures and thus, the development of new techniques for the early detection of structural degradation has become increasingly important [15–19]. In energy industries, the moisture content of wood biomass materials is an important factor in determining the net energy content and the overall quality of the product [20,21].

Apart from specific moisture sensors, there are numberless fields demanding permittivity measurements and novel microwave sensors. In medicine, several studies report the dielectric properties of biological fluids such as blood or urine, biological tissues such as skin or muscles, and organs such as the brain, the lungs, or the liver [22–31]. These studies are very important for developing new medical methods for therapy and diagnostics. In [32–35], the authors report some microwave sensors for glucose level monitoring, a critical health indicator related to health complications such as heart attack, stroke, blindness, or kidney disease. The early detection of cancer plays a crucial role in reducing the mortality rate. Consequently, many efforts are underway to develop new techniques for detecting breast or skin cancer through microwave technology [36–40].

Likewise, many other fields using dielectric properties or microwave technologies for different sensing purposes could be cited. In [41], the authors determined the dielectric properties of chlorinated water to assess the safety of drinking water by microwave-

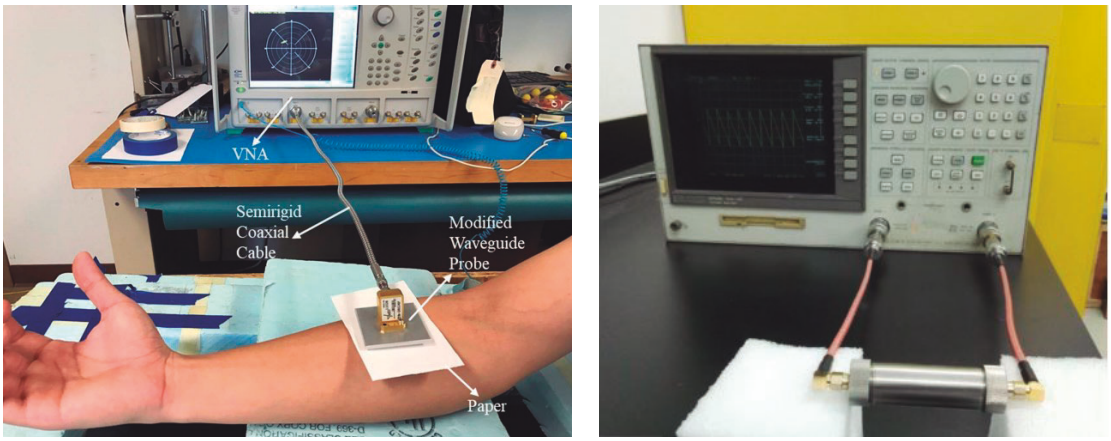

(a) (b)

Fig. **2**: Microwave sensors developments. (a) Open-ended rectangular waveguide for the in vivo measurement of skin dielectric properties [27]; (b) transmission line coaxial cell for the real-time monitoring of contamination in beach sand [42].

assisted technologies. The work in [42] described a rapid and non-destructive microwave-based technique to monitor the meta-cresol contamination levels of beach sand. In [43], a real-time microwave biosensor to detect and monitor subsurface bacterial growth was reported.

There are still many technological fields to be explored in which microwave technology could play an important role. Counterfeiting activities are constantly growing and constitute a severe threat to national economies and the safety of citizens. Technological advances have made counterfeiting techniques more readily available and increasingly sophisticated [44,45]. Thus, microwave technology can be an important yet unexplored tool in developing new methods to prevent and combat currency or document fraud.

Compared to other technologies, the distinct properties of microwave irradiation may provide substantial benefits in many sensing applications [6,46].

- Penetration depth is more significant compared to other technologies. Microwave energy can penetrate the material structure and achieve a volumetric assessment of the measured quantity.
- Microwaves allow non-destructive and non-invasive measurements. Depending on the measurement technique, physical contact between the sensor and the material may not be necessary.
- Microwave methods are safe. Sensors need low power levels, and, in contrast to ionizing radiation, the energy level of the radiation is much lower, so they do not pose a risk to human safety.
- Microwave sensors are relatively insensitive to environmental factors (dust, water vapor, etc.), which makes them especially suitable for implementation in industrial environments.
- Microwaves allow non-destructive measurements. Microwaves do not alter or contaminate the material, contrary to chemical methods.

However, some factors have limited the broad deployment of microwave sensors and permittivity measurement devices, among which the following can be highlighted [5,46,47]:

- High cost and large dimensions of the measurement systems. The dielectric probes and the devices for measuring the microwave response of such probes, typically vector network analyzers (VNA), are expensive.
- High degree of specialization required to manipulate the measurement devices and understand the devices' readings.
- Lack of standard designs. The sensors are typically developed for specific applications with low universal applicability.
- Microwave sensors are sensitive to permittivity changes, influenced by different variables, such as moisture content, grain size, density, or temperature. Specific analyses and studies are usually needed to correlate changes in permittivity with changes in a given variable.
- Acceptance of microwave technology. Even though microwaves are present in most applications in our daily life, there still exists concerns about the possible health hazards of this technology.

The remarkable growth in demand for permittivity measurements cannot be due the previous reasons alone. There is a growing interest in microwave technology as a clean, green, and sustainable technique to develop more efficient, fast, and eco-friendly heating processes. Global warming, the depletion of fossil fuels, the growing prices of energy, and the liberation of toxic wastes reinforce the need to find sustainable and renewable alternatives to fossil-derived products more critical than ever. Industries need to adapt their processes to the use of clean electricity with unconventional and environmentally-friendly heating mechanisms. The heat transfer in conventional heating technologies relies on radiation, surface convection, or internal conduction; microwave technologies involve a direct conversion of electromagnetic energy to thermal energy within the volume of the heated material [48,49]. This feature decreases processing times and reduces energy losses, resulting in lower energy consumption and operating costs. Microwave heating technologies have advantageous features such as high-power density, instantaneous temperature control, higher heating rates, process flexibility, or equipment portability [50]. In addition, permittivity variations within heterogeneous materials allow unique temperature distribution in the processed material (selective heating) which could be a significant advantage of microwave heating compared to conventional methods.

The food industry has traditionally used microwave technology in many applications in the food production chain. Cooking food using microwave techniques has been known, accepted, and used worldwide since Percy Spencer and Raytheon Manufacturing Company invented, patented, and built the first domestic microwave oven in the mid-20th century [51]. Cooking and food preservation are the primary purposes of food processing applications employing microwave or RF electromagnetic energy. Specifically, electromagnetic energy has been employed in thawing, baking, roasting, cooking, blanching, drying, pasteurization, or sterilization processes [52-62].

The number of studies in different fields of knowledge investigating the use of microwaves in their applications is huge. In the rock industry, microwave energy has been used in several applications, such as fracture or leaching [63,64]. In the

construction industry, microwaves have been employed to accelerate the curing times of concrete or decontaminate surfaces [65,66].

Microwave techniques have become increasingly popular in chemistry or pharmaceutical fields. Conventional heating techniques employed in synthesis processes are slow and inefficient. However, microwave energy instantly activates some of the molecules of the entire reaction mixture, improving product yields, reducing reaction times, and increasing productivity. Furthermore, microwave-assisted synthesis can promote reactions that are impossible with other heating technologies [67,68]. For instance, much attention has been paid to microwave synthesis of zeolite membranes for the remarkably synthesis time reduction and because microwave synthesis could lead to new morphology, orientation, composition, and performance characteristics [69–72]. Microwave sintering has also received increasing attention in recent years for similar reasons, including faster heating rates, lower sintering temperatures, shorter sintering times, and improved mechanical properties compared to conventional techniques. Microwave energy has been used in the sintering processes of ceramics, soils, metal powders, or metal matrix composites [73–80]. Microwave-assisted extraction has also been widely investigated in agriculture, healthy food, cosmetics, medical, or veterinary applications to improve chemical analysis techniques and obtain valuable compounds [81–88].

There is also great interest in the use of microwaves in the field of energy production and storage. Microwave-assisted pyrolysis is a promising bioconversion technique to produce bioenergy products from the treatment of plastic wastes, sewage sludge, lignocellulosic wastes, and other biomass residues and waste feedstocks [89–94]. Another relevant example is the work reported in [95]. The manuscript describes a contactless hydrogen production via water electrolysis triggered by microwave energy in a new reaction pathway allowing the process to occur at temperatures markedly lower than those required with other technologies.

(a) (b)

Fig. **3**: Microwave processing applications. (a) Microwave system setup for sintering of 3Y-TZP ceramics [80]; (b) Hydrogen production flowchart based on microwave reduction[95].

These lines highlight the relevance of microwave technology in addressing future challenges, underlining the importance of dielectric characterization today and in the years to come. Dielectric characterization of materials can bring value to many sectors and industries. Microwave sensors can play an essential role in detecting, monitoring, or processing control tasks. Besides, permittivity is a crucial parameter for developing new microwave heating methods for the ecological transition and decarbonization of industrial processes. The wide diversity of sectors interested in and needing permittivity characterization works compels the continuous evolution and development of new and easy-to-use methods adapted to their needs and working environments.

1.1 Fundamentals of Permittivity

This section aims to provide a general overview of permittivity, including its physical meaning and the conventions used throughout this thesis. Besides, the multiple dependencies of permittivity will be addressed.

The absolute permittivity ε is a fundamental electrical property describing the interactions between electromagnetic energy and materials [96]. The application of an electric field E to a dielectric material induces a polarization, increasing the displacement flux D.

$$\overline{D} = \bar{\bar{\varepsilon}} \cdot \overline{E} \tag{1}$$

Permittivity is a tensor relating both quantities, $\overline{E}$ and $\overline{D}$. This thesis will assume passive, reciprocal, and isotropic materials, reducing the tensor to a complex scalar, considering that permittivity is independent of the field orientation [4]. In some cases, this assumption would make it necessary to employ an effective permittivity. This term indicates that the strict definition of permittivity has been relaxed to some degree (presence of metals, heterogeneous materials, anisotropy, etc.) [97]. For instance, most food or agricultural materials are heterogeneous substances made up of elements with different permittivity values and, therefore, their complex permittivity is the effective permittivity of the mixture.

In the scientific literature, the complex relative permittivity ε_r is often used instead of the absolute permittivity quantity ε. It is a dimensionless complex quantity that can be expressed as:

$$\varepsilon_r = \varepsilon' - j\varepsilon'' = \varepsilon'(1 - \tan\delta) \tag{2}$$

where ε', ε'', and $\tan\delta$ are commonly known as the dielectric constant, the loss factor, and the loss tangent, respectively. The absolute permittivity, ε, can be calculated by multiplying the complex relative permittivity ε_r by the permittivity of free space, $\varepsilon_0 = 8.8542 \times 10\text{-}12$ F/m [98]. Throughout this thesis, ε_r will be referred to as dielectric properties, complex permittivity, or just permittivity.

The dielectric constant ε' is a measure of the “capacitivity”, the amount of energy from an external electric field stored in the material [49,99]. The minimum value of this parameter is 1, corresponding to the vacuum value. The dielectric constant of air is slightly higher, 1.0006, which is a negligible difference in most applications. It is important to point out that despite the commonly accepted name of dielectric constant, this quantity is not constant at all in most dielectric materials [98], as will be discussed in the following paragraphs.

The loss factor *ε''* describes the dissipative capabilities of the material, the amount of energy that goes into heat when irradiated by a varying electromagnetic field. Its minimum value is zero, which occurs in a lossless material. The loss tangent, defined as the ratio *ε''*/ *ε'*, is also a descriptive quantity depicting the material's ability to generate heat.

The basic elements composing dielectric materials are electrons, atoms, molecules, and ions, which are arranged within the material with a certain freedom of movement. The presence of a time-varying electromagnetic field induces the polarization of some of these constituent elements. The total permittivity is the result of all displacements happening at a certain frequency (see Fig. **4**). Permittivity is frequency dependent [49]. The dominant polarization effects at radio frequencies (RF) and microwave frequencies (MW) are the movement of dissolved ions and the rotation of molecules (relaxation processes).

In a complex material, there may be different relaxation processes happening simultaneously in the presence of an electromagnetic field, such as rotational, distortional, or interfacial polarization [98]. Let's consider a polar material like water. The thermal excitation induces a random orientation of dipoles in the absence of any external electromagnetic field. When an external electromagnetic field is applied to the dielectric material, the polar molecules tend to rotate to align themselves in a direction opposite to the electromagnetic field, appearing a net polarization (see Fig. **5**) [100].

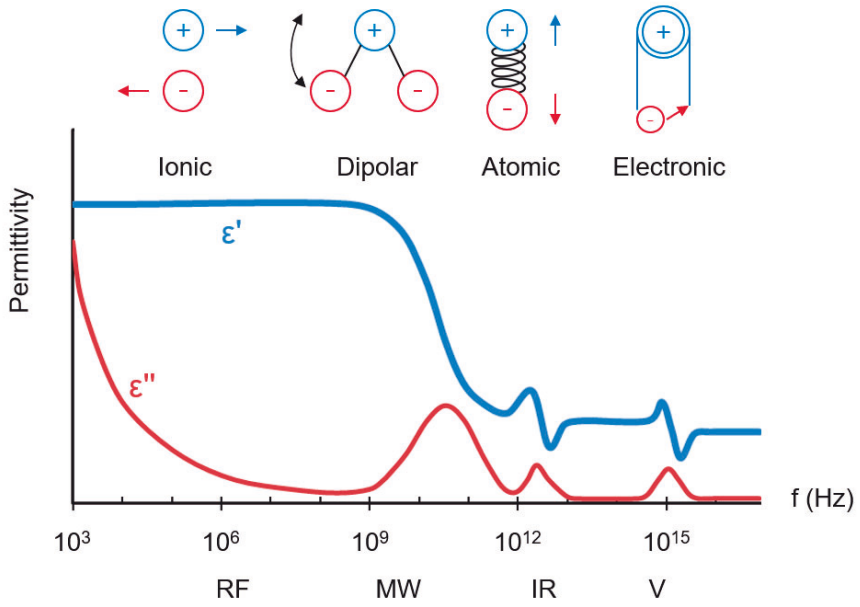

Fig. **4**: Influence of different polarization mechanisms on permittivity as a function of frequency.

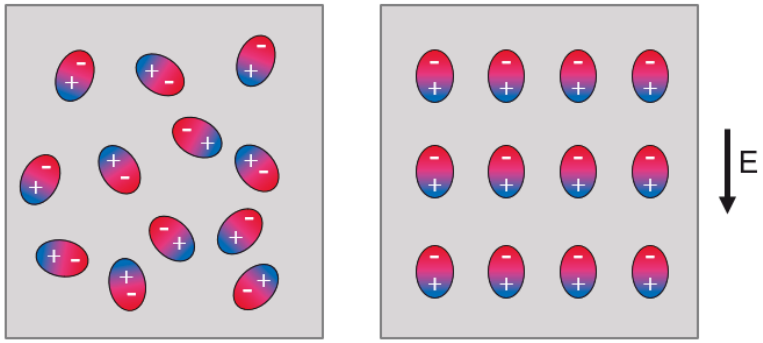

Fig. **5**: Dielectric material with polar molecules. (a) In the absence of an electromagnetic field. (b) In the presence of an electromagnetic field.

The behavior of the molecules, and thus the permittivity values, changes with the frequency of the external signal. At low frequencies, the molecules can easily rotate following the phase changes of the time-varying electromagnetic field, and most of the energy goes to storage, to ε'. However, as frequency increases and gets closer to the relaxation frequency f_{rel}, the molecules have trouble following the faster signal variations, ε' drops and the dielectric losses ε'' increase. At f_{rel}, the dielectric losses have the peak of this relaxation process. As frequency increases from f_{rel}, the dipoles are less and less able to keep up with the field's speed, and the contribution from this relaxation process to the total permittivity decay to zero [98]. Fig. **6**a shows this behavior for the example of deionized water, and Fig. **6**b shows the same data, but in a semi-circular trace commonly known as Cole-Cole diagram.

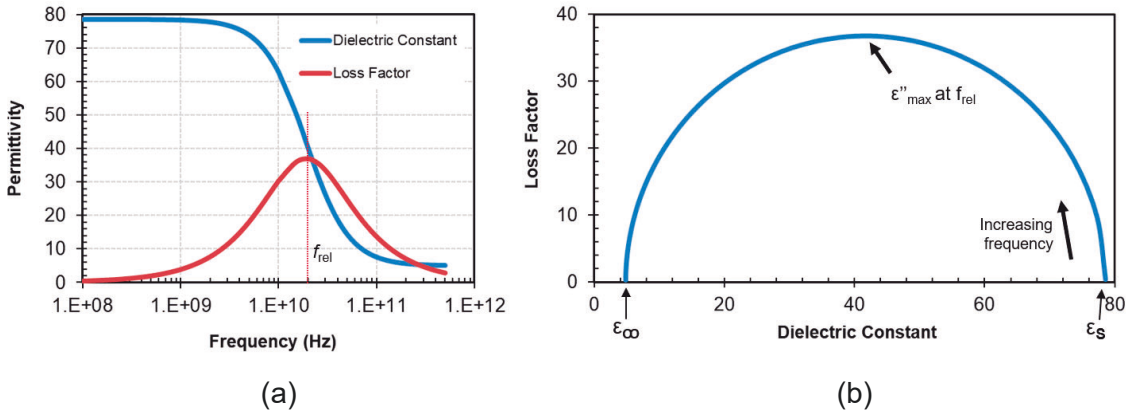

Fig. **6**: Permittivity behavior of deionized water: (a) permittivity as a function of frequency; (b) Cole-Cole diagram.

The simplest model to reproduce this response is known as Debye relaxation [98,101],

$$\varepsilon_r = \varepsilon_\infty + \frac{\varepsilon_s - \varepsilon_\infty}{1 + j\frac{f}{f_{rel}}} \tag{3}$$

where f is the frequency of the external signal, f_{rel} is the relaxation frequency, ε_s is the permittivity value at very low frequencies, and ε_∞ is the permittivity value at frequencies much higher than f_{rel}, without the influence of this relaxation process. The parameters defined in the Debye equation have been depicted in Fig. **6**a and **6**b. It is interesting to highlight that ε_s - ε_∞ is the contribution of this relaxation process to the total permittivity. Even though this model reproduces the response of deionized water, there are other models such as Cole-Cole, Cole-Davidson, Havriliak-Negami, or Multiple Debye [102–105] to adjust materials with multiple or more complex relaxation processes.

The influence of the movement of dissolved ions on permittivity differs from the behavior of relaxation processes. Fig. **7** shows the dielectric response of deionized water as a function of the frequency, as depicted in Fig. **6**a, together with the permittivity of saline water (1% salt content) [106]. Considering pure water and NaCl, the dipolar water molecules would manage to separate the NaCl structure into Na^+ and Cl^- ions, and all the ionic and molecular content restructures until they reach equilibrium. The ionic content reduces the value of the dielectric constant thanks to the new arrangement of water molecules in the resulting equilibrium. The dielectric losses increase due to the mobility of these free ions, or conductive charge carriers, under the presence of an alternating electromagnetic field [101]. The influence of the ionic content on the losses is especially relevant at low frequency as shown in Fig.**7**.

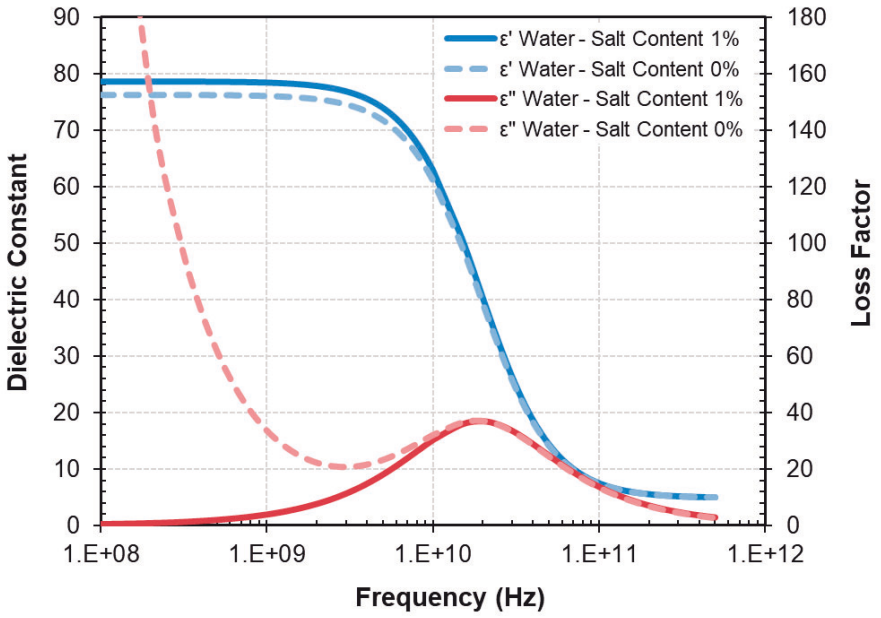

Fig. **7**: Permittivity of water with different NaCl concentrations as a function of frequency.

There are different conventions to consider the diverse loss sources, even though we could not distinguish between them when measuring at a single frequency [98]. This thesis will assume that the dielectric losses will be the total resulting from all the contributions. Thus, permittivity could be written as:

$$\varepsilon'' = \varepsilon''_D + \varepsilon''_\sigma = \varepsilon''_D + \frac{\sigma}{2\pi f} \tag{4}$$

where ε''_D are dipole losses, ε''_σ the ionic losses, and σ is the ionic conductivity. In short, frequency is possibly the element on which dielectric properties depend the most; the other is temperature. In general, considering a relaxation process, the relaxation frequency increases as the temperature increases. Thus, at a given frequency, the dielectric constant would increase with increasing temperature, and the loss factor would either increase or decrease, depending on whether the measured frequency is above or below f_{rel} [107]. Likewise, the ionic loss component increases with increasing temperature [101]. However, the actual temperature dependence in most complex materials should be obtained by measuring the material in the desired conditions.

Some other factors can also influence the permittivity of a given material. Even though these parameters are widely discussed in the literature, someone could consider that these permittivity changes are just simply because they are different materials. Permittivity depends on the moisture content (bound or non-associated water), the chemical composition (Salt or fat content), the density (mix air-material), the particle size, the homogeneity (effective permittivity), the viscosity, anisotropic effects, etc.

Permittivity describes the material behaviour in the presence of an electromagnetic field, the amount of energy it can store, and the amount of energy that can transform into heat. Permittivity depends on many factors, such as frequency, temperature, ionic content, density, or the presentation of the material. Such dependencies increase the need for new dielectric characterization methods and justify the continuous effort devoted to this end. This thesis aims to develop new devices for the monitoring and characterization of dielectrics adapted to different environments and particularities of the materials. To achieve this purpose, this work aspires to devise easy-to-use and stand-alone systems that may be employed in a wide range of situations, or specific cells that solve particular problems.

1.2 Vector Network Analyzers

Permittivity measurement techniques involve the connection of the test fixture to a measurement device called impedance analyzer or vector network analyzer (VNA) [99,108–110]. At microwave frequencies, the wavelengths become comparable or even smaller than the physical dimensions of the components. Hence, the behavior of the circuits changes with frequency, and the phase information becomes essential for the analysis of microwave circuits. The VNA is usually the most appropriate device to perform the measurements for permittivity characterization at microwave frequencies.

A network analyzer generates a microwave signal of a given frequency and launches it into a device under test (DUT). In our case, we consider the DUT to be a linear microwave circuit employed to characterize a dielectric material. Part of the input signal may reflect back, and other part may go forward. The reflected and transmitted signals

may differ from the input signal. The scattering parameters measure the amplitude and phase differences between the incident or reference signal and the reflected or transmitted waves. Fig. **8**a shows the scattering parameters of a typical two-port microwave circuit, where S_{11} is equivalent to the input complex reflection coefficient and S_{21} is the forward complex transmission coefficient. Then, the VNA changes the frequency of the incident signal and repeats the process to create a frequency sweep.

A simple schematic diagram of a VNA setup is shown in Fig. **8**b. This configuration comprises a microwave source, a separation network, receivers, and a processor that, together with the display, allows the results to be calculated and displayed. However, commercial VNAs are much more complex. For example, the standard block diagram of a heterodyne N-port VNA is shown in Fig. **9** [110].

Microwave technology and dielectric characterization techniques are highly specialized processes requiring complex and expensive devices that have historically limited the expansion of these methods outside the telecommunications field. Vector network analyzers are by far the most relevant contributor to this high cost and complexity. Among others, this thesis targets to overcome these limitations by creating stand-alone and easy-to-use systems for the dielectric characterization of materials. For that purpose, we designed a portable reflectometer and embedded it in some of the developments described in this work.

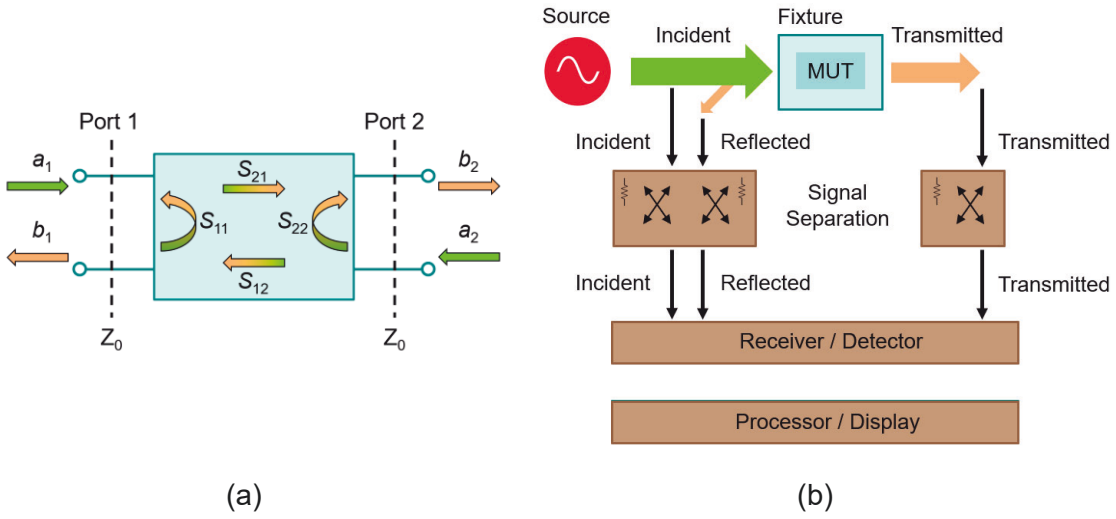

Fig. **8**: (a) Two-port device with its wave quantities and scattering parameters. (b) Simple Schematic of a Vector Network Analyzer

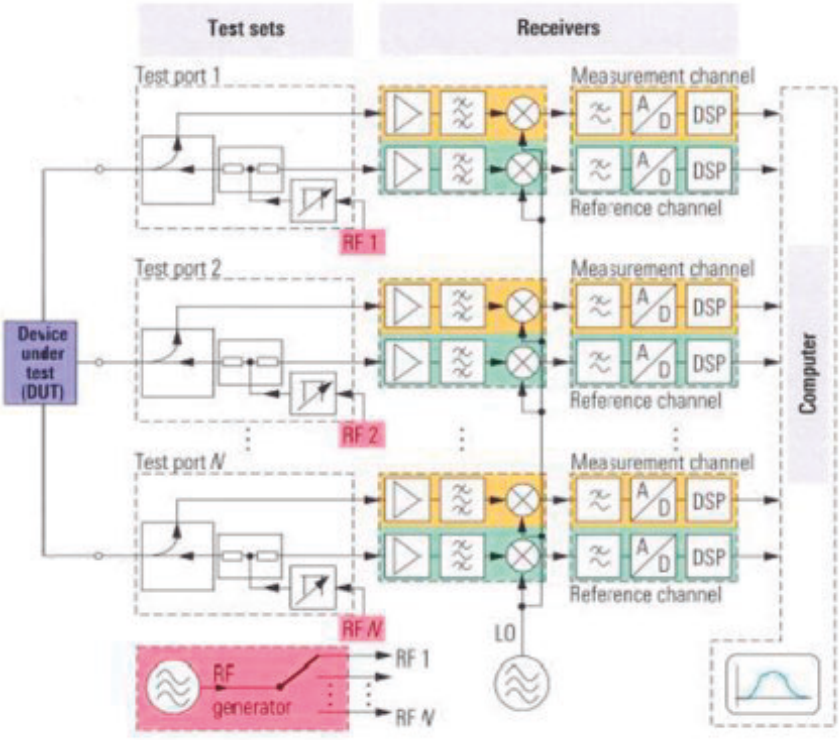

Fig. **9**: Block Diagram of a heterodyne N-Port Vector Network Analyzer [110].

1.3 Permittivity measurements techniques

Materials can be present in many formats, shapes, and properties. There are several factors to consider when selecting the most appropriate method to perform permittivity measurements, given the multiple dependencies of the dielectric properties and the vast number of measurement techniques available. This section aims to provide an overview of the most relevant techniques to characterize the dielectric properties of materials.

Permittivity values depend on the frequency, and thus, it is a fundamental aspect to consider. For instance, to ascertain the absorbing capabilities at the typical ISM frequency of 2.45GHz, it would suffice to know the permittivity at that single frequency. However, if we aim to select the frequency band with the best absorbing capabilities, it would demand measuring in a broader bandwidth. The dielectric losses of the material are also a fundamental parameter that largely conditions the election of the most suitable measurement technique among all available. But there are many more conditioning factors, such as the objective temperature, the needed accuracy, the hazardous risks, the state of the material (liquid, powder, semi-solid, solid), and its shape (round, planar, irregular), size, and homogeneity, etc.

A good number of scientific articles, review papers, books, commercial brochures, or technical notes report very detailed works explaining different techniques for permittivity characterization, diverse classification approaches, and some advice to select the most appropriate method for a measurement need [97–99,111–114]. In this small review, permittivity techniques will be divided into resonant and non-resonant methods, a typical

classification manner with significant differences in the frequency bandwidth, the losses of the material, and the accuracy.

1.3.1 Resonant methods

Resonators are microwave circuits that provide the best accuracy in terms of dielectric characterization, and thus, they are the most advisable techniques for the measurement of low-loss materials at discrete frequencies.

In a resonant structure, standing waves appear because of the interference between forward and reverse traveling waves, caused by the interaction of the waves with the boundary conditions of the structure [115]. Thanks to the back-and-forth movement of these waves, the interaction between the microwave energy and the dielectric material increases, boosting sensitivity, which improves the precision of the measurement, making resonant methods preferable for the permittivity characterization of low-loss materials [98].

The measurement of a resonant structure yields two fundamental parameters: the resonant frequency (f_r) and the quality factor (Q). The resonant frequency is the frequency at which the microwave structure can store energy. When a microwave signal with a frequency different from f_r is introduced into a resonant system, all the energy reflects to the input port. However, if the frequency of the introduced signal is equal to the resonant frequency of the structure, the cavity can store that microwave energy within its walls. Consequently, microwave resonators can perform permittivity characterization of material at a single frequency. In an actual resonator, there are losses. These losses come from different elements such as the conductivity of the resonator's walls, the dielectric losses of the measured material, or the external losses of the coupling network. The losses widen the response of the resonator; the resonator can also store energy at frequencies around the resonant frequency, but some energy is dissipated as heat. The measure of this widening and the assessment of the resonator's performance is the quality factor, which indicates the energy loss compared to the energy stored in the fields inside the resonator [116].

Nevertheless, the resonant frequency is not unique; there are several frequencies at which the system can store electromagnetic energy, resulting in resonant modes that differ in the number of field components and their pattern and direction. The dominant mode is the mode with the lowest resonant frequency, which is the one typically selected for permittivity measurements. Sometimes, the existence of additional high-order modes allows measurements at different frequencies. Still, mode density increases with frequency, which may hinder the identification of the appropriate mode and could originate significant errors due to mode coincidence and degeneracy. A different approach is to employ different sizes of the same microwave geometry, what would allow dielectric characterization by the dominant mode at different frequencies [98].

When a dielectric material is placed in a resonant structure, the resonant frequency, and the quality factor shifts (see Fig. **10**). The dielectric properties are obtained by relating the resonant frequency, the quality factor, and the geometry of the resonant structure using an electromagnetic model.

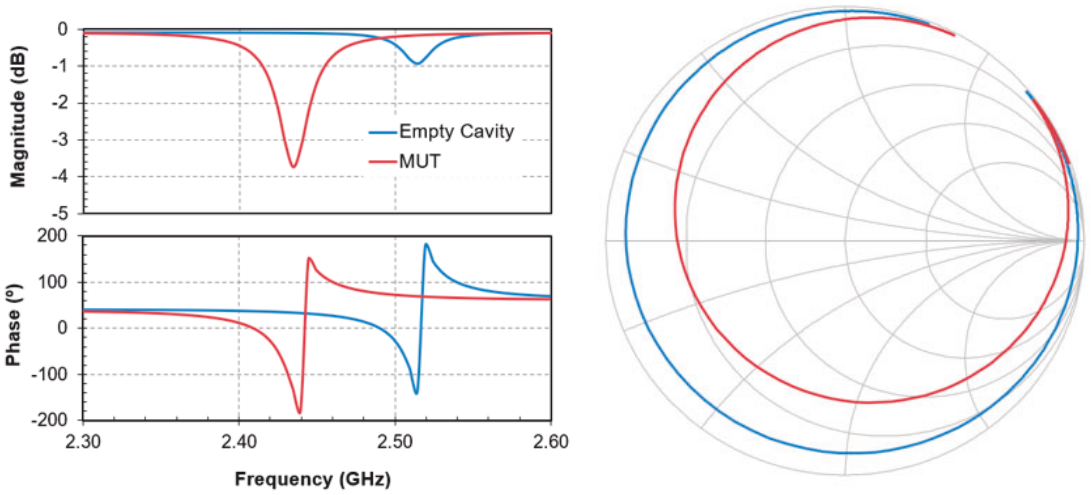

Fig. **10**: Resonant frequency and quality factor shifts in (a) Magnitude/phase plot and (b) Smith chart diagram.

A coupling network must be employed to introduce the microwave signal into the resonator and monitor its response for permittivity calculations [117]. This circuitry will influence both the resonant frequency and quality factor of the resonator. The typical approach for permittivity measurements consists of a transmission setup with very low coupling levels. The microwave signal is introduced through one port and collected through a different port, obtaining the scattering parameter S_{21}. In this case, the resonant frequency is directly the frequency of the maximum value of the S_{21}, and the quality factor can be determined as

$$Q = \frac{f_r}{\Delta f} \tag{5}$$

where f_r is the resonant frequency and Δf is the 3dB bandwidth [98]. Nevertheless, a reflection setup is also possible using the same port to introduce and monitor the microwave signal. In this case, the resonance retrieved with low coupling levels do not allow the use of Equation (5); a circular fitting procedure is frequently employed for this purpose [118]. In addition, several works have employed reflection measurements with high coupling levels to perform permittivity measurements of medium to high loss materials. In such a case, the influence of the external coupling network should be removed from the resonance measurements to determine the permittivity of the measured material properly [117–120].

Resonant methods include resonant cavities, open resonators, or dielectric resonators. Fig. **11** and **12** present a compilation of the most representative resonant techniques.

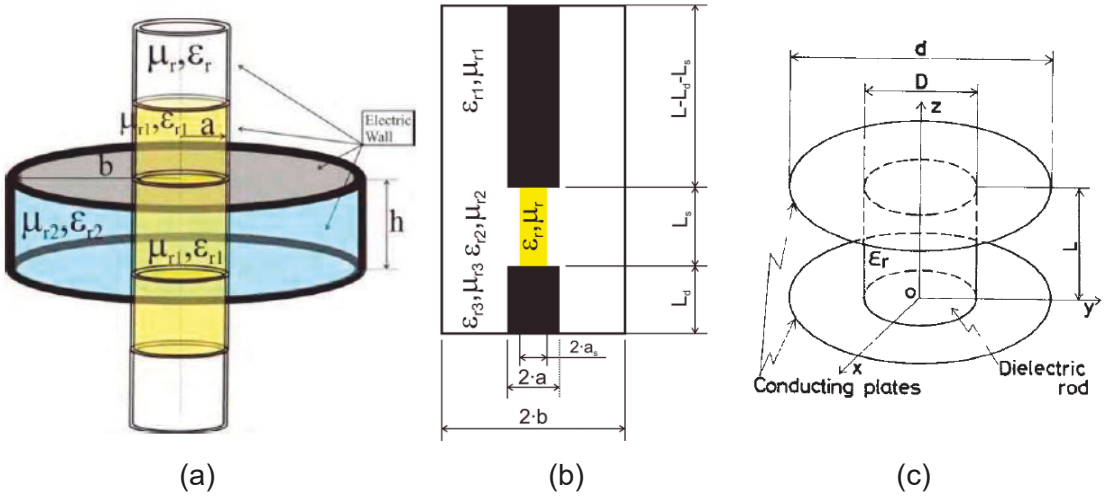

Fig. **11**: Resonant cavities for permittivity characterization of dielectric materials. (a) Cylindrical cavity [121]. (b) Re-entrant cavity structure [122]. (c) Dielectric resonator [123].

The closed cylindrical cavity (Fig **11**a) is one of the most versatile setups for permittivity characterization or process monitoring. The dominant mode changes depending on the relationship between the height and radius of the structure. In some cases, small holes can be drilled on the axis of the cavity to introduce samples, avoiding the use of lids. In addition, medium to high loss materials can be measured if the sample size is small enough to ensure a measurable Q factor. These features allow the measurement of a wide variety of circular elements, such as solid cylinders reaching from top to bottom of the cavity, circular laminar samples covering the entire width of the cavity, small size rods at the bottom of the cavity, liquid, or powder materials inside tubes, etc [121,124–127]. In [128], decoupled orthogonal modes were employed in the same closed cylindrical cavity to allow simultaneous dielectric characterization and microwave heating of rod samples inside a quartz tube.

Reentrant geometries have also been employed as a resonant method for dielectric properties determination. The typical setup consists of a short-circuited coaxial line with a gap in the central conductor to place the dielectric sample. The gap is set at one end in the single-post configuration [129] and in between the center conductor in the double-post structure [130]. The main advantage of this structure is the manageable size of the cavities to measure at frequencies below 1GHz, compared to other resonant methods. Since most of the energy in the cavity is stored in the capacitance gap, these structures are very sensitive to permittivity changes, being therefore ideal for dielectric characterization [98]. This technique has been typically employed to measure low-loss solid rods [122]. Nevertheless, some recent attempts have used this technique to measure medium to high loss liquids employing tubes crossing the axis of the structure [131].

Fig **12** show some of the most relevant methods specifically designed to characterize laminar materials, such as substrates or thin films. Fig. **12**a shows a Microstrip ring resonator, a technique with moderate accuracy that can obtain permittivity

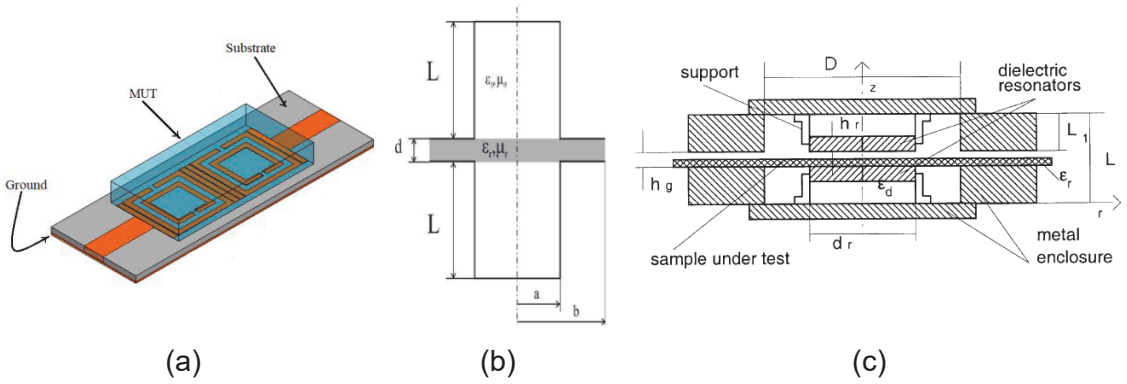

Fig. **12**: Resonant cavities for permittivity characterization of laminate materials. (a) Split ring resonator [134]. (b) Split Cylinder resonator [136]. (c) Split-post dielectric resonator [138].

measurements of laminar materials placed over some microstrip or stripline substrate geometries [132–134]. Fig. **12**b shows the geometry of a Split cylinder resonator, which consists of a cylindrical cavity split into two halves, in which the laminar material is placed [135][136]. This technique is more precise, but fields propagating outside the circular section can still lead to some inaccuracies. One of the most accurate methods for measuring laminar materials is presented in Fig. **12**c, the split-post dielectric resonator. It consists of two dielectric resonators achieving a strong evanescent electromagnetic field between them, which reduces the influence of the electromagnetic fields in the air gap [137–140].

The methods described in the previous paragraph are suitable for measuring permittivity of bulk laminate materials. Near-field probes are the preferable solution for heterogeneous laminate materials, achieving special resolutions shorter than the wavelength of the microwave signal employed [141,142]. Near-field radiation requires the size of the probe (the tip) to be smaller than the tip-to-sample distance and far shorter than the wavelength of the microwave signal, achieving spatial resolutions in the range of the size of the probe. Thereby, near field scanning microwave microscopes (NSMM) can determine the dielectric properties of inhomogeneous materials. Given the relevance of the tip-to-sample distance in the probe's response under the presence of a dielectric material, the use of a distance tracking element is usually necessary to allow permittivity characterization. Due to the rise of nanoscience and nanotechnology, most current devices try to achieve nanometric resolutions with complex setups, leaving aside many alternative applications that could require sensing systems and dielectric characterization at higher length scales [143].

Dielectric resonator and open resonator techniques follow different approaches for permittivity characterization. The dielectric resonator technique generates a resonant mode within a rod-shaped sample itself [123,144–147]. The method's sensitivity is superb because the electromagnetic fields are almost entirely inside the dielectric material, achieving a filling factor very close to 1. Thus, it is one of the most accurate methods for the dielectric characterization of low-loss material. The open resonator methods are typically employed to measure low-loss dielectrics at millimeter-wave frequencies with a free-field setup [148–150].

This thesis aims to cover the dielectric characterization of a wide range of formats and shapes of materials. In particular, the evolution of a bi-reentrant cavity was utilized to measure liquids, semi-solids, powders, granular and rod-shaped bulk solid materials, and a near-field microwave probe to characterize non-homogeneous planar materials. Although resonant transmission methods are the most widely employed, they are typically more complex, requiring more sophisticated measurement instrumentation and a higher degree of specialization. However, the autonomous devices in this work used a resonant reflection approach. The characteristics of resonant reflection methods make them very interesting for developing stand-alone devices with affordable and more straightforward instrumentation. Likewise, reflection methods with high coupling levels allow the characterization of low and high losses materials with the same setup.

1.3.2 Non-resonant methods

Non-resonant methods are based on analyzing the magnitude and phase changes in an electromagnetic signal transmitted or reflected by the material under test. For isotropic and non-magnetic materials, the permittivity can be determined by measuring the reflection or transmission parameter (S_{11} or S_{21}) of the microwave structure in which the material is placed [111]. These methods are often recommended for broadband measurement of high-loss materials and are generally less accurate than resonant methods. Non-resonant methods include waveguide cells, free-space techniques, and open-ended probes. It is relevant to highlight that some geometries can be adapted to be used in resonant or non-resonant setups [120,151].

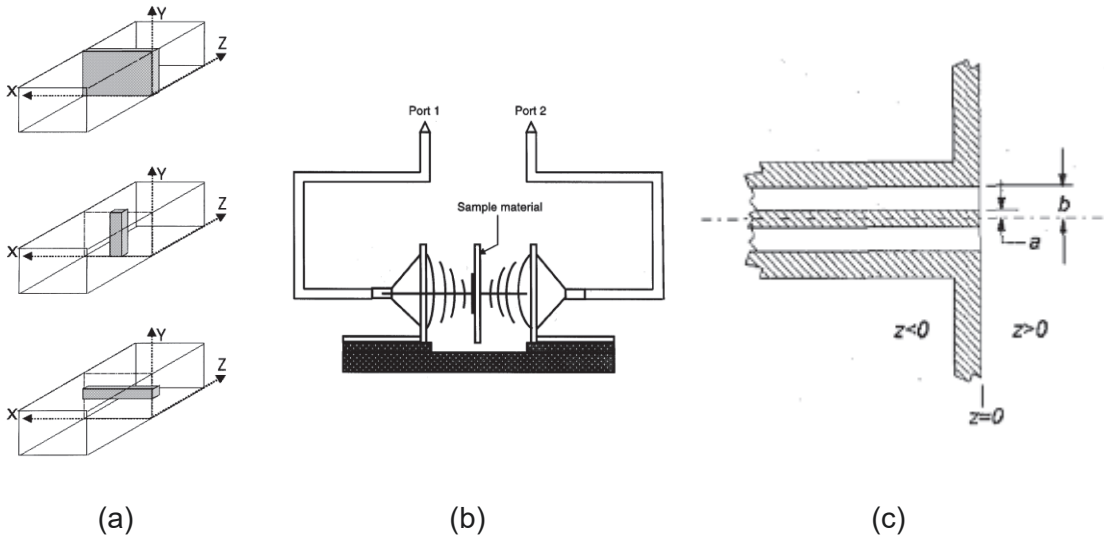

Fig. **13**: Non-resonant techniques for permittivity characterization of dielectric materials. (a) Partially filled rectangular waveguide [152]. (b) Free-space transmission technique [112]. (c) Open-ended coaxial probe [151].

Waveguide cell methods typically involve placing the material filling total o partially the cross-section of a coaxial or rectangular waveguide [113,152–154] and measuring the reflected and/or transmitted signal of the structure. Coaxial lines have the advantage of covering a large bandwidth, but the samples must be mechanized in the form of a toroid. In the case of rectangular waveguides, the frequency range is narrower, but rectangular-shaped samples are easier to manufacture [99]. Air gaps between the samples and the cavity walls reduce the accuracy of this technique, as remarked in the previous section [113].

Free space techniques employ the measurement of the reflection or transmission coefficients of two antennas that focus the microwave energy through the material under test [99]. This non-contact method allows high-temperature measurements in hostile environments. The technique requires the material to be large and flat compared to the electromagnetic beamwidth; thus, it is typically employed at millimeter-wave frequencies with the aid of concave mirrors or dielectric lenses to focus the beam [111,113].

Open-ended probes have been widely employed for permittivity characterization. Although the method's accuracy is limited [99,155], the open-ended coaxial probe has possibly become the most widely used method worldwide for the measurement of lossy dielectric materials. The method consists of measuring the reflection parameter of a coaxial line with an open end in contact with the material to be measured. Many features make the use of this probe advantageous in many situations. It is a broadband method that allows non-destructive measurements of planar solids, semi-solids, or liquid materials. However, some drawbacks of the technique should be considered. The technique usually employs liquids of known permittivity (normally deionized water) to calibrate the probe before measurements which may compromise the precision of the measurement. Air gaps between the sample and the probe aperture may lead to significant errors for solid and semi-solid materials. Likewise, air bubbles may hinder this kind of issue. The sample size must be big enough as the method assumes an infinite ground plane and sample size [99,151,156,157]. Although it is a relevant and valuable technique, it is often overused. Coaxial probes have been used in inappropriate situations, out of range, and claiming unrealistic accuracies.

Coaxial probes are the most widely used devices to determine permittivity of high losses materials, but they have reduced accuracy and may present measurement issues and inaccurate interpretation of results, primarily when used by non-specialist users. It is crucial to highlight the importance of adapting the measurement techniques to the environments and characteristics of the materials to avoid malpractice in the use of approaches that are not suitable for the multiple dependencies of permittivity, such as frequency, temperature, or dielectric losses. Given the importance of non-resonant methods and, in particular, the coaxial probe, this work presents a non-resonant open-ended coaxial probe adapted to a specific food environment, highlighting such relevant aspects.

1.4 Objectives

The thesis aims to study and develop methods for permittivity sensing and characterization adapted to different environments and covering a wide range of materials' formats, shapes, and properties. This work aims to create versatile, easy-to-use, and stand-alone devices for permittivity characterization of dielectric materials. Nevertheless, this work also addresses the design of measurement cells for specific applications.

This thesis has been financially supported through the grant reference BES-2016-077296 of the call Convocatoria de las ayudas para contratos predoctorales para la formación de doctores de 2016 by Ministerio de Economía y Competitividad (MINECO) and by European Social Funds (ESF) of European Union, and the project SEDMICRON—TEC2015-70272-R (MINECO/FEDER) supported by Ministerio de Economía y Competitividad (MINECO) and by European Regional Development Funds (ERDF) of European Union.

The project's objectives were part of the Spanish Strategy for Science, Technology, and Innovation within the Security, Protection, and Defence Challenge. One of the objectives of this challenge was the development of new aspects that reinforce security and defence capabilities. In particular, the project SEDMICRON focused on using a near-field scanning microwave microscope (NSMM) as a robust system for the detection, measurement, and authentication of micrometer-scale markers in document security applications.

In this context, the research activities in this Ph.D. aimed to support the development of this research project regarding the creation of the NSMM system and the development of microwave cells for the dielectric characterization needs of the project. Likewise, it aimed to go further and adapt the elements developed to other fields of knowledge, with a particular focus on reducing the limitations for using this type of sensor by non-specialized users. The specific objectives can be summarized in the following points.

- Develop a near-field scanning microwave microscope as a robust system for the authentication of markers in document security applications. This objective would require the achievement of the following goals:
    - Design microwave probes for near-field detection adapted to the application's needs.
    - Develop a microscopic platform with the necessary instrumentation for the near field measurement of 2D maps with micrometric resolutions.
    - Analyze the effect of the probe-sample distance on the robustness of the detection provided by the microscope.
- Increase the functionality of the microscope to allow measurements of complex permittivity of planar materials on a 2D micrometric scale and identify alternative applications that can benefit from the use of the developed microwave microscope.
- Develop permittivity measurement cells to allow the dielectric characterization of markers within the project framework.
- Identify alternative applications that can benefit from using these permittivity measurement techniques.

1.5 Thesis Structure

This thesis dissertation describes the work carried out to obtain the title of Ph.D. in Telecommunication Engineering under the Doctoral Program in Telecommunications of the Universitat Politècnica de València (UPV). The research has been conducted in the microwave division (DIMAS) of the Institute of Information and Communication Technologies (ITACA) of the Universitat Politècnica de València (UPV) under the direction of Prof. José M. Catalá-Civera.

This dissertation is devised as a thesis by published papers with the author's original contributions including the most relevant aspects developed during the doctoral studies. The document is structured in the chapters summarized below.

Chapter 1, Introduction, describes a general overview of the state of the art regarding permittivity measurements and techniques, together with the objectives and structure of the thesis.

Chapter 2, “A new stand-alone microwave instrument for measuring the complex permittivity of materials at microwave frequencies”, reproduces the first paper of the thesis. This work describes the development of a standalone and portable instrument based on a re-entrant cavity designed to measure the dielectric properties of materials inside pyrex tubes at microwave frequencies.

Chapter 3, “Improved open-ended coaxial probe for temperature-dependent permittivity measurements of foodstuff at radio frequencies “, presents the second paper of the thesis. This manuscript details the development of a test fixture to determine the permittivity of lossy food products as a function of temperature. The device includes a coaxial probe with increased sensitivity to be used at RF frequencies.

Chapter 4, “Detection of Anti-Counterfeiting Markers through Permittivity Maps Using a Micrometer Scale Near Field Scanning Microwave Microscope”, reproduces the third paper of the thesis. The work describes the different elements designed to create a standalone and portable Near Field Scanning Microwave Microscope at the micrometer scale developed to detect markers on anti-counterfeiting applications by means of permittivity maps.

Chapter 5, “High-Resolution Detection of Rock-Forming Minerals by Permittivity Measurements with a Near-Field Scanning Microwave Microscope”, features the fourth paper of the thesis. The manuscript extends the functionality of the microscope presented in chapter 4 to measure complex permittivity maps of planar materials. The system is utilized to detect permittivity maps of rock specimens.

Chapter 6, "General discussion", outlines the published results, describes the main contributions and achievements, and the degree of compliance of the objectives of the thesis.

Chapter 7, “Conclusions”, summarizes the most relevant results obtained in this thesis and foresees the prospects of future research lines.

1.6 References

1. Clark, F.M. The properties of dielectrics: Part II. The dielectric constant. *J. Franklin Inst.* **1929**, *208*, doi:10.1016/S0016-0032(29)90937-6.
2. Dielectric Properties articles, 2000-2021 Available online: https://www.sciencedirect.com/search?qs=dielectric properties&date=2000-2021 (accessed on Feb 12, 2022).
3. Permittivity articles, 2000-2021 Available online: https://www.sciencedirect.com/search?qs=permittivity&date=2000-2021 (accessed on Feb 12, 2022).
4. *Dielectric Materials for Wireless Communication*; Sebastian, M.T., Ed.; 1st edn.; Elsevier: UK, 2008;
5. Kraszewski, A.W. Microwave Aquametry -Needs and Perspectives. *IEEE Trans. Microw. Theory Tech.* **1991**, *39*, 828–835, doi:10.1109/22.79110.
6. Kraszewski, A. Microwave Aquametry: An Effective Tool for Nondestructive Moisture Sensing. *Subsurf. Sens. Technol. Appl.* **2001**, *2*, 347–362, doi:10.1023/A:1013212916645.
7. Nelson, S.O.; Trabelsi, S. Principles of grain and seed moisture sensing through radio-frequency and microwave dielectric properties. In Proceedings of the 2017 ASABE Annual International Meeting; American Society of Agricultural and Biological Engineers, 2017; pp. 1–13.
8. Nelson, S.O. Frequency and moisture dependence of the dielectric properties of high-moisture corn. *J. Microw. Power* **1978**, *13*, 213–218, doi:10.1080/16070658.1978.11689098.
9. Nelson, S.O. Factors Affecting the Dielectric Properties of Grain. *Trans. Am. Soc. Agric. Eng.* **1982**, *25*, 1045–1049, 1056, doi:10.13031/2013.33665.
10. Nelson, S.O. Frequency, Moisture, and Density Dependence of the Dielectric Properties of Small Grains and Soybeans. *Trans. ASAE* **1987**, *30*, 1538–1541, doi:10.13031/2013.30599.
11. Nelson, S.O.; Trabelsi, S. Dielectric properties of agricultural products. *IEEE Trans. Electr. Insul.* **1991**, *26*, 845–869, doi:10.1109/14.99097.
12. Lawrence, K.C.; Nelson, S.O.; Kraszewski, A.W. Temperature dependence of the dielectric properties of pecans. *Trans. Am. Soc. Agric. Eng.* **1992**, *35*, 251–255, doi:10.13031/2013.28596.
13. Li, P.; Wang, B.; Jing, J. The application of microwave detecting textile moisture content. *2010 Int. Conf. Intell. Comput. Technol. Autom. ICICTA 2010* **2010**, *3*, 706–709, doi:10.1109/ICICTA.2010.249.
14. Xiang, Z.; Wu, J.; Qi, C.; Hu, X. Contactless Detection of Moisture Content in Blended Fabrics with a Free-Space Microwave Method. *IEEE Trans. Instrum. Meas.* **2020**, *69*, 2139–2144, doi:10.1109/TIM.2019.2924065.
15. Al-Mattarneh, H.; Ghodgaonkar, D.; Majid, W.M. Microwave Sensing of Moisture Content in Concrete Using Open-Ended Rectangular Waveguide. *Subsurf. Sens. Technol. Appl.* **2001**, *2*, 377–390, doi:10.1023/A:1013217017554.

16. Jamil, M.; Hassan, M.K.; Al-Mattarneh, H.M.A.; Zain, M.F.M. Concrete dielectric properties investigation using microwave nondestructive techniques. *Mater. Struct. Constr.* **2013**, *46*, 77–87, doi:10.1617/s11527-012-9886-2.

17. Pavlík, J.; Tydlitát, V.; Černý, R.; Klečka, T.; Bouška, P.; Rovnaníková, P. Application of a microwave impulse technique to the measurement of free water content in early hydration stages of cement paste. *Cem. Concr. Res.* **2003**, *33*, 93–102, doi:10.1016/S0008-8846(02)00930-4.

18. Cataldo, A.; De Benedetto, E.; Cannazza, G. Hydration monitoring and moisture control of cement-based samples through embedded wire-like sensing elements. *IEEE Sens. J.* **2015**, *15*, 1208–1215, doi:10.1109/JSEN.2014.2360712.

19. Horsley, A.; Thaler, D.S. Microwave detection and quantification of water hidden in and on building materials: Implications for healthy buildings and microbiome studies. *BMC Infect. Dis.* **2019**, *19*, 1–8, doi:10.1186/s12879-019-3720-1.

20. Fernandez-Lacruz, R.; Bergström, D. Assessment of high-frequency technologies for determining the moisture content of comminuted solid wood fuels. *Wood Mater. Sci. Eng.* **2016**, *11*, 13–24, doi:10.1080/17480272.2014.934281.

21. Kandala, C. V.; Holser, R.; Settaluri, V.; Mani, S.; Puppala, N. Capacitance Sensing of Moisture Content in Fuel Wood Chips. *IEEE Sens. J.* **2016**, *16*, 4509–4514, doi:10.1109/JSEN.2016.2541081.

22. Salahuddin, S.; Farrugia, L.; Sammut, C. V.; O'Halloran, M.; Porter, E. Dielectric properties of fresh human blood. *Proc. 2017 19th Int. Conf. Electromagn. Adv. Appl. ICEAA 2017* **2017**, 356–359, doi:10.1109/ICEAA.2017.8065249.

23. Jaspard, F.; Nadi, M. Dielectric properties of blood: an investigation of temperature dependence. *Physiol. Meas.* **2002**, *23*, 547–554.

24. Jaspard, F.; Nadi, M.; Rouane, A. Dielectric properties of blood: An investigation of haematocrit dependence. *Physiol. Meas.* **2003**, *24*, 137–147, doi:10.1088/0967-3334/24/1/310.

25. Yoon, G. Dielectric Properties of Body Fluids with Various Hematocrit Levels. *World Acad. Sci. Eng. …* **2011**, *1*, 640–643.

26. Lonappan, A.; Hamsakkutty, V.; Bindu, G.; Jacob, J.; Thomas, V.; Mathew, K.T. Dielectric properties of human urine at microwave frequencies. *Microw. Opt. Technol. Lett.* **2004**, *42*, 500–503, doi:10.1002/mop.20349.

27. Gao, Y.; Ghasr, M.T.; Nacy, M.; Zoughi, R. Towards Accurate and Wideband In Vivo Measurement of Skin Dielectric Properties. *Dielectr. Prop. Agric. Mater. their Appl.* **2019**, *68*, 512–524, doi:10.1109/TIM.2018.2849519.

28. Abdilla, L.; Sammut, C.; Mangion, L.Z. Dielectric properties of muscle and liver from 500 MHz-40 GHz. *Electromagn. Biol. Med.* **2013**, *32*, 244–252, doi:10.3109/15368378.2013.776436.

29. Mohammed, B.; Bialkowski, K.; Abbosh, A.; Mills, P.C.; Bradley, A.P. Dielectric properties of dog brain tissue measured in vitro across the 0.3–3 GHz band. *Bioelectromagnetics* **2016**, *37*, 549–556, doi:10.1002/bem.22007.

30. Sebek, J.; Bortel, R.; Prakash, P. Broadband lung dielectric properties over the ablative temperature range: Experimental measurements and parametric

models. *Med. Phys.* **2019**, *46*, 4291–4303, doi:10.1002/mp.13704.

31. Yu, X.; Sun, Y.; Cai, K.; Yu, H.; Zhou, D.; Lu, D.; Xin, S.X. Dielectric Properties of Normal and Metastatic Lymph Nodes Ex Vivo From Lung Cancer Surgeries. *Bioelectromagnetics* **2020**, *41*, 148–155, doi:10.1002/bem.22246.

32. Kim, S.; Melikyan, H.; Kim, J.; Babajanyan, A.; Lee, J.H.; Enkhtur, L.; Friedman, B.; Lee, K. Noninvasive in vitro measurement of pig-blood d-glucose by using a microwave cavity sensor. *Diabetes Res. Clin. Pract.* **2012**, *96*, 379–384, doi:10.1016/j.diabres.2012.01.018.

33. Dobson, R.; Wu, R.; Callaghan, P. Blood glucose monitoring using microwave cavity perturbation. *Electron. Lett.* **2012**, *48*, 905–906, doi:10.1049/el.2012.1811.

34. Ebrahimi, A.; Scott, J.; Ghorbani, K. Microwave reflective biosensor for glucose level detection in aqueous solutions. *Sensors Actuators, A Phys.* **2020**, *301*, 111662, doi:10.1016/j.sna.2019.111662.

35. Omer, A.E.; Shaker, G.; Safavi-Naeini, S.; Kokabi, H.; Alquié, G.; Deshours, F.; Shubair, R.M. Low-cost portable microwave sensor for non-invasive monitoring of blood glucose level: novel design utilizing a four-cell CSRR hexagonal configuration. *Sci. Rep.* **2020**, *10*, 1–20, doi:10.1038/s41598-020-72114-3.

36. Golnabi, A.H.; Meaney, P.M.; Geimer, S.; Paulsen, K.D. Microwave imaging for breast cancer detection and therapy monitoring. In Proceedings of the 2011 IEEE Topical Conference on Biomedical Wireless Technologies, Networks, and Sensing Systems; 2011; pp. 59–62.

37. Li, X.; Hagness, S.C. A confocal microwave imaging algorithm for breast cancer detection. *IEEE Microw. Wirel. Components Lett.* **2001**, *11*, 130–132, doi:10.1109/7260.915627.

38. Wang, L. Microwave sensors for breast cancer detection. *Sensors (Switzerland)* **2018**, *18*, 1–17, doi:10.3390/s18020655.

39. Kwon, S.; Lee, S. Recent Advances in Microwave Imaging for Breast Cancer Detection. *Int. J. Biomed. Imaging* **2016**, *2016*, doi:10.1155/2016/5054912.

40. Chand, K.; Mehta, P.; Beetner, D.G.; Zoughi, R.; Stoecker, W. V. Microwave reflectometry as a novel diagnostic method for detection of skin cancers. *Conf. Rec. - IEEE Instrum. Meas. Technol. Conf.* **2005**, *2*, 1425–1428, doi:10.1109/imtc.2005.1604385.

41. Abdelgwad, A.H.; Said, T.M. Measured Dielectric permittivity of chlorinated drinking water in the microwave frequency range. In Proceedings of the 2015 IEEE 15th Mediterranean Microwave Symposium (MMS); Lecce, Italy, 2015.

42. Russel, M.; Zhenxiang, S.; Changrui, L.; Hao, Z.; Lifen, L.; Marios, S.; Yong, Z. Development of a detection method based on dielectric spectroscopy for real-time monitoring of meta-cresol contamination in beach-sand. *Sensors Actuators, A Phys.* **2017**, *268*, 16–26, doi:10.1016/j.sna.2017.10.049.

43. Jain, M.C.; Nadaraja, A.V.; Mohammadi, S.; Vizcaino, B.M.; Zarifi, M.H. Passive Microwave Biosensor for Real-Time Monitoring of Subsurface Bacterial Growth. *IEEE Trans. Biomed. Circuits Syst.* **2021**, *15*, 122–132, doi:10.1109/TBCAS.2021.3055227.

44. European Commission Counterfeiting Available online:

https://ec.europa.eu/home-affairs/counterfeiting_en (accessed on Jan 10, 2022).

45. Interpol Counterfeit currency and security documents Available online: https://www.interpol.int/en/Crimes/Counterfeit-currency-and-security-documents (accessed on May 20, 2021).

46. Nyfors, E. Industrial Microwave Sensors---A Review. *Subsurf. Sens. Technol. Appl.* **2000**, *1*, 23–43, doi:10.1023/A:1010118609079.

47. Nyfors, E.; Vainikainen, P. Industrial microwave sensors. In Proceedings of the 10th International Microwave Conference; Ksiaz Castle, Poland, 1994; pp. 45–54.

48. Macana, R.J.; Baik, O.D. Disinfestation of insect pests in stored agricultural materials using microwave and radio frequency heating: A review. *Food Rev. Int.* **2018**, *34*, 483–510, doi:10.1080/87559129.2017.1359840.

49. Piyasena, P.; Dussault, C.; Koutchma, T.; Ramaswamy, H.S.; Awuah, G.B. Radio Frequency Heating of Foods: Principles, Applications and Related Properties - A Review. *Crit. Rev. Food Sci. Nutr.* **2003**, *43*, 587–606, doi:10.1080/10408690390251129.

50. Chaouki, J.; Farag, S.; Attia, M.; Doucet, J. The development of industrial (thermal) processes in the context of sustainability: The case for microwave heating. *Can. J. Chem. Eng.* **2020**, *98*, 832–847, doi:10.1002/cjce.23710.

51. J.M. Osepchuk A History of Microwave Heating Applications. *IEEE Trans. Microw. Theory Tech.* **1984**, *32*, 1200–1224, doi:10.1109/TMTT.1984.1132831.

52. Chandrasekaran, S.; Ramanathan, S.; Basak, T. Microwave food processing-A review. *Food Res. Int.* **2013**, *52*, 243–261, doi:10.1016/j.foodres.2013.02.033.

53. Hojjati, M.; Noguera-Artiaga, L.; Wojdyło, A.; Carbonell-Barrachina, Á.A. Effects of microwave roasting on physicochemical properties of pistachios (Pistaciavera L.). *Food Sci. Biotechnol.* **2015**, *24*, 1995–2001, doi:10.1007/s10068-015-0263-0.

54. Radoiu, M. Microwave drying process scale-up. *Chem. Eng. Process. - Process Intensif.* **2020**, *155*, 108088, doi:10.1016/j.cep.2020.108088.

55. Megahed, M.G. Microwave roasting of peanuts: Effects on oil characteristics and composition. *Food/Nahrung* **2001**, *45*, 255–257, doi:10.1002/1521-3803(20010801)45:4<255::AID-FOOD255>3.0.CO;2-F.

56. Ranjan, S.; Dasgupta, N.; Walia, N.; Thara Chand, C.; Ramalingam, C. Microwave Blanching: An Emerging Trend in Food Engineering and its Effects on Capsicum annuum L. *J. Food Process Eng.* **2017**, *40*, 1–8, doi:10.1111/jfpe.12411.

57. Ahmed, J.; Ramaswamy, H.S. Microwave Pasteurization and Sterilization of Foods. In *Handbook of Food Preservation*; Rahman, M.S., Ed.; CRC Press: Boca Raton, FL, 2007; pp. 691–711.

58. Fan, H.; Fan, D.; Huang, J.; Zhao, J.; Yan, B.; Ma, S.; Zhou, W.; Zhang, H. Cooking evaluation of crayfish (Procambarus clarkia) subjected to microwave and conduction heating: A visualized strategy to understand the heat-induced quality changes of food. *Innov. Food Sci. Emerg. Technol.* **2020**, *62*, 102368, doi:10.1016/j.ifset.2020.102368.

59. Kutlu, N.; Pandiselvam, R.; Saka, I.; Kamiloglu, A.; Sahni, P.; Kothakota, A. Impact of different microwave treatments on food texture. *J. Texture Stud.* **2021**, 1–28, doi:10.1111/jtxs.12635.

60. Awuah, G.B.; Koral, T.; Guan, D. Radio-frequency baking and roasting of food products. In *Radio-Frequency Heating in Food Processing: Principles and Applications*; George B. Awuah, Hosahalli S. Ramaswamy, J.T., Ed.; CRC press: Boca Raton, 2014.

61. Wang, W.; Wang, W.; Wang, Y.; Yang, R.; Tang, J.; Zhao, Y. Hot-air assisted continuous radio frequency heating for improving drying efficiency and retaining quality of inshell hazelnuts (Corylus avellana L. cv. Barcelona). *J. Food Eng.* **2020**, *279*, 109956, doi:10.1016/j.jfoodeng.2020.109956.

62. Wang, Y.; Wig, T.D.; Tang, J.; Hallberg, L.M. Sterilization of foodstuffs using radio frequency heating. *J. Food Sci.* **2003**, *68*, 539–544, doi:10.1111/j.1365-2621.2003.tb05708.x.

63. Lu, G.M.; Feng, X.T.; Li, Y.H.; Zhang, X. The Microwave-Induced Fracturing of Hard Rock. *Rock Mech. Rock Eng.* **2019**, *52*, 3017–3032, doi:10.1007/s00603-019-01790-z.

64. Guo, L.; Lan, J.; Du, Y.; Zhang, T.C.; Du, D. Microwave-enhanced selective leaching of arsenic from copper smelting flue dusts. *J. Hazard. Mater.* **2020**, *386*, 121964, doi:10.1016/j.jhazmat.2019.121964.

65. Akbarnezhad, A.; Ong, K.C.G. Microwave decontamination of concrete. *Mag. Concr. Res.* **2010**, *62*, 879–885, doi:10.1680/macr.2010.62.12.879.

66. Makul, N.; Rattanadecho, P.; Pichaicherd, A. Accelerated microwave curing of concrete: A design and performance-related experiments. *Cem. Concr. Compos.* **2017**, *83*, 415–426, doi:10.1016/j.cemconcomp.2017.08.007.

67. Hayes, B.; Hayes, B.L. Recent Advances in Microwave- Assisted Synthesis. *Aldrichimica Acta* **2004**, *37*, 66–76.

68. Kappe, C.O.; Dallinger, D. The impact of microwave synthesis on drug discovery. *Nat. Rev. Drug Discov.* **2006**, *5*, 51–63, doi:10.1038/nrd1926.

69. Li, Y.; Yang, W. Microwave synthesis of zeolite membranes: A review. *J. Memb. Sci.* **2008**, *316*, 3–17, doi:10.1016/j.memsci.2007.08.054.

70. Wang, M.; Bai, L.; Li, M.; Gao, L.; Wang, M.; Rao, P.; Zhang, Y. Ultrafast synthesis of thin all-silica DDR zeolite membranes by microwave heating. *J. Memb. Sci.* **2019**, *572*, 567–579, doi:10.1016/j.memsci.2018.11.049.

71. Wang, L.; Yang, J.; Wang, J.; Raza, W.; Liu, G.; Lu, J.; Zhang, Y. Microwave synthesis of NaA zeolite membranes on coarse macroporous α-Al2O3 tubes for desalination. *Microporous Mesoporous Mater.* **2020**, *306*, 110360, doi:10.1016/j.micromeso.2020.110360.

72. Zeng, X.; Hu, X.; Song, H.; Xia, G.; Shen, Z.Y.; Yu, R.; Moskovits, M. Microwave synthesis of zeolites and their related applications. *Microporous Mesoporous Mater.* **2021**, *323*, 111262, doi:10.1016/j.micromeso.2021.111262.

73. Taylor, L.A.; Meek, T.T. Microwave Sintering of Lunar Soil: Properties, Theory, and Practice. *J. Aerosp. Eng.* **2005**, *18*, 188–196, doi:10.1061/(asce)0893-1321(2005)18:3(188).

74. Rybakov, K.I.; Olevsky, E.A.; Krikun, E. V. Microwave sintering: Fundamentals and modeling. *J. Am. Ceram. Soc.* **2013**, *96*, 1003–1020, doi:10.1111/jace.12278.

75. Singhal, C.; Murtaza, Q.; Parvej Microwave Sintering of Advanced Composites Materials: A Review. *Mater. Today Proc.* **2018**, *5*, 24287–24298, doi:10.1016/j.matpr.2018.10.224.

76. Schleppi, J.; Gibbons, J.; Groetsch, A.; Buckman, J.; Cowley, A.; Bennett, N. Manufacture of glass and mirrors from lunar regolith simulant. *J. Mater. Sci.* **2019**, *54*, 3726–3747, doi:10.1007/s10853-018-3101-y.

77. Duan, B.; Zhou, Y.; Wang, D.; Zhao, Y. Effect of CNTs content on the microstructures and properties of CNTs/Cu composite by microwave sintering. *J. Alloys Compd.* **2019**, *771*, 498–504, doi:10.1016/j.jallcom.2018.08.315.

78. Prakash, C.; Singh, S.; Ramakrishna, S.; Królczyk, G.; Le, C.H. Microwave sintering of porous Ti–Nb-HA composite with high strength and enhanced bioactivity for implant applications. *J. Alloys Compd.* **2020**, *824*, doi:10.1016/j.jallcom.2020.153774.

79. Kim, Y.J.; Ryu, B.H.; Jin, H.; Lee, J.; Shin, H.S. Microstructural, mechanical, and thermal properties of microwave-sintered KLS-1 lunar regolith simulant. *Ceram. Int.* **2021**, *47*, 26891–26897, doi:10.1016/j.ceramint.2021.06.098.

80. Presenda, Á.; Salvador, M.D.; Penaranda-Foix, F.L.; Catalá-Civera, J.M.; Pallone, E.; Ferreira, J.; Borrell, A. Effects of microwave sintering in aging resistance of zirconia-based ceramics. *Chem. Eng. Process. Process Intensif.* **2017**, *122*, 404–412, doi:10.1016/j.cep.2017.03.002.

81. Routray, W.; Orsat, V. Microwave-Assisted Extraction of Flavonoids: A Review. *Food Bioprocess Technol.* **2012**, *5*, 409–424, doi:10.1007/s11947-011-0573-z.

82. ALUPULUI, A.; Călinescu, I.; Lavric, V. Microwave Extraction of Active Principles. *U.P.B. Sci. Bull., Ser. B* **2012**, *74*, 129–142.

83. *Microwave-assisted Extraction for Bioactive Compounds: Theory and Practice*; Chemat, F., Cravotto, G., Eds.; Springer Science+Business Media New York, 2013; ISBN 978-1-4614-4829-7.

84. Li, Y.; Fabiano-Tixier, A.S.; Vian, M.A.; Chemat, F. Solvent-free microwave extraction of bioactive compounds provides a tool for green analytical chemistry. *TrAC - Trends Anal. Chem.* **2013**, *47*, 1–11, doi:10.1016/j.trac.2013.02.007.

85. Cassol, L.; Rodrigues, E.; Zapata Noreña, C.P. Extracting phenolic compounds from Hibiscus sabdariffa L. calyx using microwave assisted extraction. *Ind. Crops Prod.* **2019**, *133*, 168–177, doi:10.1016/j.indcrop.2019.03.023.

86. Llompart, M.; Celeiro, M.; Dagnac, T. Microwave-assisted extraction of pharmaceuticals, personal care products and industrial contaminants in the environment. *TrAC - Trends Anal. Chem.* **2019**, *116*, 136–150, doi:10.1016/j.trac.2019.04.029.

87. Kaderides, K.; Papaoikonomou, L.; Serafim, M.; Goula, A.M. Microwave-assisted extraction of phenolics from pomegranate peels: Optimization, kinetics, and comparison with ultrasounds extraction. *Chem. Eng. Process. - Process Intensif.* **2019**, *137*, 1–11, doi:10.1016/j.cep.2019.01.006.

88. Mirzadeh, M.; Arianejad, M.R.; Khedmat, L. Antioxidant, antiradical, and antimicrobial activities of polysaccharides obtained by microwave-assisted extraction method: A review. *Carbohydr. Polym.* **2020**, *229*, 115421, doi:10.1016/j.carbpol.2019.115421.

89. Ludlow-Palafox, C.; Chase, H.A. Microwave-induced pyrolysis of plastic wastes. *Ind. Eng. Chem. Res.* **2001**, *40*, 4749–4756, doi:10.1021/ie010202j.

90. Yin, C. Microwave-assisted pyrolysis of biomass for liquid biofuels production. *Bioresour. Technol.* **2012**, *120*, 273–284, doi:10.1016/j.biortech.2012.06.016.

91. Motasemi, F.; Afzal, M.T. A review on the microwave-assisted pyrolysis technique. *Renew. Sustain. Energy Rev.* **2013**, *28*, 317–330, doi:10.1016/j.rser.2013.08.008.

92. Morgan, H.M.; Bu, Q.; Liang, J.; Liu, Y.; Mao, H.; Shi, A.; Lei, H.; Ruan, R. A review of catalytic microwave pyrolysis of lignocellulosic biomass for value-added fuel and chemicals. *Bioresour. Technol.* **2017**, *230*, 112–121, doi:10.1016/j.biortech.2017.01.059.

93. Zaker, A.; Chen, Z.; Wang, X.; Zhang, Q. Microwave-assisted pyrolysis of sewage sludge: A review. *Fuel Process. Technol.* **2019**, *187*, 84–104, doi:10.1016/j.fuproc.2018.12.011.

94. Zhou, N.; Dai, L.; Lyu, Y.; Li, H.; Deng, W.; Guo, F.; Chen, P.; Lei, H.; Ruan, R. Catalytic pyrolysis of plastic wastes in a continuous microwave assisted pyrolysis system for fuel production. *Chem. Eng. J.* **2021**, *418*, 129412, doi:10.1016/j.cej.2021.129412.

95. Serra, J.M.; Borrás-Morell, J.F.; García-Baños, B.; Balaguer, M.; Plaza-González, P.; Santos-Blasco, J.; Catalán-Martínez, D.; Navarrete, L.; Catalá-Civera, J.M. Hydrogen production via microwave-induced water splitting at low temperature. *Nat. Energy* **2020**, *5*, 910–919, doi:10.1038/s41560-020-00720-6.

96. Venkatesh, M.S.; Raghavan, G.S.V. An overview of microwave processing and dielectric properties of agri-food materials. *Biosyst. Eng.* **2004**, *88*, 1–18, doi:10.1016/j.biosystemseng.2004.01.007.

97. Baker-Jarvis, J.; Janezic, M.D.; Degroot, D.C. High-frequency dielectric measurements. *IEEE Instrum. Meas. Mag.* **2010**, *13*, doi:10.1109/MIM.2010.5438334.

98. Clarke, R.; Gregory, A.; Cannell, D.; Patrick, M.; Wylie, S.; Youngs, I.; Hill, G. *A Guide to characterisation of dielectric materials at RF and microwave frequencies*; Institute of Measurement and Control and National Physical Laboratory: London, 2003; ISBN 0 904457 38 9.

99. Keysight Technologies *Basics of Measuring the Dielectric Properties of Materials*; 2020;

100. Tinga, W.R.; Nelson, S.O. Dielectric Properties of Materials for Microwave Processing - Tabulated. *J. Microw. Power* **1973**, *8*, 23–65, doi:10.1080/00222739.1973.11689017.

101. Ryynänen, S. The electromagnetic properties of food materials: A review of the basic principles. *J. Food Eng.* **1995**, *26*, 409–429, doi:10.1016/0260-8774(94)00063-F.

102. Gregory, A.P.; Clarke, R.N. *Tables of the Complex Permittivity of Dielectric Reference Liquids at Frequencies up to 5 GHz*; London, 2012;

103. Cole, K.S.; Cole, R.H. Dispersion and absorption in dielectrics I. Alternating current characteristics. *J. Chem. Phys.* **1941**, *9*, 341–351, doi:10.1063/1.1750906.

104. Davidson, D.W.; Cole, R.H. Dielectric relaxation in glycerol, propylene glycol, and n-propanol. *J. Chem. Phys.* **1951**, *19*, 1484–1490, doi:10.1063/1.1748105.

105. Havriliak, S.; Negami, S. A complex plane analysis of α-dispersions in some polymer systems. *J. Polym. Sci. Part C Polym. Symp.* **1966**, *14*, 99–117, doi:10.1002/polc.5070140111.

106. Klein, L.; Swift, C.T. An Improved Model for the Dielectric Constant of Sea Water at Microwave Frequencies. *IEEE J. Ocean. Eng.* **1977**, *2*, 104–111, doi:10.1109/JOE.1977.1145319.

107. Nelson, S.O.; Kraszewski, A.W. Dielectric Properties of Materials and Measurement Techniques. *Dry. Technol.* **1990**, *8*, 1123–1142, doi:10.1080/07373939008959939.

108. Agilent Technologies *Agilent AN 1287-2 Exploring the Architectures of Network Analyzers*; 2000;

109. keysight Technologies *Understanding the Fundamental Principles of Vector Network Analysis.*; 2020;

110. Rohde & Schwarz USA, I. *Fundamentals of Vector Network Analysis Primer*; Columbia, MD, 2017;

111. Krupka, J. Frequency domain complex permittivity measurements at microwave frequencies. *Meas. Sci. Technol.* **2006**, *17*, R55–R70, doi:10.1088/0957-0233/17/6/R01.

112. Venkatesh, M.S.; Raghavan, G.S.V. An overview of dielectric properties measuring techniques. *Can. Biosyst. Eng. / Le Genie des Biosyst. au Canada* **2005**, *47*, 15–30.

113. Rohde & Schwarz GmbH & Co. KG *Measurement of Dielectric Material Properties. Application Note*;

114. Kaatze, U. Techniques for measuring the microwave dielectric properties of materials. *Metrologia* **2010**, *47*, doi:10.1088/0026-1394/47/2/S10.

115. Ramo, S.; Whinnery, J.R.; Van Duzar, T. *Fields and Waves in Communication Electronics*; 3rd Editio.; John Wiley & Sons, Inc., 1994; ISBN 978-0-471-58551-0.

116. *Dielectric Resonators*; Kajfez, D., Guillon, P., Eds.; Second Edi.; Noble Publishing Corporation, 1998;

117. Canós, A.J.; Catalá-Civera, J.M.; Peñaranda-Foix, F.L.; De Reyes-Davó, E.L. A novel technique for deembedding the unloaded resonance frequency from measurements of microwave cavities. *IEEE Trans. Microw. Theory Tech.* **2006**, *54*, doi:10.1109/TMTT.2006.877833.

118. Kajfez, D. Linear Fractional Curve Fitting for Measurement of High Q Factors. *IEEE Trans. Microw. Theory Tech.* **1994**, *42*, 1149–1153,

doi:10.1109/22.299749.

119. Darko Kajfez *Q-Factor*; Vector Fields: Oxford, MS, USA, 1994;

120. Canós Marín, A.J.; García-Baños, B.; Catalá-Civera, J.M.; Peñaranda-Foix, F.L.; Gutiérrez-Cano, J.D. Improvement in the accuracy of dielectric measurement of open-ended coaxial resonators by an enhanced de-embedding of the coupling network. *IEEE Trans. Microw. Theory Tech.* **2013**, *61*, doi:10.1109/TMTT.2013.2285359.

121. Peñaranda-Foix, F.L.; Catalá-Civera, J.M. Circuital Analysis of Cylindrical Structures Applied to the Electromagnetic Resolution of Resonant Cavities. In *Passive Microwave Components and Antennas*; Vitaliy Zhurbenko, Ed.; IntechOpen, 2010.

122. Penaranda-Foix, F.L.; Catala-Civera, J.M.; Canos-Marin, A.J.; Garcia-Banos, B. Circuital analysis of a coaxial re-entrant cavity for performing dielectric measurement. In Proceedings of the IEEE MTT-S International Microwave Symposium Digest; 2009.

123. Kobayashi, Y.; Katoh, M. Microwave Measurement of Dielectric Properties of Low-Loss Materials By the Dielectric Rod Resonator Method. *IEEE Trans. Microw. Theory Tech.* **1985**, *MTT-33*, 586–592, doi:10.1109/tmtt.1985.1133033.

124. Yu, K.B.; Ogourtsov, S.G.; Belenky, V.G.; Maslenikov, A.B.; Omar, A.S. Accurate microwave resonant method for complex permittivity measurements of liquids. *IEEE Trans. Microw. Theory Tech.* **2000**, *48*, 2159–2164, doi:10.1109/22.884209.

125. Kawabata, H.; Tanpo, H.; Kobayashi, Y. A rigorous analysis of a TM/sub 010mode cylindrical cavity to measure accurate complex permittivity of liquid. *Conf. Proc. - 33rd Eur. Microw. Conf. EuMC 2003* **2003**, *2*, 759–762, doi:10.1109/EUMC.2003.177587.

126. Li, S.; Akyel, C.; Bosisio, R.G. Precise Calculations and Measurements on the Complex Dielectric Constant of Lossy Materials Using TM/sub 010/ Cavity Perturbation Techniques. *IEEE Trans. Microw. Theory Tech.* **1981**, *29*, 1041–1048, doi:10.1109/TMTT.1981.1130496.

127. Penaranda-Foix, F.L.; Janezic, M.D.; Catala-Civera, J.M.; Canos, A.J. Full-wave analysis of dielectric-loaded cylindrical waveguides and cavities using a new four-port ring network. *IEEE Trans. Microw. Theory Tech.* **2012**, *60*, 2730–2740, doi:10.1109/TMTT.2012.2206048.

128. Catalá-Civera, J.M.; Canós, A.J.; Plaza-González, P.; Gutiérrez, J.D.; García-Baños, B.; Peñaranda-Foix, F.L. Dynamic Measurement of Dielectric Properties of Materials at High Temperature during Microwave Heating in a Dual Mode Cylindrical Cavity. *IEEE Trans. Microw. Theory Tech.* **2015**, *63*, doi:10.1109/TMTT.2015.2453263.

129. Xi, W.; Tinga, W.R.; Voss, W.A.G.; Tian, B.Q. New Results for Coaxial Re-Entrant Cavity with Partially Dielectric Filled Gap. *IEEE Trans. Microw. Theory Tech.* **1992**, *40*, 747–753, doi:10.1109/22.127525.

130. Baker-Jarvis, J.; Riddle, B.F. *Dielectric Measurements Using a Reentrant Cavity: Mode-Matching Analysis*; 1996;

131. Marques-Villarroya, D.; Canós, A.J.; Peñaranda-Foix, F.L.; Garcia-Baños, B.; Catalá-Civera, J.M. Full-Wave Modal Analysis of a Novel Dielectrometer for Accurate Measurement of Complex Permittivity of High-Loss Liquids at Microwave Frequencies. *IEEE Trans. Microw. Theory Tech.* **2018**, *66*, 5760–5770, doi:10.1109/TMTT.2018.2881136.

132. Bernard, P.A.; Gautray, J.M. Measurement of Dielectric Constant Using a Microstrip Ring Resonator. *IEEE Trans. Microw. Theory Tech.* **1991**, *39*, 592–595, doi:10.1109/22.75310.

133. Saeed, K.; Guyette, A.C.; Hunter, I.C.; Pollard, R.D. Microstrip resonator technique for measuring dielectric permittivity of liquid solvents and for solution sensing. *IEEE MTT-S Int. Microw. Symp. Dig.* **2007**, 1185–1188, doi:10.1109/MWSYM.2007.380342.

134. Al-Behadili, A.A.; Mocanu, I.A.; Codreanu, N.; Pantazica, M. Modified split ring resonators sensor for accurate complex permittivity measurements of solid dielectrics. *Sensors* **2020**, *20*, 6855, doi:10.3390/s20236855.

135. Janezic, M.D.; Baker-Jarvis, J. Full-wave analysis of a split-cylinder resonator for nondestructive permittivity measurements. *IEEE Trans. Microw. Theory Tech.* **1999**, *47*, 2014–2020, doi:10.1109/22.795077.

136. Marques-Villarroya, D.; Penaranda-Foix, F.L.; Garcia-Banos, B.; Catala-Civera, J.M.; Gutierrez-Cano, J.D. Enhanced Full-Wave Circuit Analysis for Modeling of a Split Cylinder Resonator. *IEEE Trans. Microw. Theory Tech.* **2017**, *65*, 1191–1202, doi:10.1109/TMTT.2016.2637932.

137. Krupka, J.; Geyer, R.G.; Baker-Jarvis, J.; Ceremuga, J. Measurements of the complex permittivity of microwave circuit board substrates using split dielectric resonator and reentrant cavity techniques. In Proceedings of the Seventh International Conference on Dielectric Materials, Measurements and Applications; 1996; pp. 21–24.

138. Krupka, J.; Gregory, A.P.; Rochard, O.C.; Clarke, R.N.; Riddle, B.; Baker-Jarvis, J. Uncertainty of complex permittivity measurements by split-post dielectric resonator technique. *J. Eur. Ceram. Soc.* **2001**, *21*, 2673–2676, doi:10.1016/S0955-2219(01)00343-0.

139. Mazierska, J.; Krupka, J.; Jacob, M. V.; Ledenyov, D. Complex permittivity measurements at variable temperatures of low loss dielectric substrates employing split post and single post dielectric resonators. *IEEE MTT-S Int. Microw. Symp. Dig.* **2004**, *3*, 1825–1828, doi:10.1109/mwsym.2004.1338959.

140. Krupka, J.; Gwarek, W.; Kwietniewski, N.; Hartnett, J.G. Measurements of planar metal-dielectric structures using split-post dielectric resonators. *IEEE Trans. Microw. Theory Tech.* **2010**, *58*, 3511–3518, doi:10.1109/TMTT.2010.2086690.

141. Anlage, S.M.; Talanov, V. V; Schwartz, A.R. Principles of Near-Field Microwave Microscopy. In *Scanning Probe Microscopy: Electrical and Electromechanical Phenomena at the Nanoscale*; Kalinin, S., Gruverman, A., Eds.; Springer New York: New York, NY, 2007; pp. 215–253 ISBN 978-0-387-28668-6.

142. Imtiaz, A.; Wallis, T.M.; Kabos, P. Near-Field Scanning Microwave Microscopy: An Emerging Research Tool for Nanoscale Metrology. *IEEE Microw. Mag.* **2014**, *15*, 52–64, doi:10.1109/MMM.2013.2288711.

143. Geaney, S.; Cox, D.; Hönigl-Decrinis, T.; Shaikhaidarov, R.; Kubatkin, S.E.; Lindström, T.; Danilov, A. V.; de Graaf, S.E. Near-Field Scanning Microwave Microscopy in the Single Photon Regime. *Sci. Rep.* **2019**, *9*, 1–7, doi:10.1038/s41598-019-48780-3.

144. Geyer, R.G.; Krupka, J. Microwave Dielectric Properties of Anisotropic Materials at Cryogenic Temperatures. *IEEE Trans. Instrum. Meas.* **1995**, *44*, 329–331, doi:10.1109/19.377844.

145. Krupka, J.; Derzakowski, K.; Riddle, B.; Baker-Jarvis, J. A dielectric resonator for measurements of complex permittivity of low loss dielectric materials as a function of temperature. *Meas. Sci. Technol.* **1998**, *9*, 1751–1756, doi:10.1088/0957-0233/9/10/015.

146. Krupka, J.; Huang, W. Te; Tung, M.J. Complex permittivity measurements of low-loss microwave ceramics employing higher order quasi TE0np modes excited in a cylindrical dielectric sample. *Meas. Sci. Technol.* **2005**, *16*, 1014–1020, doi:10.1088/0957-0233/16/4/014.

147. Sheen, J. A dielectric resonator method of measuring dielectric properties of low loss materials in the microwave region. *Meas. Sci. Technol.* **2008**, *19*, doi:10.1088/0957-0233/19/5/055701.

148. Jones, R.G. Precise dielectric measurements at 35 GHz using an openmicrowave resonator. *Proc. Inst. Electr. Eng.* **1976**, *123*, 285–290, doi:10.1049/piee.1976.0067.

149. Clarke, R.N.; Rosenberg, C.B. Fabry-Perot and open resonators at microwave and millimetre wave frequencies, 2-300 GHz. *J. Phys. E.* **1982**, *15*, 9–24, doi:10.1088/0022-3735/15/1/002.

150. Danilov, I.; Heidinger, R. New approach for open resonator analysis for dielectric measurements at mm-wavelengths. *J. Eur. Ceram. Soc.* **2003**, *23*, 2623–2626, doi:10.1016/S0955-2219(03)00140-7.

151. Blackham, D. V.; Pollard, R.D. An improved technique for permittivity measurements using a coaxial probe. *IEEE Trans. Instrum. Meas.* **1997**, *46*, 1093–1099, doi:10.1109/19.676718.

152. Chiu, T. Dielectric constant measurement technique for a dielectric strip using a rectangular waveguide. *IEEE Trans. Instrum. Meas.* **2003**, *52*, 1501–1508, doi:10.1109/TIM.2003.817904.

153. Baker-Jarvis, J.; Vanzura, E.J.; Kissick, W.A. Improved technique for determining complex permittivity with the transmission/reflection method. *IEEE Trans. Microw. Theory Tech.* **1990**, *38*, doi:10.1109/22.57336.

154. Belhadj-Tahar, N.E.; Fourrier-Lamer, A. Broad-band simultaneous measurement of complex permittivity and permeability for uniaxial or isotropic materials using a coaxial discontinuity. *J. Electromagn. Waves Appl.* **1992**, *6*, 1225–1245, doi:10.1163/156939392X00698.

155. Keysight Technologies *Keysight 85070E Dielectric Probe Kit 200 MHz to 50 GHz*; 2014;

156. Baker-Jarvis, J.; Janezic, M.D.; Domich, P.D.; Geyer, R.G. Analysis of an Open-Ended Coaxial Probe with Lift-Off for Nondestructive Testing. *IEEE Trans.*

Instrum. Meas. **1994**, *43*, 711–718, doi:10.1109/19.328897.

157. Bakhtiari, S.; Qaddoumi, N.; Ganchev, S.I.; Zoughi, R. Microwave Noncontact Examination of Disbond and Thickness Variation in Stratified Composite Media. *IEEE Trans. Microw. Theory Tech.* **1994**, *42*, 389–395, doi:10.1109/22.277431.

Chapter 2

A New Stand-Alone Microwave Instrument for Measuring the Complex Permittivity of Materials at Microwave Frequencies

José D. Gutiérrez-Cano [1], Pedro J. Plaza-González [1], Antoni J. Canós [1], Beatriz García-Baños [1], José M. Catalá-Civera [1], Felipe L. Peñaranda-Foix [1]

[1] Instituto ITACA. Universitat Politècnica de València. Camino de Vera s/n.46022 Valencia, Spain.

IEEE Transactions on Instrumentation and Measurement, Volume: 69, Issue: 6, June 2020

Abstract

This article reports the development of a stand-alone and portable instrument designed to measure the complex permittivity of dielectric materials at microwave frequencies. The equipment consists of an in-house single-port vectorial reflectometer and a resonant coaxial bireentrant microwave cavity where the material under test (MUT) is placed inside a Pyrex vial, making the device appropriate for measuring liquids, semisolids, powders, and granular materials. The relationship between the dielectric properties of involved materials and the cavity resonance has been determined by numerical methods based on mode-matching and circuit analyses. In order to increase the measurement range, so that low to high loss materials can be characterized in the same cavity, the effect of the coupling network is deembedded from the resonance measurements. The performance of the newly devised instrument is evaluated by error/uncertainty analysis and comparative studies with other well-established instruments and methods. Errors lower than 2% in the dielectric constant and 5% in the loss factor are found. This simple, portable, affordable, and robust device could help nonspecialized personnel to accurately measure the dielectric properties of materials used in a wide range of microwave applications.

2.1 Introduction

Even though the precise dielectric characterization of materials has been studied for many years, it still remains an important, yet challenging task. In fact, dielectric materials attract a lot of research interest since they are widely used in communication applications such as substrates in printed circuit boards (PCBs) or dielectric resonators in filters and oscillators [1–5].

Moreover, there is an increasing demand for dielectric property measurements regarding different practical applications in fields like biological and chemical industries [6–9], agricultural research [10–12], or new food technologies [13–15]. Indeed, the study of these properties is relevant for these fields in order to ascertain the ability of dielectric materials to be processed under microwave irradiation [16]. Dielectric properties could then provide scientists and industrial engineers with valuable information to properly incorporate materials into their intended application and to investigate new effective and efficient ways to apply heat to materials and reactions.

The extensive variety of techniques to calculate dielectric properties can be categorized into resonant and nonresonant methods. The criteria used to select the appropriate technique for dielectric characterization mainly take into account the expected losses of the material under test (MUT), the frequency range covered by the measurement, and the material's attributes (format, shape, homogeneity, etc.).

Resonant methods include resonant cavities, open resonators, or dielectric resonators [17]. These techniques make use of the shift in the resonant frequency and the quality factor of a resonant structure to determine the permittivity of materials at a single frequency [18]. This procedure has become the most preferable for measuring low-loss materials [17]. However, resonant methods might also be considered for measurements of medium- and high-loss materials, if the feeding network of the cavities is included in the analysis [19].

Related literature has reported several notable implementations of resonant structures. For instance, Janezic and Baker-Jarvis [20] described a cylindrical structure divided into two halves to measure flat shaped materials placed in the gap of two cylindrical parts. Baker-Jarvis and Riddle [21] presented a full-mode model to extract the dielectric properties of cylindrical samples placed inside a reentrant cavity. Krupka et al. [22] used a split-post dielectric resonator to measure laminar-shaped low- to medium-loss materials. A common feature in all these procedures is that they require a vector network analyzer (VNA) to generate the microwave signal which is launched into the resonators and to analyze the reflected or transmitted signal that travels back with the information on the dielectric properties of the MUT.

However, VNA devices have several disadvantages. On the one hand, most of them use sophisticated equipment designed to be run in laboratories with specialized operators and which are not or barely portable. On the other hand, the cost of commercial network analyzers, which might be acceptable for the telecommunications sector, is often prohibitive for microwave power industrialists. Microwave industrial processes require specifically designed equipment to be used under industrial conditions: these devices should be simple, portable, affordable, and robust while retaining a useful subset of their current functionality. In fact, most industrial applications need only dielectric properties around ISM frequencies.

Recently, some attempts have been made to develop stand-alone devices to simplify dielectric property measurements. For example, Korpas et al. [23] reported a system which replaced the VNA by a wideband-magnitude logarithmic power detector to measure the dielectric properties of laminar materials together with a single post dielectric resonator. Corbellini and Gavioso [24] described the development and performance of a low-cost and simplified VNA instrument for the measurement of resonances in quasi-spherical microwave cavities. Likewise, Schmid and Partner Engineering AG (SPEAG) [25] developed an open-ended coaxial probe connected to an integrated and simplified vector reflectometer (R60, Copper Mountain Technologies) to determine the dielectric properties without the need for an advanced VNA.

In this article, we present a portable, stand-alone, and easy-to-use instrument which is able to perform reliable and accurate measurements of materials' dielectric properties around the ISM frequency of 2.45 GHz. The device is based on a resonant bireentrant microwave cavity, where the MUT is placed inside a Pyrex vial, making the device appropriate for measuring liquids, semisolids, powders, and granular materials, as well as solids, if properly machined to fit into the container.

An in-house VNA, consisting of a PLL synthesizer and a dual RF/IF gain and phase receiver, is implemented in the instrument to measure the magnitude and the phase of the forward and reflected signals in the microwave cavity. The advent of various wireless technologies during the last few years has made the selection of microwave components at these frequencies easily available and cost affordable.

The materials' dielectric properties are determined from the resonant frequency and Q - factor measurements and from a full-wave mode-matching analysis of the microwave cavity avoiding any previous calibration with reference materials. Both the frequency synthesizer and receiver are connected to a PC, where user-friendly LabVIEW-based software allows the automatic control of the measurement process to display the dielectric properties of the MUT in a straightforward way.

By means of this device, low-, moderate-, and high-loss materials can be accurately measured, thus providing nonspecialized personnel with an accessible system to gain knowledge about the dielectric properties of materials to be used in a wide range of microwave applications.

2.2 Design of the Measurement Cell

2.2.1 Microwave Cavity

The dielectric measurement cell is designed as a coaxial bireentrant cavity with a partially dielectric-filled gap, as shown in Fig. **1**. The cavity has a coaxial center conductor and an endplate, each with a centered hole. A cylindrical Pyrex tube containing the MUT sample is inserted into the cavity through the endplate hole and further into the center conductor which also provides a concentric alignment.

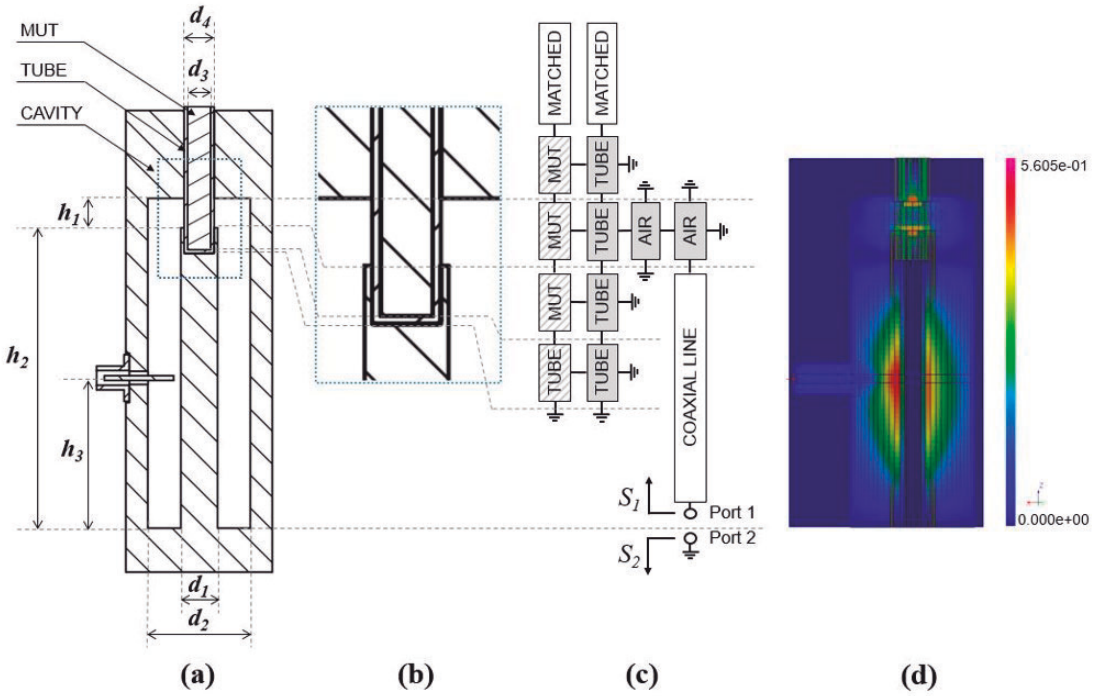

Fig. **1**: (a) Geometry of the coaxial bireentrant microwave cavity h_1=8 mm, h_2=82 mm, h_3=41 mm, d_1=10 mm, d_2=28 mm, d_3=6.4 mm, and d_4=8.2 mm. (b) Zoomed-in view of the dotted section in (a). (c) Circuital representation of the microwave cavity used for mode-matching modeling. (d) Representation of the E - field in the resonant cavity containing a Pyrex vial filled with a dielectric material simulated by means of a quickwave 3-D electromagnetic simulator.

Due to the small size of holes in the coaxial center conductor and the endplate in comparison with the wavelength, the electromagnetic fields vanish at these points, and therefore the effect of rounded ends of the Pyrex tube container can be neglected in the structure's electromagnetic modeling.

The relationship between the dielectric properties of the MUT and the cavity resonance has been determined by numerical methods based on mode-matching and circuit analyses. These methods have been employed successfully in the technical literature [26] for the analysis of similar coaxial reentrant cavities. The aim of circuit analysis is to split or segment a complex structure into smaller and simpler canonical circuits. These circuit networks, containing N ports, are analyzed and computed separately to obtain a multimodal generalized scattering matrix (GSM) or generalized admittance matrix (GAM) [27,28]. Next, all the individual matrices are connected together to establish the original structure and also the resonance condition which provides the unloaded resonant frequency f_u and the Q_u factor.

In the particular case of the structure depicted in Fig. **1**, the bireentrant cavity was segmented into 21 simpler networks—see Fig. **1**c—with only five different circuits: a two-port network for the coaxial line [27]; a three-port network (lined background) for the dielectric rod inside the tube and the central part at the bottom of the tube [27]; a four-port network ring [28] circuit (gray solid background) for the tube enclosing the dielectric

material and the air surrounding the tube; a one-port network for the matched circuits to represent infinite geometry; and a one-port network for the finite conductivity short-circuits. Each port in Fig. **1**c is represented by a solid line in the corresponding networks. An equivalence of different parts of the cavity together with the circuit networks is also shown in Fig. **1**. Fig. **2** shows the geometry of the three-port and four-port networks considered in the mode-matching analysis.

The three-port structure shown in Fig. **2**a consists of a dielectric cylinder where port 1 is on the top of the cylinder ($z=h$, $0<r<a$, $0<\varphi<2\pi$), port 2 is at the bottom of the cylinder ($z=0$, $0<r<a$, $0<\varphi<2\pi$), and port 3 is on the lateral wall ($0<z<h$, $r=b$, $0<\varphi<2\pi$). This three-port network can be analyzed by using the GAM matrix [29–33] following the procedure described in [20]. Likewise, the four-port network comprises a ring, which is similar to the three-port network but with an additional inner port at ($0<z<h$, $r=a$, $0<\varphi<2\pi$), as shown in Fig. **2**b, and the GAM matrix is solved according to [28].

Fig. **2**c shows the geometry of the reentrant section of the cavity [h_1 height in Fig. **1**a] and the network segmentation employed for this zone. The MUT is characterized by a three-port network connected to the tube in the lateral [port 3 in Fig. **2**a] and to other three-port MUT sections at the top and bottom [ports 1 and 2 in Fig. **2**a]. The region of the tube is characterized by a four-port network connected in turn to an air section [port 4 in Fig. **2**b] and to other tube networks at the top and bottom. The air sections are also four-port networks connected to the metal (inner wire) and air coaxial parts.

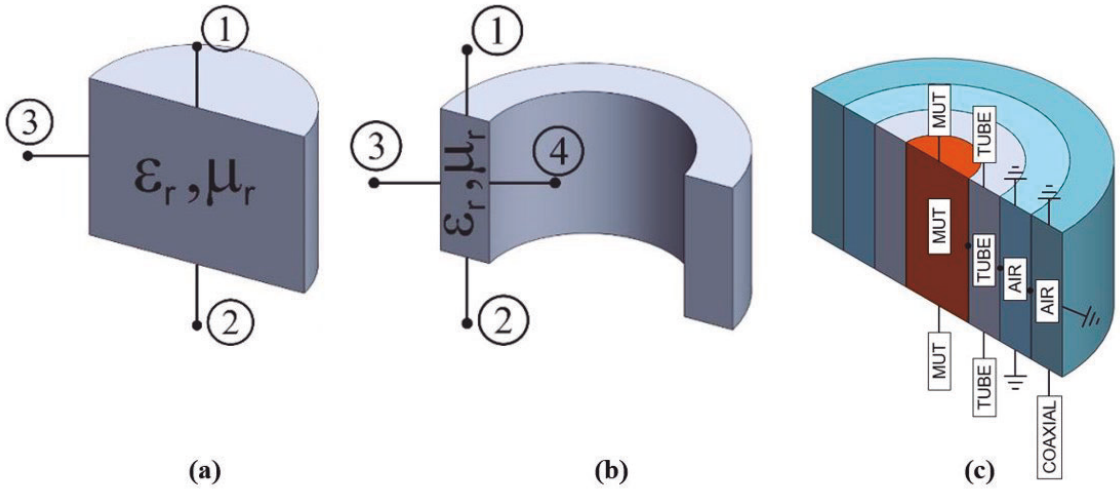

Fig. **2**: Canonical circuits used for solving the mode-matching and circuit analyses applied to the resonant cavity. (a) Three-port network. (b) Four-port network. (c) Geometry of the reentrant section of the cavity [h_1 height in Fig. **1**a] and the network segmentation employed for this zone.

For each N-port network, the GAM is represented by

$$\vec{\mathbf{e}} = \begin{pmatrix} \vec{e}_1 \\ \vec{e}_2 \\ \dots \\ \vec{e}_N \end{pmatrix} = \begin{pmatrix} \mathbf{Y}_{11} & \mathbf{Y}_{12} & \dots & \mathbf{Y}_{1N} \\ \mathbf{Y}_{21} & \mathbf{Y}_{22} & \dots & \mathbf{Y}_{2N} \\ \dots & \dots & \dots & \dots \\ \mathbf{Y}_{N1} & \mathbf{Y}_{N2} & \dots & \mathbf{Y}_{NN} \end{pmatrix} \cdot \begin{pmatrix} \vec{h}_1 \\ \vec{h}_2 \\ \dots \\ \vec{h}_N \end{pmatrix} = \bar{\bar{\mathbf{Y}}} \cdot \vec{\mathbf{h}} \tag{1}$$

where $\vec{e}_i$ and $\vec{h}_i$ are the coefficients, at port 1≤i≤N , of the series expansion of the electric and magnetic fields, using appropriate basis functions, as described in [27] and [28].

Admittance coefficients Y_{ij} are considered matrices due to the series expansion and the coupling between the ports and the basis functions. Because of the structure's axial symmetry, only the TEM and TM_{0n} modes are expanded in the coaxial and circular waveguides.

The resonant structure is then rebuilt by joining the simpler N-port networks applying the boundary conditions in the common ports (continuity of tangential electric and magnetic fields) as reported in [34–36] to calculate the GAM at port 1 (see Fig. **1**). The relationship between the GAM and the GSM is very simple and has been characterized by [33]. The resonance condition is finally applied to port 1 by means of the following equation [26]:

$$\left| S_1\left(f, \varepsilon_r\right) \cdot S_2\left(f\right) - \mathbf{1} \right| = 0 \tag{2}$$

where S_1 (f,ε_r) refers to the previous GSM calculated at port 1, S_2(f) is the GSM of port 2 (short-circuit at the lower part of the cavity), and "1 " is the symbol of the identity matrix. Equation (2) was solved numerically by the Nelder–Mead simplex method [37], which delivered a unique solution within the working frequency range (from 1.9 to 2.6 GHz). The solution of the resonant condition of Equation (2) provides the complex resonant frequency (f_Ω) of the whole original structure according to

$$f_\Omega = f_u \cdot \left(1 + \frac{j}{2Q_u}\right) \tag{3}$$

The theoretical approach described above was used to determine the dimensions of a resonant measurement cell which provided maximum sensitivity for a wide range of dielectric materials around the frequency of 2.45 GHz (see Fig. **1** for dimensions). The unloaded resonant frequency and Q -factor maps, as a function of dielectric properties obtained by Equation (2), are displayed in Fig. **3**. According to Fig. **3**, materials with dielectric constants ranging from 1 to 100 and losses from 0.001 to 10 will undergo an approximate shift in the resonant frequency from 1.9 to 2.6 GHz (more than 600 MHz) and a Q -factor variation from 1200 to 10.

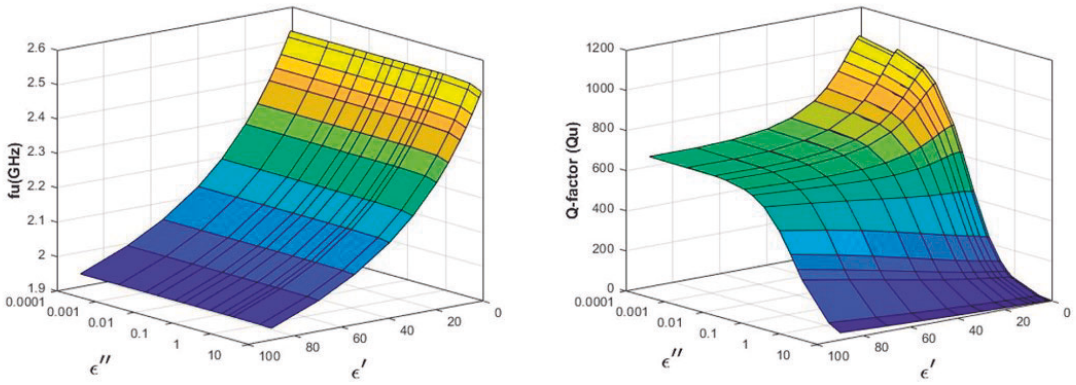

Fig. **3**: Simulated results (maps) of the unloaded resonant frequency (f_u) and the Q -factor (Q_u) as a function of dielectric properties ($\varepsilon'-j\varepsilon''$) in the bireentrant microwave cavity of Fig. **1**.

2.2.2 Coupling Network

The feeding network to couple the energy of the microwave source to the cavity is an electric probe which penetrates some distance into the coaxial cavity, as shown in Fig. **1**a. Since the coupling mechanism becomes part of the resonant structure, the resonant frequency and the Q -factor determined from reflection measurements with a VNA (referred to as loaded and denoted f_L and Q_L , respectively) shift from the theoretical (unloaded) values of the cavity (denoted f_u and Q_u , respectively).

From a general equivalent circuit, the influence of the coupling on the Q -factor has been traditionally modeled in the literature by [38–41]

$$\frac{1}{Q_L}=\frac{1}{Q_e}+\frac{1}{Q_u}=\frac{k+1}{Q_u} \tag{4}$$

where Q_e stands for the external Q -factor which accounts for losses in the coupling network and the rest of elements external to the resonator and $k=Q_u/Q_e$ is the coupling factor. Despite its simplicity and generality, expression (4) turns out to be very precise and practical since, in addition to Q_L, the values of Q_e and k can also be obtained very accurately and directly from the measurement in most cases, and thus the unloaded Q -factor can usually be determined by Equation (4), irrespective of the coupling mechanism used.

However, unlike the Q -factor, the resonant frequency shift due to the coupling cannot be modeled in such a general and precise way, but instead only in terms of parameters directly available from the measured response [19,40]. The detuning effect of the resonant frequency might be neglected if the energy is weakly coupled to the resonator, in which case unloaded resonant frequencies are practically equal to the loaded resonances ($f_u \approx f_L$). Nonetheless, this undercoupling condition results in an important limitation: medium- or high-loss materials cannot be measured because they attenuate most of the microwave signal and the cavity resonance disappears. Consequently, to measure low- and high-losses in the same cavity, the cavity has to be strongly coupled

(overcoupled), and therefore the effect of the coupling network has to be de-embedded from the measurements to retrieve the unloaded resonances.

In this respect, Canós et al. [19] have proposed an empirical technique with which the unloaded resonant frequency based on reflection measurement of one-port cavities under different coupling levels (i.e., probes of different lengths) can be obtained, in order to establish a trend toward the uncoupled cavity.

For each coupling condition, the values of f_L and Q_e are obtained by applying Kajfez's linear fractional curve fitting procedure to the measurement of the cavity [40,42], and the unloaded resonant frequency fu is estimated through the equation

$$f_L = \left(1 + \frac{A}{Q_e^{\alpha}}\right) \cdot f_u \tag{5}$$

where A and α are fitting parameters related to electromagnetic fields inside the cavity and the specific coupling network, and remain constant for different coupling levels.

This technique, which originally involves measurements with variable coupling, has been applied here for de-embedding the cavity's unloaded resonant frequency coupled with a fixed probe, as shown in Fig. **1**. In this way, the frequency response of six dielectric materials with different permittivities is measured by coupling the cavity with several electrical probes of same radii and with the same position and orientation as the probe described in Fig. **1**, but of different lengths. Pairs of A and α parameters corresponding to the measurement of each material in the cavity for determining the unloaded resonance are represented in Fig. **4** with respect to the loaded resonant frequency f_L of the 10-mm-long probe (Q_e=119.2).

As shown in Fig. **4**, the relationship of A and α with the frequency f_L is very well defined and suitable to be modeled by curve-fitting with simple functions. Through this calibration procedure, A and α can be accurately estimated from the loaded resonant frequency f_L, which is measured from the frequency response of the cavity with a fixed probe, and then the unloaded resonant frequency fu is determined using Equation (5).

The E -field of the bireentrant microwave cavity loaded with a dielectric material and coupled with the specific position and length of the coupling probe is modeled using QuickWave-3-D electromagnetic FDTD simulator software (QWED, Warsaw, Poland), and is represented in Fig. **1**b. The figure shows two E -field variations in the coaxial and bireentrant areas corresponding to the resonator length of approximately 3λ /8. The intense E -field in the MUT position is one of the reasons for the high sensitivity of the measurement cell, which is reflected in the large frequency shift obtained as a function of dielectric properties, as illustrated in Fig. **3**.

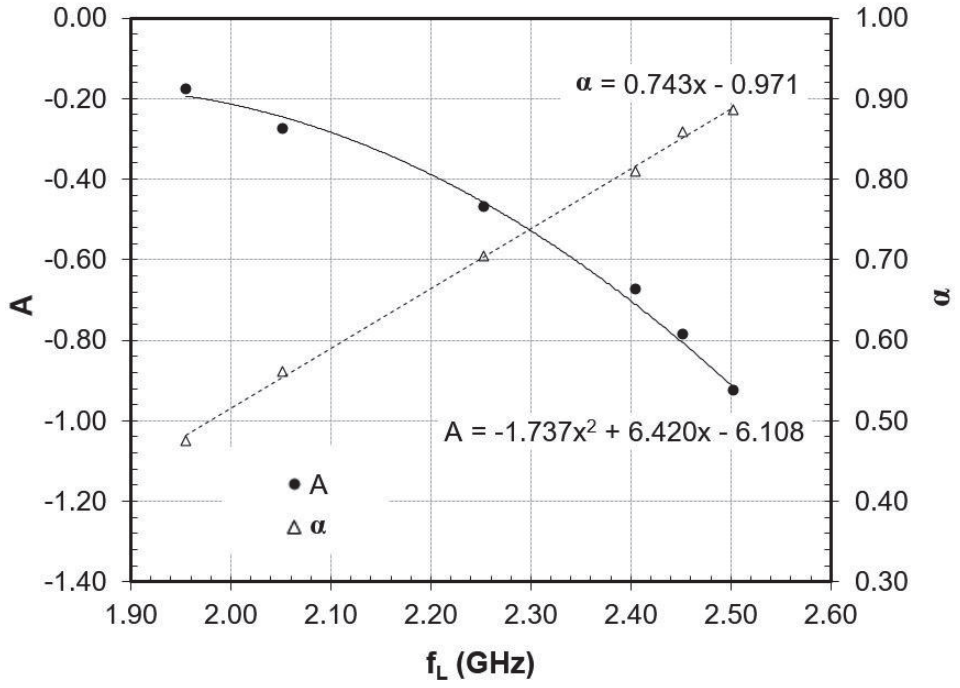

Fig. **4**: Relationship of *A* and *α* with the loaded resonant frequency (f_L) for removing the effect of the coupling network.

2.3 Experimental Setup

Fig. **5** shows a schematic of the in-house portable microwave vectorial reflectometer (PMR) developed for the dielectric measurement of materials. The microwave system consists of four main subsystems: a microwave source, a receiver which detects the magnitude and phases of the forward and reflected microwave signals in order to measure the cavity's reflection (S_{11}), a separation network, and a data acquisition system connected to a personal computer via a USB link.

The transmitter is a PLL frequency synthesizer based on an ADF4113 (analog devices) integrated circuit [43]. This chip has a built-in phase detector and an N divider which can implement a complete PLL circuit when used with an external loop filter and a voltage-controlled oscillator (ROS-2500 from mini-circuits). This block synthesizes signals that can be rapidly adjusted to generate frequency sweeps from 1500 to 2600 MHz, which is enough to cover the expected range in the resonant cavity measurements.

The receiver was designed from the commercial gain-phase detector AD8302 IC (analog devices) [44]. AD8302 detects the ratio or difference in decibels between two input signals from low frequencies to 2.7 GHz. The circuit integrates two logarithmic detectors on a single chip, each with a dynamic range of 60 dB, a digital phase detector, and circuits used for amplitude and output scaling. The outputs from AD8302 (V_{MAG} and V_{PHS}) are practically linear voltages from 0 to 1.8 V, proportional to the relative amplitude and the relative phase of the two input signals [44]. However, the range for the phase measurement is limited to 0°–180°. This restriction implies that AD8302 cannot

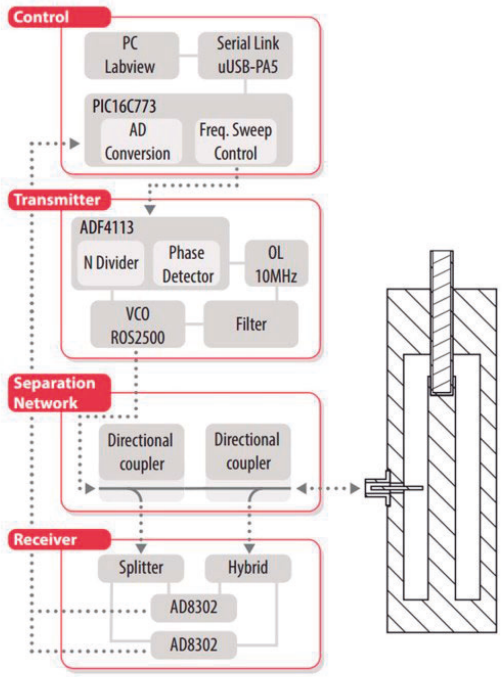

Fig. **5**: Relationship of A and α with the loaded resonant frequency (f_L) for removing the effect of the coupling network.

distinguish between an input phase difference ranging from 0° to +180° and another ranging from −180° to 0°. The inherent ambiguity of this circuit was solved here by using two AD8302 devices and adding an extra phase shift (of −90°) in one of the units.

Fig. **6** illustrates the procedure implemented with the output voltage (V_{PHS}) of the AD8302 circuits in order to solve phase ambiguity. For instance, a V_{PHS} output of 0.68 V in one of the AD8302 detectors means that it will not be able to distinguish between the relative phase of points A(−110°) and B(+110°). By shifting the second AD8302 by −90°, we can obtain a new V_{PHS} output of 1.6 V, where points A and B move to new positions: A'(−20°) and B'(20°). However, each of these positions again shows ambiguity (the phase sign of these positions is unknown again); nonetheless, only points (B-B') result in a phase shift of −90°, thus their ambiguity can be solved straightforwardly. Furthermore, the combined outputs of the two AD8302 circuits, once phase ambiguity has been solved, lead to an improvement in the stability of the entire response of the system. For example, the nonlinear zones of each AD8302 output (relative phases close to −180°, 180°, or 0°, as shown in Fig. **6**) were substituted by the linear zone of the alternative AD8302.

Fig. **5** shows the receiver block system with two AD8302 IC detectors whose input channels are shifted −90° by using a 3-dB splitter (S2D1426 from Synergy Microwave Corp.) and a 3-dB/−90° hybrid (XC2100A-03 from Anaren). The separation of the forward and reverse signals is carried out by two bidirectional couplers (BDCA 1-7-33+ from Mini-Circuits) to increase directivity.

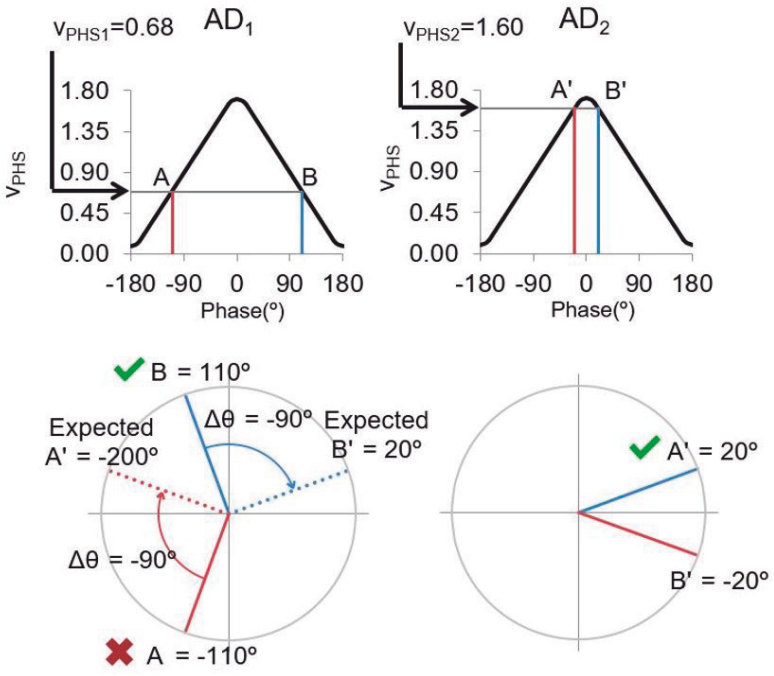

Fig. **6**: Procedure implemented to solve phase ambiguity in AD8302 IC detectors by shifting two units by −90°.

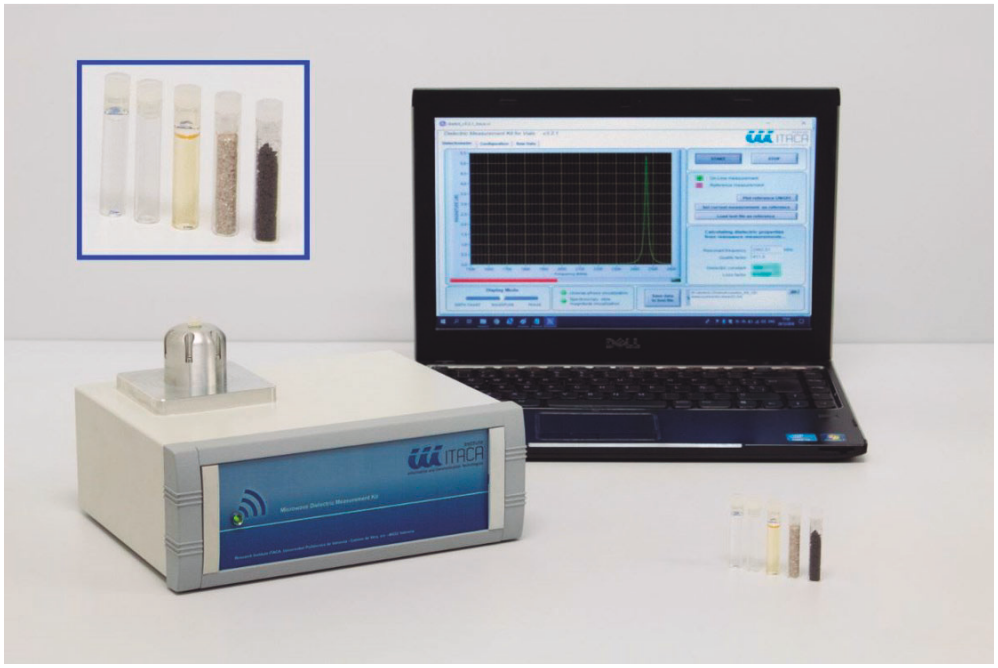

Fig. **7**: Picture of the dielectric measurement microwave system and zoomed-in view of the Pyrex vials used to hold the MUT.

The output voltage signals from the AD8302 detectors are digitalized in a multichannel 12-bits analog-to-digital converter and processed in a microprocessor (PIC16C773 from Microchip) connected via a serial link to a personal computer. Digital lines for the control of the synthesizer output frequencies are also driven by the microprocessor. LabVIEW-based software controls all the processes automatically, making the required reflection measurements and transforming the outputs into the desired display (which includes control functionalities, statistics, thresholds, and alarms). This procedure allows several measurement points per second to be obtained. The afore-described setup was assembled in a compact and portable housing. Fig. **7** shows a picture of the developed measurement system.

2.4 Experimental Results and Measurements

To evaluate the performance of the in-house dielectric measurement system described in the sections 2.2 and 2.3, the dielectric properties of eleven well-known reference materials were measured (see Table I). These materials were chosen to cover a broad permittivity and dielectric loss range and then verify the equipment's response under an extensive set of conditions.

In spite of the equipment being designed to characterize solid, powder, and liquid materials, we mostly used liquids in these tests to avoid any influence of density or air gaps of samples in the measurement results. The reference liquids were acquired from Panreac Química (Barcelona, Spain) to ensure the highest reliability of assays.In addition, a solid Macor sample from Corning Inc. (NY, USA) machined in the form of a rod of 6.38 mm diameter and a micrometer-sized Zeolite powder CBV100 from Zeolyst CV (Farmsum, the Netherlands) with a density of 0.51 g/cm3 were included in the dielectric measurement tests.

For all these materials, a detailed error analysis of the permittivity and dielectric loss factor measurements was also performed including uncertainty and a comparative study with other well-established instruments and methods (measurement bias).

2.4.1 Resonance Measurements

Fig. **8** shows the magnitude and the phase of the S_{11} parameter of the coaxial bireentrant cavity with Pyrex tubes filled with tetrahydrofuran, acetone, and distilled water, measured with the in-house single-port VNA. These materials were selected because they present dielectric losses which cover both the overcoupled and undercoupled resonances in the cavity. Measurements of the same cavity and material configuration have also been performed by a commercial full-featured VNA (ZVA50, two ports 50-GHz, Rohde & Schwarz USA, Inc., Columbia, MD) for comparison purposes. The frequency sweep was set from 1800 to 2600 MHz to cover the cavity's frequency range. The IF bandwidth for the VNA measurements was set to 1 kHz and both systems used an output power of 0 dBm. Prior to measurements, the response of both PMR and VNA was calibrated with the 85052B Standard Mechanical Calibration Kit (3.5 mm, Keysight Technologies, Santa Rosa, CA) and a standard OSM calibration procedure. The S_{11} measurements of 85052B loads with the full-featured VNA were employed as a reference for the calibration of the PMR [45].

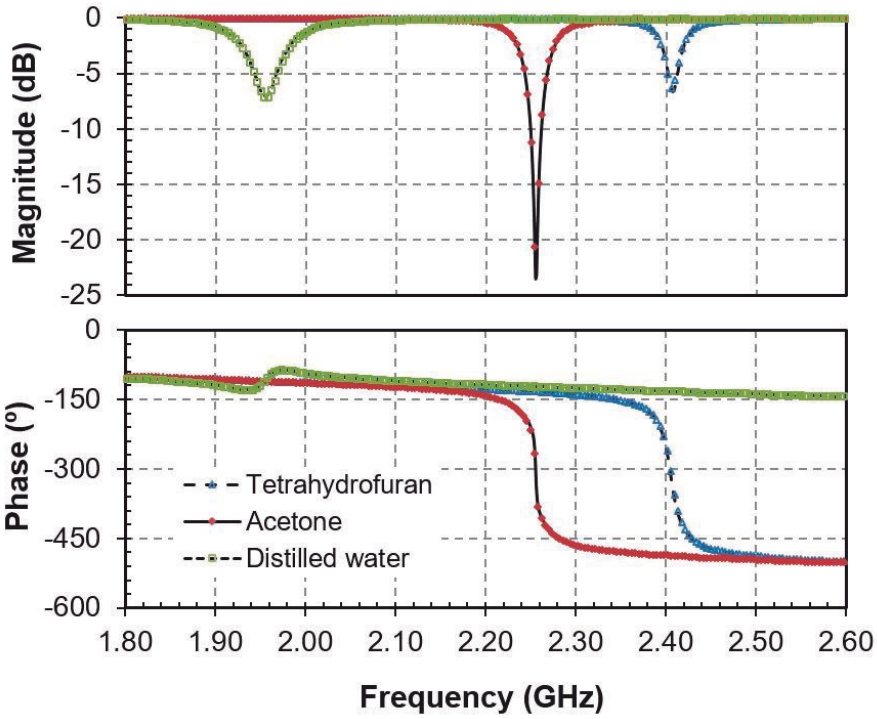

Fig. **8**: Magnitude and phase of S_{11} of the coaxial re-entrant cavity with vials filled with tetrahydrofuran, acetone, and distilled water measured by an in-house single-port VNA (solid line) and a commercial full-featured VNA (dashed line).

Table I. Complex frequency measurements of the coaxial bireentrant cavity structure loaded with reference liquids and associated uncertainties. f_{LPMR} (MHz), f_{LVNA} (MHz), and $|\Delta f_L/f_L|$ % are, respectively, the loaded resonant frequency provided by the PMR and the full featured VNA and their relative difference; Q_{uPMR} , Q_{uVNA} , $|\Delta Q_u/Q_u|$ %, and $|\Delta Q_u|$ are, respectively, the unloaded Q -Factor using the PMR and the full featured VNA and their relative and absolute differences; f_{urec} (MHz), $f_{uA\alpha}$ (MHz), and $|\Delta f_u|$ (MHz) are, respectively, the calculated unloaded resonant frequency and reference and their absolute difference

MATERIAL	$f_{L\ PMR}$ (MHz)	$f_{L\ VNA}$ (MHz)	$f_{u\ rec}$ (MHz)	$f_{u\ A\alpha}$ (MHz)	$\left\|\frac{\Delta f_L}{f_L}\right\|$ %	$\|\Delta f_u\|$ (MHz)	$Q_{U\ PMR}$	$Q_{U\ VNA}$	$\left\|\frac{\Delta Q_u}{Q_u}\right\|$ %	$\|\Delta Q_u\|$
Empty Tube	2,502.29 ± 0.17	2,502.09 ± 0.06	2,534.58 ± 0.17	2,535.11	0.008	0.525	1,168.8 ± 2.4	1,172.2 ± 1.6	0.290	3.4
Zeolite	2,487.32 ± 0.15	2,487.13 ± 0.06	2,520.82 ± 0.15	2,521.22	0.008	0.398	417.4 ± 1.2	414.6 ± 0.9	0.680	2.8
Cyclohexane	2,485.43 ± 0.12	2,485.28 ± 0.08	2,518.48 ± 0.12	2,518.99	0.006	0.511	1,173.7 ± 1.6	1,177.3 ± 1.0	0.301	3.5
Mineral Oil	2,483.70 ± 0.12	2,483.46 ± 0.03	2,516.83 ± 0.12	2,517.29	0.009	0.458	1,156.4 ± 0.8	1,156.7 ± 0.5	0.028	0.3
Toluene	2,480.10 ± 0.15	2,479.89 ± 0.03	2,513.38 ± 0.15	2,513.79	0.009	0.406	1,016.3 ± 1.4	1,011.7 ± 0.3	0.459	4.6
Oleic Acid	2,480.24 ± 0.23	2,480.05 ± 0.17	2,513.52 ± 0.23	2,514.09	0.008	0.565	664.8 ± 2.0	655.0 ± 1.5	1.499	9.8
2-Propanol	2,451.87 ± 0.06	2,451.02 ± 0.09	2,486.20 ± 0.06	2,484.94	0.034	1.259	27.9 ± 0.0	27.2 ± 0.1	2.536	0.7
Macor	2,430.27 ± 0.16	2,429.88 ± 0.08	2,464.85 ± 0.16	2,465.27	0.016	0.426	834.3 ± 1.7	828.5 ± 0.3	0.702	5.8
Tetrahydrofuran	2,404.34 ± 0.41	2,403.90 ± 0.33	2,440.18 ± 0.40	2,439.11	0.018	1.068	317.3 ± 0.8	310.3 ± 0.9	2.274	7.1
Acetone	2,252.85 ± 0.59	2,252.75 ± 0.45	2,290.68 ± 0.59	2,291.20	0.005	0.522	131.3 ± 0.1	128.6 ± 0.2	2.113	2.7
Dimethyl Sulphoxide	2,051.27 ± 0.18	2,051.70 ± 0.29	2,088.14 ± 0.18	2,090.83	0.021	2.693	15.4 ± 0.0	15.0 ± 0.0	2.880	0.4
Distilled Water	1,955.24 ± 0.94	1,955.02 ± 0.80	1,994.03 ± 0.90	1,991.30	0.011	2.731	44.5 ± 0.1	45.4 ± 0.1	1.983	0.9

The results achieved with the in-house VNA were in very good agreement with the full-featured VNA since similar resonances overlapped. The magnitude average error was lower than ±0.03 dB and the phase average error was lower than ±0.5°.

A series of eight measurements was repeated for each reference liquid in order to assess the type A experimental standard deviation on account of random variations according to [46]. Table I shows the loaded resonant frequencies (f_L) and the unloaded Q -factors (Q_u) determined by S_{11} measurements, according to the procedure described in section 2.2.

The uncertainties (standard deviations) of the loaded resonant frequencies and Q -factors have the same order of magnitude for both devices, except for those obtained for low-loss materials using the commercial VNA, which showed slightly smaller values. Nevertheless, the resonant frequency uncertainty was constrained below 1 MHz in all cases (even below 200 kHz in the majority), which means a relative resonant frequency uncertainty below 0.05%. The uncertainty of the Q -factor measurements was lower than 0.3% in all cases.

Concerning the absolute differences obtained with both systems, the calculated f_L values showed discrepancies of the same order of magnitude as in the uncertainty analysis, i.e., below 0.05%. However, the Q -factor results showed slightly higher discrepancies although constrained below 3% (see the $|\Delta Q_u|$ column in Table I). The influence of these differences on the results of dielectric properties will be assessed in sections 2.4.2 and 2.4.3.

Unloaded resonant frequencies (f_u) and associated uncertainties (standard deviations) were calculated from the measured f_L of the microwave cavity by means of the regression procedure described in section 2.2.2 [see Fig. **4** and Equation (5)] and are also included in Table I. Similar uncertainties to those that were obtained with the unloaded frequencies f_L were measured here.

The unloaded resonant frequencies used as references to analyze absolute deviations (denoted $f_{u\,Aa}$ in Table I) were determined according to [19] with electric probes of different lengths. The differences found in this comparison between both f_u values ranged from 500 kHz to almost 3 MHz. Thus, the $|\Delta f_u|$ values were used to calculate the uncertainty contribution of the resonant frequency whose results are presented in Section 2.4.3.

2.4.2 Dielectric Measurements

The average unloaded resonant frequencies and Q -factors of Table I were employed to calculate the dielectric properties using the numerical procedure described in Section 2.2.1. The results are given in Table II.

The dielectric properties of all MUTs were also measured at similar frequencies through other well-established techniques from the literature to obtain a set of values to be used as reference data for estimating the accuracy of the developed method (measurement bias). We selected the techniques to achieve the most reliable results depending on the losses of each liquid. Thus, liquid MUTs with higher losses were measured with an open-ended coaxial resonator [47], whereas liquid MUTs with lower losses were measured

with a fully loaded cylindrical cavity [48]. Macor was measured with a partially filled cylindrical cavity [14,28] and Zeolite powder by the dual-mode cylindrical cavity of [14]. The percentage given in Table II was calculated as the relative difference (bias) between the calculated dielectric properties and the reference values.

Table II. Dielectric Property Results of Reference Liquids and Associated Uncertainties.

MATERIAL	ε'_{ref}	ε''_{ref}	ε'_{calc}	ε''_{calc}	$\left\|\frac{\Delta\varepsilon'}{\varepsilon'}\right\|\%$	$\left\|\frac{\Delta\varepsilon''}{\varepsilon'}\right\|\%$
Ciclohexane	1.99 ± 0.03	0.0000 ± 0.0000	2.02 ± 0.05	0.0000 ± 0.0003	1.31	-
Zeolite	1.86 ± 0.04	0.1193 ± 0.0060	1.88 ± 0.04	0.1244 ± 0.0018	1.29	4.28
Mineral Oil	2.18 ± 0.03	0.0015 ± 0.0002	2.16 ± 0.04	0.0014 ± 0.0003	0.73	4.83
Toluene	2.43 ± 0.10	0.0109 ± 0.0005	2.42 ± 0.04	0.0112 ± 0.0005	0.25	2.95
Oleic Acid	2.37 ± 0.03	0.0444 ± 0.0010	2.37 ± 0.05	0.0442 ± 0.0019	0.17	0.62
2-Propanol	4.03 ± 0.20	3.1642 ± 0.3100	4.09 ± 0.09	3.2325 ± 0.0810	1.49	2.16
Macor	5.68 ± 0.03	0.0238 ± 0.0006	5.74 ± 0.05	0.0228 ± 0.0009	1.13	4.36
Tetrahydrofuran	7.61 ± 0.31	0.1922 ± 0.0370	7.57 ± 0.10	0.1939 ± 0.0069	0.53	0.92
Acetone	21.44 ± 0.21	0.8652 ± 0.1600	21.21 ± 0.18	0.8239 ± 0.0214	1.08	4.78
Dimethyl Sulphoxide	45.65 ± 0.39	9.3514 ± 1.0100	45.08 ± 0.71	9.5052 ± 0.4013	1.26	1.64
Distilled Water	78.47 ± 1.08	6.8709 ± 1.2200	77.51 ± 1.07	6.9014 ± 0.1691	1.22	0.45

The dielectric properties measured with the proposed method agreed well with the reference values. Therefore, the estimated accuracy obtained for the dielectric constant was within the range of 1.5% in all the covered measurements, regardless of material losses. The error in the loss factor was constrained around 5% in the considered measurement range. These results regarding the accuracy of losses are particularly relevant since the losses of materials spread throughout the four orders of magnitude (from 10^{-3} to 10^{1}).

The developed device provides the dielectric properties of the MUT inside the Pyrex tube as a bulk material. Therefore, it is important to remark that for powder or particulate materials, density and even moisture fluctuations in the sample can cause significant deviations in dielectric measurements. To overcome this situation, numerous density- and moisture-independent calibration algorithms have been successfully tested in the technical literature for the dielectric properties of particulate materials at different air-particle mixture ratios [49]. For solid materials, it has been empirically tested that samples must be precisely machined in the form of rods with an air gap between the solid sample and the Pyrex tube being no larger than 0.01 mm in order to maintain an equivalent accuracy for the liquid samples.

Although the accuracy was fairly stable across the studied materials, the measurement range was limited by the MUT losses, when the Q -factors dropped below 15, as the interpolation for the calculation of Q proved difficult to obtain reliable values.

2.4.3 Uncertainty of Permittivity Measurements

Even though a comparative review through other well-established instruments and methods was undertaken, the accuracy of the proposed technique depends on the uncertainties of different magnitudes involved in the numerical procedure given by Equations (1) and (2). These uncertainties include those of the unloaded resonances derived from the measurements using the in-house single-port VNA as well as the dimensional errors arising from the manufacturing tolerances of the resonant structure and the tubes used as holders (e.g., differences between the real dimensions of the resonant fixture and the values assumed in the computations).

The effect of these errors on the uncertainty of the computed permittivity values has been calculated taking into account the law of uncertainty propagation, or combined standard uncertainty, as carried out by GUM [46]. This effect is described in [27] for permittivity measurements and reproduced below. Assuming uncorrelated variables, the permittivity uncertainty can be computed as

$$\partial\varepsilon_{r1} = k_p \cdot \sqrt{\sum_i \left(\frac{\partial\varepsilon_{r1}}{\partial x_i} \cdot \Delta x_i \right)^2} \tag{6}$$

where x_i are different variables involved in the uncertainty of the measurement, Δx_i is the uncertainty associated with each variable, $\partial\varepsilon_{r1}/\partial x_i$ are the partial derivatives of permittivity depending on the variable used, and k_p is the coverage factor. In this article, k_p was fixed as 1 assuming a normal distribution with a level of confidence of 68.27%.

The uncertainties of the unloaded resonant frequency and the Q -factor described in this section are given in Table I (denoted $|\Delta f_u|$ and $|\Delta Q_u|$). With regard to the manufacturing tolerances, the inspection of the cavity parts showed the following dimensional uncertainties: the cavity's radius was ±20 μm , the radius of the inner coax wire was ±10 μm , the height of the coaxial part was ±10 μm , the height of the cylindrical part was ±10 μm , the internal radius of the Pyrex tube was ±10 μm , and the external radius of the Pyrex tube was ±10 μm .

Derivatives of Equation (6) were calculated through numerical methods, due to the difficulty in finding an analytical expression, as shown in [27]. The uncertainties calculated with this procedure are presented in Table II together with the average values.

For all considered liquids, the uncertainty was within the range of 2% for the dielectric constant and 5% for the loss factor. The uncertainties obtained for the low-loss materials were very close to those obtained with reference cavity methods, which is remarkable bearing in mind the usage of a fixed coupling network.

Table III shows the individual contribution of each variable involved in the uncertainty of measurements, for a representative material such as acetone. The manufacturing tolerances of the Pyrex tubes often caused the highest influence in the total uncertainty for both the dielectric constant and the loss factor. Uncertainties of the resonant frequency and Q -factor measurements $|\Delta f_u|$ and $|\Delta Q_u|$ also exhibited important contributions to the total uncertainty. The influence of the rest of parameters was limited, as indicated in Table III.

Table III. Uncertainty contributions of the involved parameters to the total uncertainty calculation for acetone (refer to Fig. **1** and Table I to ascertain the definition of the parameters).

x_i	Δx_i	$\frac{\partial \varepsilon'}{\partial x_i} \cdot \Delta x_i$	$\frac{\partial \varepsilon''}{\partial x_i} \cdot \Delta x_i$
d_1	20μm	0.03	0.0010
d_2	40μm	0.03	0.0012
d_3	20μm	0.15	0.0154
d_4	20μm	0.03	0.0026
h_1	10μm	0.01	0.0000
h_2	10μm	0.02	0.0004
$\lvert\Delta f_u\rvert$	0.522MHz	0.07	0.0011
$\lvert\Delta Q_u\rvert$	2.7	0.00	0.0145
$\partial \varepsilon_{r1}$		0.18	0.0214

2.5 Conclusions

In this article, a compact, robust, portable, and stand-alone microwave system to measure the permittivity of dielectric materials around the ISM band 2.45 GHz has been described.

The measurement process consisted of placing a Pyrex vial containing a sample of the material inside a bireentrant microwave cavity and measuring the resonant parameters of the cavity with an in-house portable microwave reflectometer. LabVIEW-based software controlled all the processes automatically, making the measurement process very simple and straightforward. Although the device is specifically appropriate for measuring liquids, semisolids, powders, and granular materials, it can also be used for solids, if properly machined to fit into the container.

The microwave cavity has been analyzed using numerical methods based on mode-matching and circuit analyses. Unlike previous efforts to design dielectric properties measurement methods, the system described in this article allowed the characterization of both high- and low-loss dielectric materials by means of a procedure that removes the effect of the coupling network from the complex resonance.

A detailed error analysis of the permittivity and dielectric loss factor measurements was also performed including uncertainty and a comparative study with other well-established instruments and methods. The estimated accuracy obtained for the dielectric constant was within the range of 1.5%, and the error in the loss factor was constrained around 5% in the considered measurement range. These results regarding the accuracy of losses are particularly relevant since the losses of materials spread throughout the four orders of magnitude (from 10^{-3} to 10^{1}).

The developed system is a very promising device to obtain dielectric property measurements in a wide range of industrial microwave applications.

2.6 Acknowledgments

This paper has been financially supported through the grant reference BES-2016-077296 of the call Convocatoria de las ayudas para contratos predoctorales para la formación de doctores de 2016 by Ministerio de Economía y Competitividad (MINECO) and by European Social Funds (ESF) of European Union and the project SEDMICRON - TEC2015-70272-R (MINECO/FEDER) supported by Ministerio de Economía y Competitividad (MINECO) and by European Regional Development Funds (ERDF) of European Union.

2.7 References

1. Wang, Z.; Liu, J.; Liu, L. Permittivity measurement of Ba0.5Sr0.5TiO3 ferroelectric thin films on multilayered silicon substrates. *IEEE Trans. Instrum. Meas.* **2006**, *55*, 350–356, doi:10.1109/TIM.2005.859144.

2. Sahu, A.; Aaen, P.H.; Lewandowski, A.; Shkunov, M.; Rigas, G.; Blanchard, P.T.; Wallis, T.M.; Devabhaktuni, V.K. Robust microwave characterization of inkjet-printed coplanar waveguides on flexible substrates. *IEEE Trans. Instrum. Meas.* **2017**, *66*, 3271–3279, doi:10.1109/TIM.2017.2753384.

3. Krupka, J.; Tobar, M.E.; Hartnett, J.G.; Cros, D.; Le Floch, J.M. Extremely high-Q factor dielectric resonators for millimeter-wave applications. *IEEE Trans. Microw. Theory Tech.* **2005**, *53*, 702–711, doi:10.1109/TMTT.2004.840572.

4. Sebastian, M.T.; Ubic, R.; Jantunen, H. Low-loss dielectric ceramic materials and their properties. *Int. Mater. Rev.* **2015**, *60*, 392–412, doi:10.1179/1743280415Y.0000000007.

5. Kato, Y.; Horibe, M. New permittivity measurement methods using resonant phenomena for high-permittivity materials. *IEEE Trans. Instrum. Meas.* **2017**, *66*, 1191–1200, doi:10.1109/TIM.2017.2662558.

6. Mohammed, B.; Bialkowski, K.; Abbosh, A.; Mills, P.C.; Bradley, A.P. Dielectric properties of dog brain tissue measured in vitro across the 0.3–3 GHz band. *Bioelectromagnetics* **2016**, *37*, 549–556, doi:10.1002/bem.22007.

7. Abdilla, L.; Sammut, C.; Mangion, L.Z. Dielectric properties of muscle and liver from 500 MHz-40 GHz. *Electromagn. Biol. Med.* **2013**, *32*, 244–252, doi:10.3109/15368378.2013.776436.

8. Chand, K.; Mehta, P.; Beetner, D.G.; Zoughi, R.; Stoecker, W. V. Microwave reflectometry as a novel diagnostic method for detection of skin cancers. *Conf. Rec. - IEEE Instrum. Meas. Technol. Conf.* **2005**, *2*, 1425–1428, doi:10.1109/imtc.2005.1604385.

9. Gao, Y.; Ghasr, M.T.; Nacy, M.; Zoughi, R. Towards Accurate and Wideband In Vivo Measurement of Skin Dielectric Properties. *Dielectr. Prop. Agric. Mater. their Appl.* **2019**, *68*, 512–524, doi:10.1109/TIM.2018.2849519.

10. Nelson, S.O. *Dielectric Properties of Agricultural Materials and their Applications*; Elsevier: New York, NY, USA, 2015;

11. Shrestha, B.L.; Wood, H.C.; Sokhansanj, S. Microwave dielectric properties of alfalfa leaves from 0.3 to 18 GHz. *IEEE Trans. Instrum. Meas.* **2011**, *60*, 2926–

2933, doi:10.1109/TIM.2011.2121270.

12. Then, Y.L.; You, K.Y.; Dimon, M.N.; Lee, C.Y. A modified microstrip ring resonator sensor with lumped element modeling for soil moisture and dielectric predictions measurement. *Meas. J. Int. Meas. Confed.* **2016**, *94*, 119–125, doi:10.1016/j.measurement.2016.07.046.

13. Venkatesh, M.S.; Raghavan, G.S.V. An overview of microwave processing and dielectric properties of agri-food materials. *Biosyst. Eng.* **2004**, *88*, 1–18, doi:10.1016/j.biosystemseng.2004.01.007.

14. Gutiérrez, J.D.; Catalá-Civera, J.M.; Bows, J.; Peñaranda-Foix, F.L. Dynamic measurement of dielectric properties of food snack pellets during microwave expansion. *J. Food Eng.* **2017**, *202*, 1–8, doi:10.1016/j.jfoodeng.2017.01.021.

15. Naderi-Boldaji, M.; Mishra, P.; Ahmadpour-Samani, M.; Ghasemi-Varnamkhasti, M.; Ghanbarian, D.; Izadi, Z. Potential of two dielectric spectroscopy techniques and chemometric analyses for detection of adulteration in grape syrup. *Meas. J. Int. Meas. Confed.* **2018**, *127*, 518–524, doi:10.1016/j.measurement.2018.06.015.

16. Jones, D.A.; Lelyveld, T.P.; Mavrofidis, S.D.; Kingman, S.W.; Miles, N.J. Microwave heating applications in environmental engineering - A review. *Resour. Conserv. Recycl.* **2002**, *34*, 75–90, doi:10.1016/S0921-3449(01)00088-X.

17. Krupka, J. Frequency domain complex permittivity measurements at microwave frequencies. *Meas. Sci. Technol.* **2006**, *17*, R55–R70, doi:10.1088/0957-0233/17/6/R01.

18. Baker-Jarvis, J.; Janezic, M.D.; Degroot, D.C. High-frequency dielectric measurements. *IEEE Instrum. Meas. Mag.* **2010**, *13*, doi:10.1109/MIM.2010.5438334.

19. Canós, A.J.; Catalá-Civera, J.M.; Peñaranda-Foix, F.L.; De Reyes-Davó, E.L. A novel technique for deembedding the unloaded resonance frequency from measurements of microwave cavities. *IEEE Trans. Microw. Theory Tech.* **2006**, *54*, doi:10.1109/TMTT.2006.877833.

20. Janezic, M.D.; Baker-Jarvis, J. Full-wave analysis of a split-cylinder resonator for nondestructive permittivity measurements. *IEEE Trans. Microw. Theory Tech.* **1999**, *47*, 2014–2020, doi:10.1109/22.795077.

21. Baker-Jarvis, J.; Riddle, B.F. *Dielectric Measurements Using a Reentrant Cavity: Mode-Matching Analysis*; 1996;

22. Krupka, J.; Clarke, R.N.; Rochard, O.C.; Gregory, A.P. Split post dielectric resonator technique for precise measurements of laminar dielectric specimens-Measurement uncertainties. In Proceedings of the Proc. 13th Int. Conf. Microw. Radar Wireless Commun.; 2000; pp. 305–308.

23. Korpas, P.; Wojtasiak, W.; Krupka, J.; Gwarek, W. Inexpensive approach to dielectric measurements. *19th Int. Conf. Microwaves, Radar Wirel. Commun. MIKON 2012* **2012**, *1*, 154–157, doi:10.1109/MIKON.2012.6233486.

24. Corbellini, S.; Gavioso, R.M. A low-cost instrument for the accurate measurement of resonances in microwave cavities. *IEEE Trans. Instrum. Meas.*

2013, *62*, 1259–1266, doi:10.1109/TIM.2013.2245038.

25. Speag DAK—Dielectric Assessment Kit Product Line Available online: http://www.speag.com/products/dak/dielectric-measurements (accessed on Oct 1, 2018).

26. Penaranda-Foix, F.L.; Catala-Civera, J.M.; Canos-Marin, A.J.; Garcia-Banos, B. Circuital analysis of a coaxial re-entrant cavity for performing dielectric measurement. In Proceedings of the IEEE MTT-S International Microwave Symposium Digest; 2009.

27. Peñaranda-Foix, F.L.; Catalá-Civera, J.M. Circuital Analysis of Cylindrical Structures Applied to the Electromagnetic Resolution of Resonant Cavities. In *Passive Microwave Components and Antennas*; Vitaliy Zhurbenko, Ed.; IntechOpen, 2010.

28. Penaranda-Foix, F.L.; Janezic, M.D.; Catala-Civera, J.M.; Canos, A.J. Full-wave analysis of dielectric-loaded cylindrical waveguides and cavities using a new four-port ring network. *IEEE Trans. Microw. Theory Tech.* **2012**, *60*, 2730–2740, doi:10.1109/TMTT.2012.2206048.

29. Rubio, J.; Gonzalez, M.A.; Zapata, J. Rigorous mutual coupling analysis of open-ended radiating structures based on SFELP (segmentation technique/finite elements/lanczos-pade) and spherical modes. In Proceedings of the Proc. IEEE Antenna Propagat. Soc. Int. Symp.; 2003; pp. 197–200.

30. Rebollar, J.M.; Esteban, J.; Page, J.E. Fullwave Analysis of Three and Four-Port Rectangular Waveguide Junctions. *IEEE Trans. Microw. Theory Tech.* **1994**, *42*, 256–263, doi:10.1109/22.275256.

31. Alessandri, F.; Mongiardo, M.; Sorrentino, R. Rigorous Mode Matching Analysis of Mitered E-Plane Bends in Rectangular Waveguide. *IEEE Microw. Guid. Wave Lett.* **1994**, *4*, 408–410, doi:10.1109/75.336229.

32. Auda, H.; Harrington, R.F. A Moment Solution for Waveguide Junction Problems. *IEEE Trans. Microw. Theory Tech.* **1983**, *31*, 515–520, doi:10.1109/TMTT.1983.1131539.

33. Conciauro, G.; Guglielmi, M.; Sorrentino, R. *Advanced Modal Analysis-CAD Techniques for Waveguide*; Wiley: New York, NY, USA, 2000;

34. Peñaranda-Foix, F.L. Application of the Generalized Circuital Analysis to Solve Electromagnetic Diffraction Problems, Univ. Politècnica de València, Valencia, Spain, 2001.

35. Diaz Caballero, E.; Belenguer, A.; Esteban, H.; Boria, V.E. Extending the cascading by pairs of multiport generalized scattering matrices for characterizing the connected ports. *IEEE Microw. Wirel. Components Lett.* **2014**, *24*, doi:10.1109/LMWC.2014.2348181.

36. Belenguer, A.; Caballero, E.D.; Esteban, H.; Borja, A.L.; Cascon, J. Krylov's solver based technique for the cascade connection of multiple N-port multimodal scattering matrices. *IEEE Trans. Microw. Theory Tech.* **2013**, *61*, doi:10.1109/TMTT.2012.2231696.

37. Lagarias, J.C.; Reeds, J.A.; Wright, M.H.; Wright, P.E. Convergence properties of the Nelder-Mead simplex method in low dimensions. *SIAM J. Optim.* **1998**, *9*,

112–147, doi:10.1137/S1052623496303470.

38. Ginzton, E.L. *Microwave Measurements*; McGraw-Hill: New York, NY, USA, 1957;

39. Aitken, J.E. Swept-frequency microwave Q-factor measurement. *Proc. Inst. Elec. Eng.* **1976**, *123*, 855–861.

40. Darko Kajfez *Q-Factor*; Vector Fields: Oxford, MS, USA, 1994;

41. Luiten, A. Q-factor measurement. In *Encyclopedia of Electrical and Electronics Engineering*; Wiley: New York, NY, USA, 1999; pp. 477–491.

42. Kajfez, D. Linear Fractional Curve Fitting for Measurement of High Q Factors. *IEEE Trans. Microw. Theory Tech.* **1994**, *42*, 1149–1153, doi:10.1109/22.299749.

43. Analog Devices RF PLL Frequency Synthesizers ADF4116/ADF4117/ADF4118 Available online: https://www.analog.com/media/en/technical-documentation/data-sheets/ADF4116_4117_4118.pdf (accessed on Feb 1, 2018).

44. Analog Devices RF/IF Gain and Phase Detector AD8302 Available online: https://www.analog.com/media/cn/technical-documentation/evaluation-documentation/AD8302.pdf (accessed on Feb 1, 2018).

45. Hiebel, M. *Fundamentals of Vector Network Analysis*; Rohde & Schwarz GmbH & Co. KG: Munich, Germany, 2011;

46. Joint Committee for Guides in Metrology *Evaluation of measurement data — Guide to the expression of uncertainty in measurement (GUM)*; 2008; Vol. JCGM 1002;

47. Canós Marín, A.J.; García-Baños, B.; Catalá-Civera, J.M.; Peñaranda-Foix, F.L.; Gutiérrez-Cano, J.D. Improvement in the accuracy of dielectric measurement of open-ended coaxial resonators by an enhanced de-embedding of the coupling network. *IEEE Trans. Microw. Theory Tech.* **2013**, *61*, doi:10.1109/TMTT.2013.2285359.

48. Collin, R.E. *Foundations for Microwave Engineering*; McGraw-Hill: New York, NY, USA, 1992;

49. Trabelsi, S.; Paz, A.M.; Nelson, S.O. Microwave dielectric method for the rapid, non-destructive determination of bulk density and moisture content of peanut hull pellets. *Biosyst. Eng.* **2013**, *115*, 332–338, doi:10.1016/j.biosystemseng.2013.04.003.

Chapter 3

Improved Open-Ended Coaxial Probe for Temperature-Dependent Permittivity Measurements of Foodstuff at Radio Frequencies

José D. Gutiérrez-Cano [1], José M. Catalá-Civera [1], Felipe L. Peñaranda-Foix [1], Pedro J. Plaza-González [1]

[1] Instituto ITACA. Universitat Politècnica de València. Camino de Vera s/n.46022 Valencia, Spain.

Journal of Food Engineering, Volume 316, March 2022, 110823

Abstract

Accurate determination of permittivity is a crucial factor for successfully developing new food processing technologies at radio frequencies. An improved measurement test fixture based on an open-ended coaxial probe was developed to determine the permittivity of lossy food products at radio frequencies as a function of temperature. In order to increase the sensitivity of the permittivity measurements at these frequencies, especially when using a vector network analyzer as a measuring device, the dimensions of the coaxial cell were carefully modeled to consider the range of dielectric losses estimated for food materials. The electromagnetic model was used to retrieve permittivity values from reflection measurements where the entire geometry of the test fixture was considered assuming there was no open radiation or infinite flanges and without the need of reference materials to calibrate the probe. The new cell was validated through permittivity measurements of six saline solutions and then, employed to determine the dielectric properties of cheese sauces and commercial milk samples at 40.68MHz up to 120ºC. The ionic content and temperature had a limited influence on the dielectric constant but highly determined the loss factor.

3.1 Introduction

Around 30% of the world's total energy consumption comes from the food sector [1]. Moreover, a 60% increase in food demand is expected by 2050 due to the growing population [2], which will significantly increase the energy demand. Radio frequency (RF) electromagnetic (EM) radiation (3kHz to 300 MHz) has been broadly investigated to replace less efficient traditional heating systems, such as baking and roasting [3], blanching [4], drying [5], pasteurization [6,7], thawing [8], cooking [9] or sterilization [10].

Unlike traditional heating technologies, where heat transfer is based on radiation, surface convection, or internal conduction [11], EM heating technologies involve the direct transfer of energy to the food product through the displacements of the elementary particles – electronic, atomic, ionic, and molecular – that constitute the material [12]. In particular, RF heating is mainly affected by dipole rotation and mobility of dissolved ions in the presence of a high-power alternating electric field [12,13], the latter being the primary factor in heat transfer at RF [14].

Permittivity is the most important material property explaining the behavior of food products when exposed to EM energy [14]. Hence, it is a key parameter for the design and optimization of RF heating processes. Other critical factors to be considered during EM and thermal analyses of RF heating applications, such as penetration depth, power density, heating rate, or conductivity, are also directly related to permittivity [12]. Permittivity depends on the frequency, temperature, moisture content, chemical composition, density, physical structure, and state of the material [15]. The size and shape of the material also influence the selection of an appropriate measurement approach [16]. At microwave frequencies, a wide variety of measurement methods and permittivity data are available for a vast number of materials [16–19], including food products [20–23]. However, permittivity data of food products remains scarce on RF heating as compared to microwave frequencies.

In this low frequency range, Sacilik and Colak [24] designed a coaxial sample holder connected to an impedance analyzer to determine the dielectric properties of corn seeds with different moisture contents at a low-frequency range, from 1 to 100MHz. Yu et al. [25] used a liquid test fixture from Agilent (16452) and an impedance analyzer to calculate the permittivity values of bulk canola seeds as a function of temperature and moisture content from 5 to 30MHz. Nelson and Bartley [26], for their part, developed a system based on a small HP-85070B open-ended coaxial probe in combination to a vector network analyzer (VNA) or an impedance analyzer to measure the dielectric properties of food products up to 95ºC at different RF and microwaves frequencies. The materials were inserted into a stainless-steel sample cup mounted in a Delrin water jacket connected to a constant–temperature liquid circulator to set the desired temperature. This system was later used to determine permittivity values of fruit and vegetable tissue samples [27] or uncooked chicken breast muscles [28]. Wang et al. [29] built a similar system, also based on the HP-87070B probe, which was part of a stainless-steel pressure-proof test cell surrounded by a temperature-controlled water jacket able to perform measurements up to 130ºC, to encompass the temperatures needed in pasteurization and sterilization processes. The coaxial probe was connected through a high-temperature coaxial cable to an impedance analyzer to cover different RF and microwave frequencies. In this last work, the authors studied the dielectric properties of whey protein mixture/gel, macaroni, and cheese, and, subsequently, other authors used

this system with other foodstuffs such as mashed potatoes [30], bread [31], dried fruit [32], or almond kernels [33]. Analogous systems with open-ended coaxial probes and VNAs were also employed to measure the permittivity values of other food products at RF [34–37]. A common feature in all these studies was the application of the open-ended coaxial probe method; in particular, the high-temperature coaxial probe from Keysight [38]. However, the small size of this probe could lead to some drawbacks when determining precise permittivity values at RF [39], as well as to noticeable uncertainties when the loss factor was considerably higher than the dielectric constant [38], which is to be expected in materials with high ionic content as is the case of food products. Furthermore, these assumptions of these models considering an open radiation with infinite flange can cause inaccuracies due to the reflection measurements of metallic walls containing the food material [40].

In this paper, we describe an improved coaxial test fixture to determine the permittivity of lossy food products at RF as a function of temperature (up to 120ºC). The method is based on an open coaxial cell radiating in a heated pressure-proof stainless-steel cylindrical vessel of appropriate dimensions to improve the accuracy of measurements at these frequencies. Unlike other methods, this vessel was included in the electromagnetic model to increase permittivity precision in order to take into account the longer wavelengths and penetration depth of RF. We assessed the increased sensitivity of this coaxial probe through a detailed uncertainty analysis of the parameters involved in the measurements and validate the measurement method through measurements of saline solutions. Finally, the permittivity values of some commercial foodstuff, such as food sauces and milk, were obtained to demonstrate the convenience of this new set-up.

3.2 Materials and Methods

3.2.1 Materials

Cheese dipping sauces and commercial ultra-high temperature-treated (UHT) milk samples were selected as representative of high-loss food materials. All of them were purchased from a local store in Valencia (Spain). The skimmed and whole UHT milk samples were produced by Lidl (Lidl Supermercados, S.A.U., Barcelona, Spain), while the cheese sauces were produced by Mission (Mission Foods Iberia S.A.U., Madrid, Spain) and Santa Maria (Santa Maria AB, Mölndal, Sweden). Table I reproduces the nutritional content of the measured food materials as listed in the manufacturers' packaging. The salt content reproduced in the table corresponds to the sodium chloride content of the food product. In addition, the ash content (minerals or inorganic constituents) determined according to AOAC 945.46 is also presented. All materials were stored unopened at room temperature until the time of measurement to avoid material degradation.

In addition, to validate the measurement method, six saline solutions with salinities ranging from 0% to 3.5% weight/volume were prepared by weighing the appropriate amounts of pharmaceutical grade sodium chloride (141659.1210, Panreac Química, Barcelona, Spain) and mixing them with water (361074.1612, Panreac Química, Barcelona, Spain) in a 50ml volumetric flask. The lower sodium chloride concentration corresponded to pure water and the higher to the salinity levels of seawater [41]. A digital

scale with a resolution of 0.01mg (SM1245Di, VWR International, Leuven, Belgium) was used for weighing the sodium chloride quantities.

Table I. Nutritional contents (Carbohydrates, Protein, Fat and Salt) of the four commercial food samples used in the study as listed in the packaging, in grams per 100g for the cheese sauces and in grams per 100ml for the milk samples. Measured ash content in grams per 100g (Ave ± STD over three replicates).

Sample	Carbohydrates	Protein	Fat	Salt	Ash
Mission cheese sauce	6.0	2.2	9.0	1.5	1.79 ± 0.04
Santa Maria cheese sauce	7.4	2.5	9.9	2.0	2.56 ± 0.06
Whole milk	4.6	3.0	3.6	0.13	0.68 ±0.01
Skimmed milk	4.8	3.1	0.3	0.13	0.72 ±0.01

3.2.2 Dielectric Properties Measurements and Experimental Set-up

The dielectric measurements were conducted using a custom-built fixture depicted in Figs. **1** to **3**. The cell consists of an open-ended coaxial probe with a built-in heat sink connected to a cylindrical measurement vessel to locate the material. The dimensions of the open-ended coaxial probe were determined to improve the measurements' accuracy at the ISM frequencies of the RF band. PEI1000 was employed as the filler material (beads) for the coaxial probe (next section). This amorphous and translucent amber thermoplastic material offers excellent heat resistance with a negligible coefficient of linear thermal expansion and consistent dielectric properties over a wide frequency and temperature range.

The sample was placed inside the heating chamber and pushed towards the coaxial aperture by means of a metallic piston that had a recess to collect the excess food material, ensuring that the cylindrical measurement vessel was completely filled with the material to avoid any air gaps. The diameter of the piston was slightly smaller than that of the heating chamber to allow the air to escape from the structure and the sample to rise to the recess to collect the excess material. The chamber was heated by two external heating resistors, regulated by a temperature controller (E5CSV, Omron, Kyoto, Japan) and a type-K thermocouple. Two O-ring elements, on the top and the bottom of the heating chamber, sealed the pressure inside the heating chamber.

To avoid any damage and calibration drifts of the VNA used to measure the reflection coefficient of the cell, a thermally insulated coaxial section with a built-in heat sink and an air fan coupled to it was employed to reduce the temperature before connecting the coaxial cable to the VNA. As a result, the temperature decreased below 30ºC in the output port of the N transition in both the inner and outer conductors of this coaxial section.

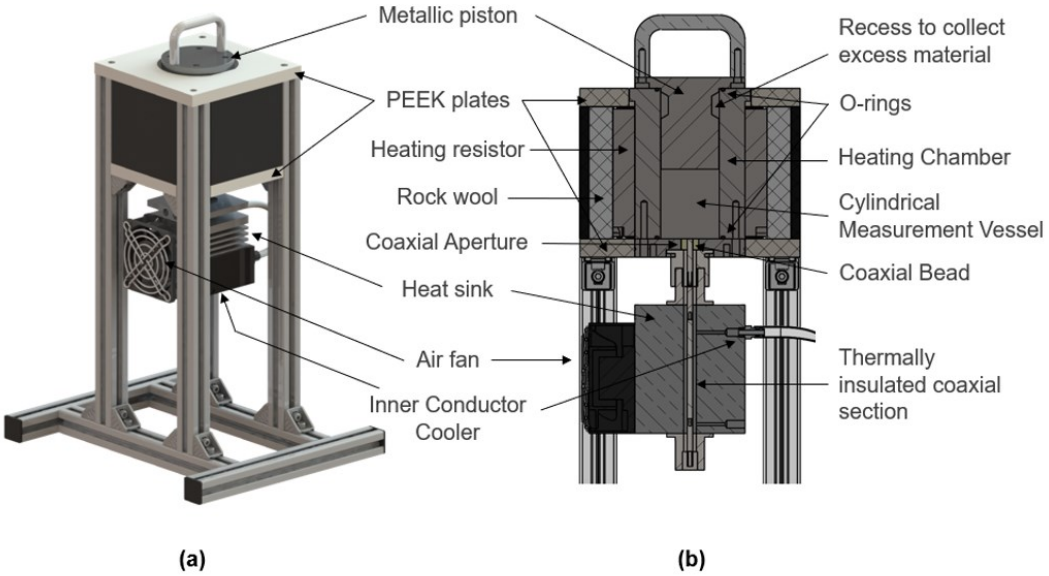

Fig. **1**: Schematic view of the open-ended permittivity measurement fixture designed at radio frequencies, (a) rendering image of the external appearance and (b) cut out cross-section of the system

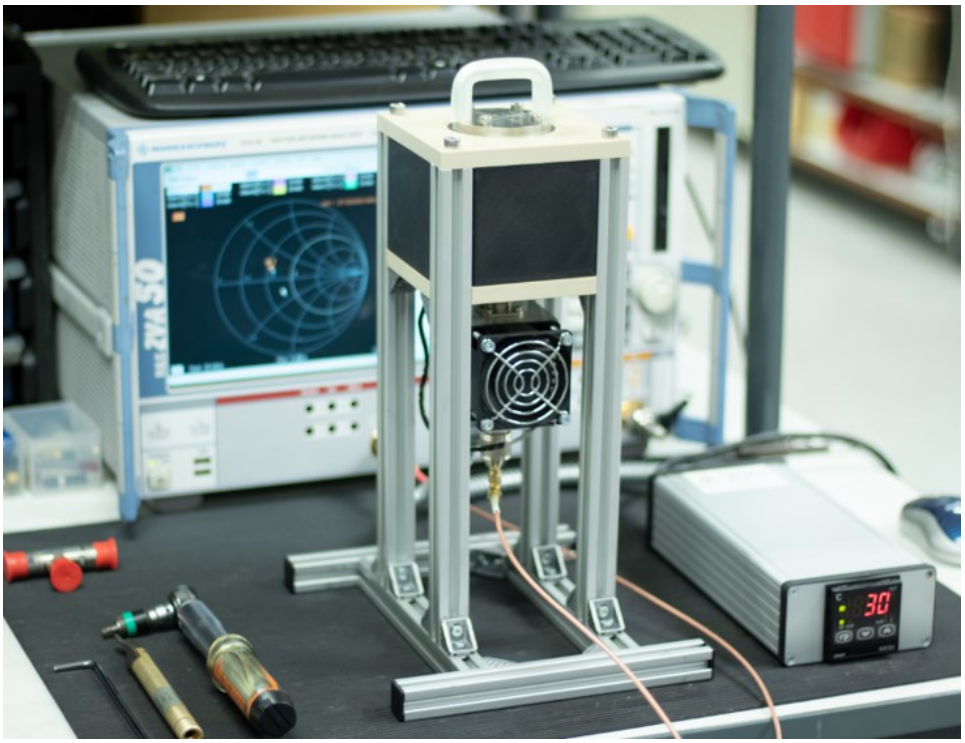

Fig. **2**: Picture of the test fixture developed to measure the dielectric properties of food materials at radio frequencies up to 120 ºC.

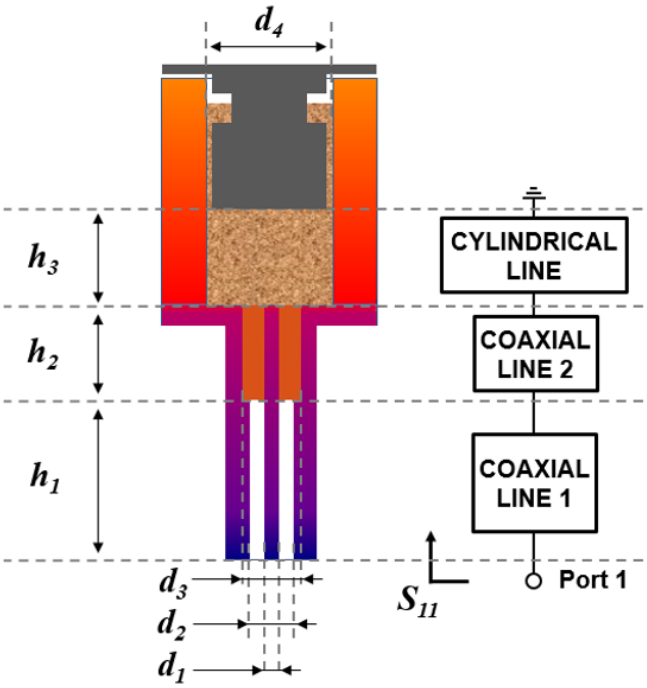

Fig. **3**: (a) Geometry diagram of the RF coaxial cell, h_1 = 155 mm, h_2 = 10 mm, h_3 = 40 mm, d_1 = 3 mm, d_2 = 6.9 mm, d_3 = 12.73 mm and d_4 = 32 mm, (b) Circuital representation of the coaxial structure used for mode-matching modelling.

All pieces in contact with the material were made of stainless steel to increase their durability and avoid long-term wear and corrosion. Two polyether ether ketone (PEEK) plates held the heating chamber and provided thermal insulation with the frame of the structure. The heating chamber was finally covered with rock wool to provide additional thermal insulation and protect the user from burns.

3.2.3 Electromagnetic Model

The electromagnetic response of the measurement device described in section 3.2.2 was modeled by circuit analysis and mode matching, a well-known technique commonly applied to the analysis of circuits at microwave frequencies [42,43]. The method is based on the segmentation of a complex structure into canonical building blocks that can be analyzed separately as N-port networks, which reduces the complexity of the whole problem [44], and which are then rejoined to characterize the complete geometry.

The analysis of open-coaxial cells is normally addressed by matching the electromagnetic fields at the aperture of a coaxial element radiating towards a dielectric medium, assuming an infinite ground plane and a semi-infinite sample size [45–47]. This approach has also been employed to model coaxial apertures in more complex circuits or resonators using circuit analysis [48]. However, given that here we have a structure confined by metal walls, we took into account the specific electromagnetic geometry and solved the transition between the coaxial line and the loaded cylindrical waveguide (the cylindrical measurement vessel), assuming there was no radiation nor any infinite

flanges. Moreover, by modeling all the elements that make up the geometry of the cell fixture, we could measure at Port 1 performing a classic VNA calibration (open, short, load) without the need of further calibrations using materials of known permittivity (the typical open, short, water calibration on the aperture of a coaxial probe).

Fig. **3** shows the separation of the measurement set-up into canonical elements. From port 1, we established 2 coaxial waveguide sections: the first one is an air-filled coaxial line [49], which corresponds to the thermally insulated coaxial section, and the second one represents the PEI1000 filled coaxial segment. Next, a circular waveguide filled with a dielectric material, representing the cylindrical measurement vessel, was connected to the second coaxial line. The geometry finishes with a lossy short circuit [50] corresponding to the bottom of the metallic piston.

After computing all the building blocks separately, the reflection coefficient at Port 1, S_{11}, can be retrieved by joining the different networks. From the S_{11} calculation, an optimization process was carried out to determine the dimensions that would maximize the sensitivity of the electromagnetic response of the test fixture in contact with the high-loss materials at RF. Even though coaxial probes can determine permittivity over a broad frequency range, for thermal food processing, only the frequencies selected for industrial, scientific, and medical applications (ISM) in the RF bands 13.56, 27.12, and 40.68 MHz were considered [51]. The final size of the different parts that make up the probe structure resulted in (see Fig. **3**): d_1 = 3mm, d_2 = 6.9mm (N size), and h_1 = 115mm for the coaxial line 1; d_1 = 3mm, d_3 = 12.73mm, and h_2 = 10mm for the coaxial line 2; and h_3 = 40mm and d_4 = 32mm for the cylindrical material housing.

To assess the performance of the above-described measurement set-up, with those dimensions, Fig. **4** shows the simulation of the reflection coefficient in Port 1 at the ISM frequency of 40.68MHz for a set of dielectric materials ranging from 1 to 200 in the dielectric constant (ε') and from 5 to 2500 in the loss factor (ε''). For a given loss factor, the simulated reflection coefficient as a function of the dielectric constants described an arc whose values are equally spaced in phase. For a fixed dielectric constant, the reflection coefficient formed a straight line with loss factor values, with the spacing decreasing as the loss factor increased. The overall response of the probe diminished as the losses of the materials increased; therefore, a reduced resolution of the dielectric constant is expected for very high-loss materials. As the figure shows, the probe's response offers a wide mapping area providing good sensitivity to discriminate between the permittivity values and the measurement values of the reflection coefficient.

For comparison purposes, Fig. **4** also depicts the reflection coefficient of an open-ended coaxial aperture with the dimensions of the Keysight 85070B probe, which was calculated for the same set of materials and frequency following the procedure by Baker-Jarvis et al. [45]. As the figure shows, the area of the Smith chart covered by our probe is about 6 times larger, compared to that of the smaller probe for the same set of materials and frequency, what makes it more sensitive to changes in the material's permittivity. The rotation of the mapping is due to the offset added by the coaxial lengths considered in our model. This behavior positively affects measurement uncertainty and demonstrates the suitability of a larger aperture for measurements of lossy food materials at such low frequencies.

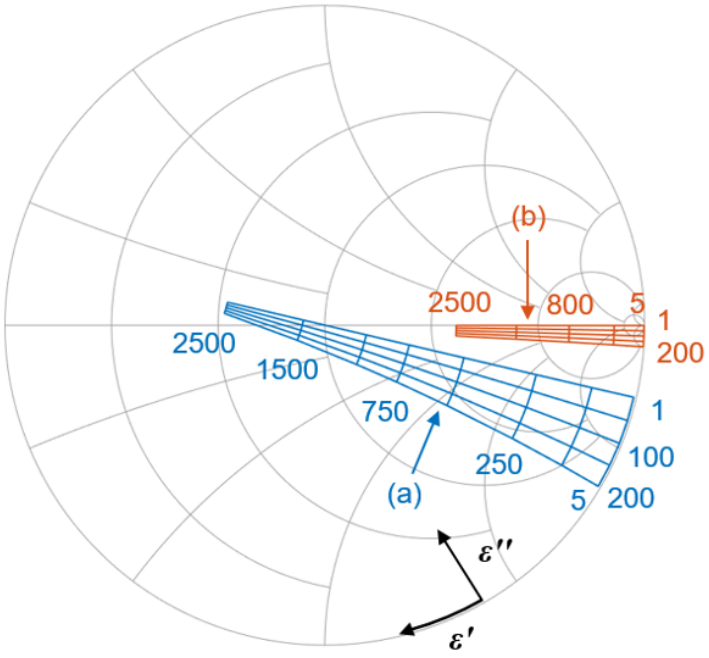

Fig. **4**: Mapping of complex permittivity onto the complex reflection coefficient plane (Smith chart) at 40.68 MHz for (a) RF coaxial cell with h_1 = 115 mm, h_2 = 10 mm, h_3 = 40 mm, d_1 = 3 mm, d_2 = 6.9 mm, d_3 = 12.73 mm, d_4 = 32 mm and bead permittivity 3 and (b) a coaxial aperture with inner diameter = 0.66 mm, outer diameter = 3 mm and bead permittivity 3.3.

From measurements, permittivity was calculated numerically by minimizing Equation (1), which evaluates the absolute difference between the measured (S_{11m}) and the simulated (S_{11}) reflection coefficients using the Nelder-Mead simplex method proposed by Lagarias et al. [52], available in the fminsearch function of Matlab (The MathWorks Inc., Natick, USA).

$$\left| \frac{S_{11}(f,\varepsilon_r,\mu_r) - S_{11m}(f,\varepsilon_r,\mu_r)}{S_{11m}(f,\varepsilon_r,\mu_r)} \right| \tag{1}$$

where ε_r= complex permittivity (dimensionless), μ_r= complex permeability (dimensionless), and f = resonant frequency (s^{-1}). For food materials, the relative permeability is generally equal to that of free space, μ_r=1 [20].

3.2.4 Uncertainty Study

The total uncertainty of the calculated permittivity was assessed through numerical methods determining the combined standard uncertainty for uncorrelated input quantities as presented in [53], whose equation is reproduced below:

$$u_c(\varepsilon) = \sqrt{\sum_i \left(\frac{\partial S_{11}}{\partial x_i} \right)^2 \cdot u^2(x_i)} \tag{2}$$

where S_{11} is the simulated reflection coefficient, x_i are the magnitudes involved in that equation showing a noticeable uncertainty contribution, and $u(x_i)$ is the standard uncertainty of those magnitudes. The sources of uncertainty analyzed were the following: dimensional errors due to manufacturing tolerances (±10 µm for d_1 and d_3; ±20 µm for d_4; and ±10 µm for h_3); errors in the permittivity value of the coaxial bead (±0.05 for ε'); and errors in the measured reflection coefficient, evaluated by estimating the Type A standard uncertainty [53] using 5 independent repeated observations of the reflection coefficient for materials with different losses to cover the mapping of the probe (±0.2º to 5º in phase and ±0.005 in magnitude). The uncertainties due to the length of the coaxial lines (h_1 and h_2) were disregarded since these magnitudes only induce a phase shift that can be easily countered by matching the length of the coaxial lines with the phase of the empty cell.

Fig. **5** shows the uncertainty evaluation of the proposed test fixture for the same set of dielectric materials examined in section 3.2.3. The uncertainty results were superimposed on the corresponding mapping of the reflection coefficient simulated from this set of materials. The cell described here displayed an uncertainty below 5% for the measurement area comprising dielectric constant values above 20 in almost the entire simulated range. Uncertainty increased slightly as the losses increased due to the narrowing of the permittivity map. Uncertainty in the loss factor shows the opposite trend, with uncertainties decreasing as the loss factor values increased, showing a loss factor uncertainty below 5% for the loss factor values above 100 and an uncertainty below 2% for the loss factor values above 250.

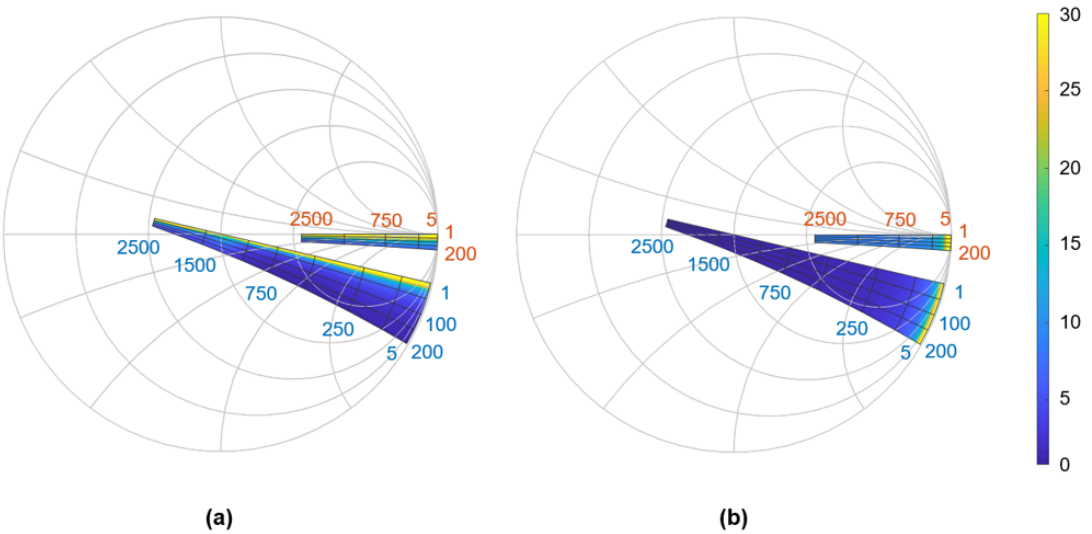

Fig. **5**: Uncertainty maps (%) at 40.68 MHz for (a) an RF coaxial cell with inner diameter = 3 mm, outer diameter = 12.73 mm, bead permittivity 3, h_1 = 115 mm, h_2 = 10 mm h_3 = 40 mm and (b) an RF coaxial cell with inner diameter = 0.66 mm, outer diameter = 3 mm, bead permittivity 3.3, $h_1 = h_2$ = 0 mm, h_3 = 40 mm and d_4 = 32 mm.

The uncertainty analysis allowed us to conclude that the main source of uncertainty derives from the reflection coefficient measurement: we found that phase uncertainty has a significant impact on the uncertainty of the dielectric constant, while magnitude uncertainty basically affects the uncertainty of the loss factor. The magnitude uncertainty also showed a noticeable influence on the dielectric constant uncertainty in the mapping areas close to the center of the Smith chart.

For comparison purposes, Fig. **5** also shows the uncertainty obtained for the smaller coaxial aperture using the same sample container and the same sources of uncertainty considered above. This smaller cell exhibited considerably higher uncertainty values than the proposed cell, above 10% in the entire simulated range, being higher than 20% for all values with a dielectric constant below 100. As expected, the uncertainty in the loss factor was also higher, with an uncertainty of about 10% for the loss factor values above 250. It should be noted that using reference materials within the calibration and calculation algorithms could reduce these uncertainties in both cell sizes, but in any case, measurement uncertainties should be taken into consideration.

3.2.5 Measurement Procedure

The proposed measurement technique was employed to determine the dielectric properties of the food materials described in section 3.2.1 at the ISM frequency of 40.68MHz. The structure's reflection coefficient was measured by means of a VNA (ZVA50, 2 ports 50GHz, Rohde & Schwarz USA, Inc., Columbia, MD). One hour was allowed to stabilize the VNA prior to calibrating within a range from 10 to 50MHz using a standard OSM calibration procedure with a Type-N calibration kit (53K36R-MSON3, Calibration kit N, 50Ω, Rosenberger, Tittmoning, Germany). The modelling of the reflection coefficient at Port 1, S_{11} in Fig. **3**, allowed this kind of calibration, avoiding the typical open, short, water calibration of coaxial probes. The cable connecting the VNA and the measurement system remained undisturbed during measurements to avoid calibration drifts [47].

A sample of 35 ml of food was put inside the device to fill the measurement vessel and nearly all the housing for excess material, what avoided disturbances from air gaps. The metal piston was tightened with 4 screws applying a torque of 5 Nm to avoid leakage and to maintain the pressure of the material inside the chamber during heating. The setpoint of the temperature controller was raised from room temperature (23 ºC) up to 120 ºC in steps of 20 ºC. The thermal stabilization of the material under test was achieved by waiting at least 30 minutes between measurements and verifying that the reading of the reflection coefficient had stabilized. After each set of measurements, the coaxial aperture and the sample vessel were cleaned with deionized water and dried with disposable paper towels. For each plotted point, three heating experiments were carried out with a different sample material, having a total of three replicates at each selected temperature.

3.3 Experimental Results and Discussion

3.3.1 Saline Solutions

Fig. **6** shows the average dielectric constant and loss factor results at room temperature of the six saline solutions as a function of their salt content. Results in the figure represent the mean value of the three replicates, while the error bars correspond to the uncertainty analysis described in section 3.2.4.

For comparison purposes, Fig. **6** also displays reference values calculated from the Debye equation reproduced below, which contains an additional term ($\sigma/\omega\varepsilon_0$) to include the contribution of ionic conductivity in the dielectric losses [41]:

$$\varepsilon = \varepsilon_\infty + \frac{\varepsilon_s - \varepsilon_\infty}{1+(j\omega\tau)^{1-\alpha}} - j\frac{\sigma}{\omega\varepsilon_0} \tag{3}$$

where ω is the angular frequency, τ is the relaxation time, α is a parameter to describe the distribution of relaxation times, ε_0 is the permittivity of free space, ε_s and ε_∞ are the lower and upper limits of the dielectric constant respectively, and σ is the ionic conductivity. For saline water, the dependence of these parameters on frequency, temperature, and salinity was provided by Klein and Swift [41]. As the dielectric losses of a sodium chloride water solution at 40.68MHz are mainly affected by ionic dissipation, while the influence of dipole polarization is negligible [54], the loss factor could also be

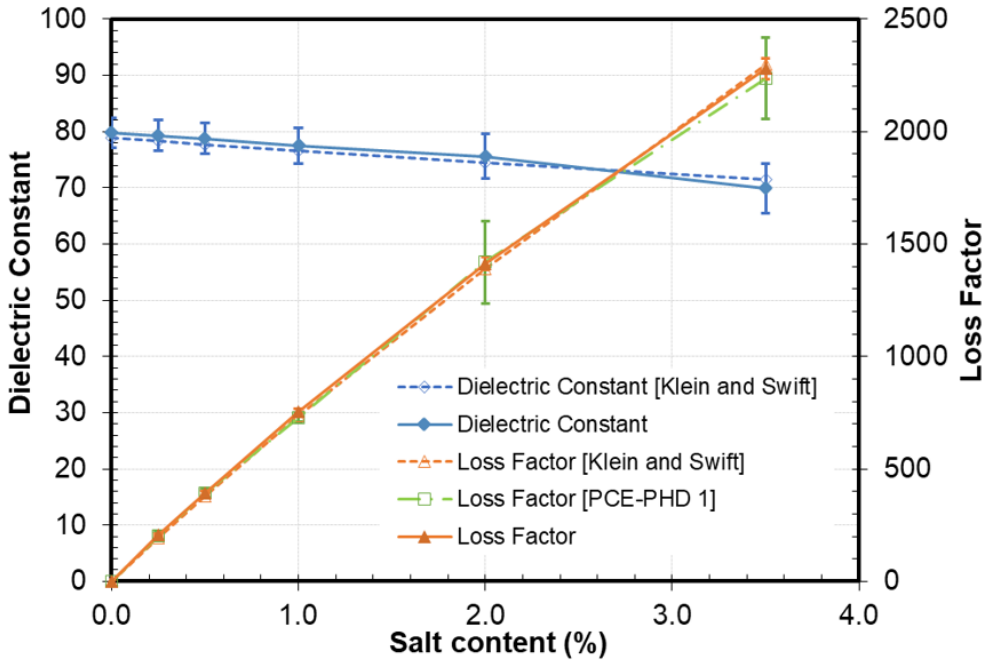

Fig. **6**: Dielectric properties at room temperature of different saline solutions as a function of their salt content at 40.68 MHz.

determined from conductivity measurements using the ionic term in Equation (3) [55]. The conductivity of the six saline solutions was measured by means of a PCE-PHD 1 Multifunction Conductivity Meter (PCE Ibérica S.L., Albacete, Spain) and the calculated loss factor values were included in Fig. **6**. The presented values are the mean of three replicates and the error bars were determined from the accuracy stated in the manual of the instrument.

Both the dielectric constant and loss factor values showed good agreement with the reference data, having uncertainties below 5% in almost all the measurement range, which validates the performance of the measurement technique at RF.

The dielectric constant of the saline solutions decreased slightly as the salt content increased, in agreement with previous measurements of food samples [30]. Studies on food materials have highlighted the minor influence of the salt content on the dielectric constant at RF, as dissolved ions reduce polarization and consequently the dielectric constant of water [35]. However, salt content does have a major impact on the loss factor values at RF. At microwave frequencies, the dielectric losses and, thus, dielectric heating are mainly affected by dipole rotation, while at RF, the ionic mobility of dissolved ions plays the key role [12,14]. The dielectric losses obtained for pure water at 40.68 MHz were practically zero, but they increased significantly in the presence of dissolved ions. Hence, the measured loss factor increased from 204.5, for a salt content of 0.25%, to 2312.9, for a salt content of 3.5%. This trend was similar in other works with food materials [30,35], although the published absolute values of permittivity differ considerably from those of the saline mixtures. The influence of salt content on permittivity depends on how it is bound to other components of the foodstuff that change the mobility of the salts [56]. Therefore, the characterization of the specific mixed final compound is recommended.

These results show the importance of dielectric characterization at RF, since slight variations in the salt level and in the mixture with other base components considerably affect the loss factor values and, consequently, the heating capabilities of food materials using electromagnetic energy. It is also interesting to remark the considerable differences among the loss factor values of these saline solutions at microwave frequencies, given that they increase from 9.6 (0%) to 46 (3.5%) at the ISM frequency of 2.45GHz [41], which demonstrates the infeasibility of using dielectric properties measured at microwave frequencies in studies at RF.

3.3.2 Cheese Sauces

Fig. **7** shows the measured average dielectric constant and loss factor values of the two cheese sauces analyzed as a function of temperature. Although the overall composition of the sauces was different, the loss factor was also found to be directly related to the salt content. At room temperature, the dielectric losses of the Mission sauce (1.5 g/100g salt and 1.79 g/100g ash) and the Santa Maria sauce (2 g/100g salt and 2.56 g/100g ash) were 840.5 and 976.7, respectively. Both curves are nearly parallel as a function of temperature, reaching very high values at 120 ºC, 2365.5 and 2639.2, respectively. This trend is similar to the values reported by Wang et al. [29], who measured a cheese sauce with an ash percentage of 1% (mass basis), half the ash content than in our sauces, but

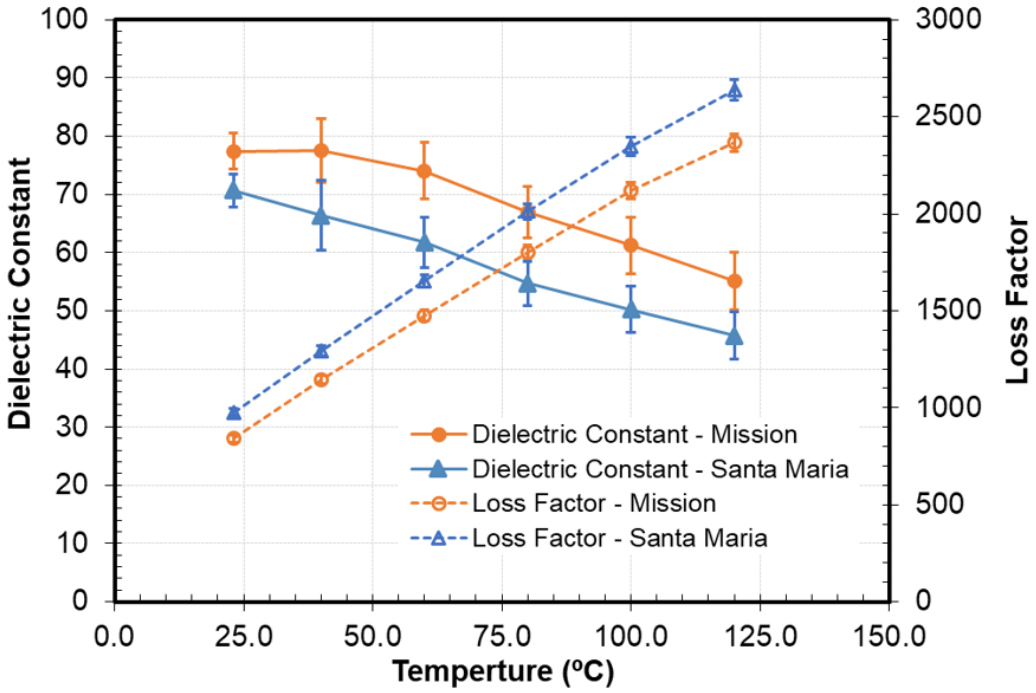

Fig. **7**: Dielectric properties of two cheese sauces as a function of temperature at 40.68 MHz

obtaining, at 40 MHz, higher loss factor values over the entire temperature range, from 885.6 at 20 ºC to 2985.5 at 121.1 ºC.

Results of the dielectric constant measurements as a function of the temperature were quite similar for both sauces, although the sauce with the highest salt content showed slightly lower values, probably due to the reduction in polarization caused by the large number of ions [35].

3.3.3 UHT Milk

Figure **8** shows the temperature dependence of the average dielectric constant and loss factor of the whole and skimmed UHT milk samples. The dielectric constant of both milk samples was very similar, although it was slightly higher in the sample with the lower fat content. A decreasing trend was observed regarding temperature, close to the results presented in section 3.3.2. Nevertheless, due to the lower loss factor values of milk samples, these measurements were in the broadest part of the probe's response and showed reduced uncertainties, which bolstered our confidence in the results obtained.

The loss factor measurements on the skimmed milk provided higher values than the whole milk (225.2 and 205.4 respectively, at room temperature). This was probably influenced by a higher ionic content in the milk [57], as the ash content of both samples suggests, and has also been reported by other authors [36,58]. Once again, both milk samples followed an increasing trend regarding the temperature, reaching values of about 600 at 120 ºC.

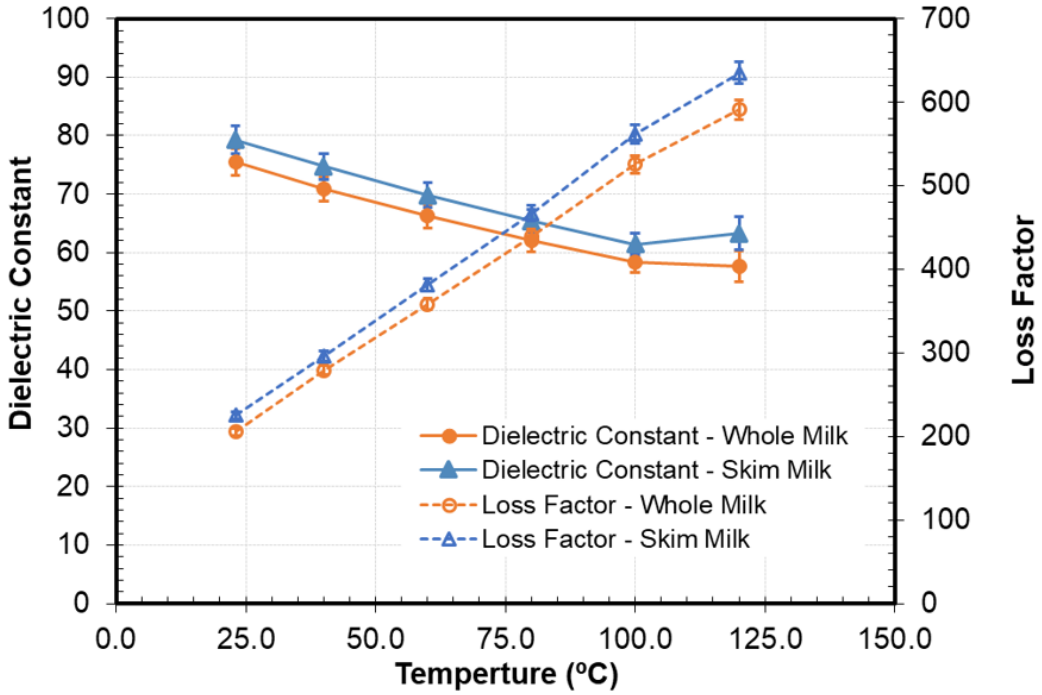

Fig. **8**: Dielectric properties of whole and skimmed milk as a function of temperature at 40.68 MHz.

Nunes et al. [59] reported the permittivity of UHT milk samples at room temperature for frequencies between 1 and 20 GHz. Their dielectric constant results are in good agreement with our measurements, ceiling the dielectric constant of milk samples to the static dielectric constant of pure water, and obtaining lower dielectric constant values as the fat content increased. They also found a Debye equation for the samples with an additional term for ionic conduction losses, which allows the calculation of permittivity values at 40.68 MHz. The loss factor values given by this equation provided 220 for skimmed milk and 225.8 for whole milk, very close to the results shown in Fig. **8**.

Other studies on permittivity examining different milk samples at RF and performing measurements with an 85070B coaxial probe in combination with a VNA have obtained dissimilar results [36,40,58]. At 40.68 MHz, some of the trends and permittivity values agreed with our results [36,58], whereas others differed [40]. The variability in these published results might be due to uncertainty issues related to the use of small-sized coaxial cells, as described in section 3.2.4, especially if measurements are carried out with a VNA.

3.4 Conclusions

An improved open coaxial test fixture for temperature-dependent permittivity measurements of high loss food products at radio frequencies (RF) was developed. In contrast with previous studies, here, the dimensions of the coaxial cell were carefully modeled to increase the sensitivity of the permittivity determination at RF especially when using a VNA as a measuring device.

The electromagnetic model utilized to retrieve permittivity values from the reflection measurements considered the entire geometry of the test fixture, assuming there was no open radiation or infinite flanges, and without having to use reference materials to calibrate the probe.

The uncertainty analysis undertaken demonstrated the greater accuracy of the used cell compared to most other approaches employed in previous works. The uncertainties in the reflection measurements were found to be the most critical factor in the overall uncertainty. The method's accuracy was also validated by measuring different saline solutions covering the measuring range of the probe with excellent results.

The permittivity of commercial cheese sauces and UHT milk samples was obtained as a function of temperature at the ISM frequency of 40.68MHz. The ionic content and temperature were shown to strongly influence permittivity, particularly the loss factor results. The measured results agree well with those reported by some authors for similar materials, while they differ from the trends found by others. The disparity in the permittivity values reported for similar materials in different works using a similar open-coaxial technique highlights the importance of using a suitable cell size customized for the frequency under study. The use of larger coaxial apertures would be an advisable option to obtain accurate dielectric properties measurements of high-loss materials at RF.

3.5 Acknowledgments

This paper has been financially supported through the grant reference BES-2016-077296 of the call Convocatoria de las ayudas para contratos predoctorales para la formación de doctores de 2016 by Ministerio de Economía y Competitividad (MINECO) and by European Social Funds (ESF) of European Union.

3.6 References

1. *Energy-smart food for people and climate. Issue Paper*; Food and Agriculture Organization of the United Nations (FAO), Ed.; 2011;

2. Ladha-Sabur, A.; Bakalis, S.; Fryer, P.J.; Lopez-Quiroga, E. Mapping energy consumption in food manufacturing. *Trends Food Sci. Technol.* **2019**, *86*, 270–280, doi:10.1016/j.tifs.2019.02.034.

3. Awuah, G.B.; Koral, T.; Guan, D. Radio-frequency baking and roasting of food products. In *Radio-Frequency Heating in Food Processing: Principles and Applications*; George B. Awuah, Hosahalli S. Ramaswamy, J.T., Ed.; CRC press: Boca Raton, 2014.

4. Zhang, X.; Shi, Q.; Gao, T.; Zhang, Z.; Guo, C.; Fu, H.; Wang, Y. Developing radio frequency blanching process of apple slice. *J. Food Eng.* **2020**, *273*, 109832, doi:10.1016/j.jfoodeng.2019.109832.

5. Wang, W.; Wang, W.; Wang, Y.; Yang, R.; Tang, J.; Zhao, Y. Hot-air assisted continuous radio frequency heating for improving drying efficiency and retaining quality of inshell hazelnuts (Corylus avellana L. cv. Barcelona). *J. Food Eng.* **2020**, *279*, 109956, doi:10.1016/j.jfoodeng.2020.109956.

6. Li, R.; Kou, X.; Cheng, T.; Zheng, A.; Wang, S. Verification of radio frequency pasteurization process for in-shell almonds. *J. Food Eng.* **2017**, *192*, 103–110, doi:10.1016/j.jfoodeng.2016.08.002.

7. Yang, Y.; Geveke, D.J.; Brunkhorst, C.D.; Sites, J.E.; Geveke, N.J.; Tilman, E.D. Optimization of the radio frequency power, time and cooling water temperature for pasteurization of Salmonella Typhimurium in shell eggs. *J. Food Eng.* **2019**, *247*, 130–135, doi:10.1016/j.jfoodeng.2018.12.004.

8. Erdogdu, F.; Altin, O.; Marra, F.; Bedane, T.F. A computational study to design process conditions in industrial radio-frequency tempering/thawing process. *J. Food Eng.* **2017**, *213*, 99–112, doi:10.1016/j.jfoodeng.2017.05.003.

9. Rincon, A.M.; Singh, R.K.; Stelzleni, A.M. Effects of endpoint temperature and thickness on quality of whole muscle non-intact steaks cooked in a Radio Frequency oven. *LWT - Food Sci. Technol.* **2015**, *64*, 1323–1328, doi:10.1016/j.lwt.2015.07.017.

10. Wang, Y.; Wig, T.D.; Tang, J.; Hallberg, L.M. Sterilization of foodstuffs using radio frequency heating. *J. Food Sci.* **2003**, *68*, 539–544, doi:10.1111/j.1365-2621.2003.tb05708.x.

11. Macana, R.J.; Baik, O.D. Disinfestation of insect pests in stored agricultural materials using microwave and radio frequency heating: A review. *Food Rev. Int.* **2018**, *34*, 483–510, doi:10.1080/87559129.2017.1359840.

12. Piyasena, P.; Dussault, C.; Koutchma, T.; Ramaswamy, H.S.; Awuah, G.B. Radio Frequency Heating of Foods: Principles, Applications and Related Properties - A Review. *Crit. Rev. Food Sci. Nutr.* **2003**, *43*, 587–606, doi:10.1080/10408690390251129.

13. Marra, F.; Zhang, L.; Lyng, J.G. Radio frequency treatment of foods: Review of recent advances. *J. Food Eng.* **2009**, *91*, 497–508, doi:10.1016/j.jfoodeng.2008.10.015.

14. Jiao, Y.; Tang, J.; Wang, Y.; Koral, T.L. Radio-Frequency Applications for Food Processing and Safety. *Annu. Rev. Food Sci. Technol.* **2018**, *9*, 105–127, doi:10.1146/annurev-food-041715-033038.

15. Venkatesh, M.S.; Raghavan, G.S.V. An overview of microwave processing and dielectric properties of agri-food materials. *Biosyst. Eng.* **2004**, *88*, 1–18, doi:10.1016/j.biosystemseng.2004.01.007.

16. Krupka, J. Frequency domain complex permittivity measurements at microwave frequencies. *Meas. Sci. Technol.* **2006**, *17*, R55–R70, doi:10.1088/0957-0233/17/6/R01.

17. Catalá-Civera, J.M.; Canós, A.J.; Plaza-González, P.; Gutiérrez, J.D.; García-Baños, B.; Peñaranda-Foix, F.L. Dynamic Measurement of Dielectric Properties of Materials at High Temperature during Microwave Heating in a Dual Mode Cylindrical Cavity. *IEEE Trans. Microw. Theory Tech.* **2015**, *63*, 2905–2914, doi:10.1109/TMTT.2015.2453263.

18. García-Baños, B.; Cuesta-Soto, F.; Griol, A.; Catalá-Civera, J.M.; Pitarch, J. Enhancement of sensitivity of microwave planar sensors with EBG structures. *IEEE Sens. J.* **2006**, *6*, 1518–1522, doi:10.1109/JSEN.2006.884506.

19. García-Baños, B.; Catalá-Civera, J.M.; Canós, A.J.; Peñaranda-Foix, F. Design rules for the optimization of the sensitivity of open-ended coaxial microwave sensors for monitoring changes in dielectric materials. *Meas. Sci. Technol.* **2005**, *16*, 1186–1192, doi:10.1088/0957-0233/16/5/019.

20. *Handbook of Microwave Technology for food applications*; Datta, A.K., Anantheswaran, R.C., Eds.; Marcel Dekker, Inc.: New York, 2001;

21. Gutiérrez-Cano, J.D.; Hamilton, I.E.; Catalá-Civera, J.M.; Bows, J.; Peñaranda-Foix, F.L. Effect of water content on the dynamic measurement of dielectric properties of food snack pellets during microwave expansion. *J. Food Eng.* **2018**, *232*, 21–28, doi:10.1016/j.jfoodeng.2018.03.018.

22. Gutiérrez, J.D.; Catalá-Civera, J.M.; Bows, J.; Peñaranda-Foix, F.L. Dynamic measurement of dielectric properties of food snack pellets during microwave expansion. *J. Food Eng.* **2017**, *202*, 1–8, doi:10.1016/j.jfoodeng.2017.01.021.

23. Meda, V.; Orsat, V.; Raghavan, V. Microwave heating and the dielectric properties of foods. In *The Microwave Processing of Foods: Second Edition*; Regier, M., Knoerzer, K., Schubert, H., Eds.; Elsevier Inc., 2017; pp. 23–43 ISBN 9780081005286.

24. Sacilik, K.; Colak, A. Determination of dielectric properties of corn seeds from 1 to 100 MHz. *Powder Technol.* **2010**, *203*, 365–370, doi:10.1016/j.powtec.2010.05.031.

25. Yu, D.U.; Shrestha, B.L.; Baik, O.D. Radio frequency dielectric properties of bulk canola seeds under different temperatures, moisture contents, and frequencies for feasibility of radio frequency disinfestation. *Int. J. Food Prop.* **2015**, *18*, 2746–2763, doi:10.1080/10942912.2015.1013630.

26. Nelson, S.O.; Bartley, P.G. Frequency and temperature dependence of the dielectric properties of food materials. *Trans. ASAE* **2002**, *45*, 1223–1227, doi:10.13031/2013.9931.

27. Nelson, S.O. Frequency- and temperature-dependent permittivities of fresh fruits and vegetables from 0.01 To 1.8 GHz. *Trans. Am. Soc. Agric. Eng.* **2003**, *46*, 567–574, doi:10.13031/2013.12946.

28. Zhuang, H.; Nelson, S.O.; Trabelsi, S.; Savage, E.M. Dielectric properties of uncooked chicken breast muscles from ten to one thousand eight hundred megahertz. *Poult. Sci.* **2007**, *86*, 2433–2440, doi:10.3382/ps.2006-00434.

29. Wang, Y.; Wig, T.D.; Tang, J.; Hallberg, L.M. Dielectric properties of foods relevant to RF and microwave pasteurization and sterilization. *J. Food Eng.* **2003**, *57*, 257–268, doi:10.1016/S0260-8774(02)00306-0.

30. Guan, D.; Cheng, M.; Wang, Y.; Tang, J. Dielectric Properties of Mashed Potatoes Relevant to Microwave and Radio-frequency Pasteurization and Sterilization Processes. *J. Food Sci.* **2004**, *69*, FEP30–FEP37, doi:10.1111/j.1365-2621.2004.tb17864.x.

31. Liu, Y.; Tang, J.; Mao, Z. Analysis of bread dielectric properties using mixture equations. *J. Food Eng.* **2009**, *93*, 72–79, doi:10.1016/j.jfoodeng.2008.12.032.

32. Alfaifi, B.; Wang, S.; Tang, J.; Rasco, B.; Sablani, S.; Jiao, Y. Radio frequency disinfestation treatments for dried fruit: Dielectric properties. *LWT - Food Sci.*

Technol. **2013**, *50*, 746–754, doi:10.1016/j.lwt.2012.07.012.

33. Li, R.; Zhang, S.; Kou, X.; Ling, B.; Wang, S. Dielectric properties of almond kernels associated with radio frequency and microwave pasteurization. *Sci. Rep.* **2017**, *7*, 42452, doi:10.1038/srep42452.

34. Guo, W.; Wu, X.; Zhu, X.; Wang, S. Temperature-dependent dielectric properties of chestnut and chestnut weevil from 10 to 4500 MHz. *Biosyst. Eng.* **2011**, *110*, 340–347, doi:10.1016/j.biosystemseng.2011.09.007.

35. Ling, B.; Guo, W.; Hou, L.; Li, R.; Wang, S. Dielectric Properties of Pistachio Kernels as Influenced by Frequency, Temperature, Moisture and Salt Content. *Food Bioprocess Technol.* **2015**, *8*, 420–430, doi:10.1007/s11947-014-1413-8.

36. Zhu, X.; Guo, W.; Jia, Y. Temperature-Dependent Dielectric Properties of Raw Cow's and Goat's Milk from 10 to 4,500 MHz Relevant to Radio-frequency and Microwave Pasteurization Process. *Food Bioprocess Technol.* **2014**, *7*, 1830–1839, doi:10.1007/s11947-014-1255-4.

37. Zhu, Z.; Guo, W. Frequency, moisture content, and temperature dependent dielectric properties of potato starch related to drying with radio-frequency/microwave energy. *Sci. Rep.* **2017**, *7*, 1–11, doi:10.1038/s41598-017-09197-y.

38. Keysight Technologies *Keysight 85070E Dielectric Probe Kit 200 MHz to 50 GHz*; 2014;

39. Gregory, A.P.; Clarke, R.N. Dielectric metrology with coaxial sensors. *Meas. Sci. Technol.* **2007**, *18*, 1372, doi:10.1088/0957-0233/18/5/026.

40. Muñoz, I.; Gou, P.; Picouet, P.A.; Barlabé, A.; Felipe, X. Dielectric properties of milk during ultra-heat treatment. *J. Food Eng.* **2018**, *219*, 137–146, doi:10.1016/j.jfoodeng.2017.09.025.

41. Klein, L.; Swift, C.T. An Improved Model for the Dielectric Constant of Sea Water at Microwave Frequencies. *IEEE J. Ocean. Eng.* **1977**, *2*, 104–111, doi:10.1109/JOE.1977.1145319.

42. Gutierrez-Cano, J.D.; Plaza-Gonzalez, P.; Canos, A.J.; Garcia-Banos, B.; Catala-Civera, J.M.; Penaranda-Foix, F.L. A New Stand-Alone Microwave Instrument for Measuring the Complex Permittivity of Materials at Microwave Frequencies. *IEEE Trans. Instrum. Meas.* **2020**, *69*, doi:10.1109/TIM.2019.2941038.

43. Peñaranda-Foix, F.L.; Catalá-Civera, J.M. Circuital Analysis of Cylindrical Structures Applied to the Electromagnetic Resolution of Resonant Cavities. In *Passive Microwave Components and Antennas*; Vitaliy Zhurbenko, Ed.; IntechOpen, 2010.

44. Penaranda-Foix, F.L.; Janezic, M.D.; Catala-Civera, J.M.; Canos, A.J. Full-wave analysis of dielectric-loaded cylindrical waveguides and cavities using a new four-port ring network. *IEEE Trans. Microw. Theory Tech.* **2012**, *60*, 2730–2740, doi:10.1109/TMTT.2012.2206048.

45. Baker-Jarvis, J.; Janezic, M.D.; Domich, P.D.; Geyer, R.G. Analysis of an Open-Ended Coaxial Probe with Lift-Off for Nondestructive Testing. *IEEE Trans. Instrum. Meas.* **1994**, *43*, 711–718, doi:10.1109/19.328897.

46. Bakhtiari, S.; Qaddoumi, N.; Ganchev, S.I.; Zoughi, R. Microwave Noncontact Examination of Disbond and Thickness Variation in Stratified Composite Media. *IEEE Trans. Microw. Theory Tech.* **1994**, *42*, 389–395, doi:10.1109/22.277431.

47. Blackham, D. V.; Pollard, R.D. An improved technique for permittivity measurements using a coaxial probe. *IEEE Trans. Instrum. Meas.* **1997**, *46*, 1093–1099, doi:10.1109/19.676718.

48. Canós Marín, A.J.; García-Baños, B.; Catalá-Civera, J.M.; Peñaranda-Foix, F.L.; Gutiérrez-Cano, J.D. Improvement in the accuracy of dielectric measurement of open-ended coaxial resonators by an enhanced de-embedding of the coupling network. *IEEE Trans. Microw. Theory Tech.* **2013**, *61*, doi:10.1109/TMTT.2013.2285359.

49. Marks, R.B.; Williams, D.F. A general waveguide circuit theory. *J. Res. Natl. Inst. Stand. Technol.* **1992**, *97*, 533–562, doi:10.6028/jres.097.024.

50. Collin, R.E. *Field theory of guided waves*; 2nd Editio.; John Wiley & Sons: New York, 1990; ISBN 978-0-87942-237-0.

51. Jones, P.L.; Rowley, A.T. Dielectric drying. *Dry. Technol.* **1996**, *14*, 1063–1098, doi:10.1080/07373939608917140.

52. Lagarias, J.C.; Reeds, J.A.; Wright, M.H.; Wright, P.E. Convergence properties of the Nelder-Mead simplex method in low dimensions. *SIAM J. Optim.* **1998**, *9*, 112–147, doi:10.1137/S1052623496303470.

53. Joint Committee for Guides in Metrology *Evaluation of measurement data — Guide to the expression of uncertainty in measurement (GUM)*; 2008; Vol. JCGM 1002;

54. Barba, A.A.; D'Amore, M. Relevance of Dielectric Properties in Microwave Assisted Processes. In *Microwave Materials Characterization*; Costanzo, S., Ed.; IntechOpen, 2012; pp. 91–118.

55. Luan, D.; Tang, J.; Liu, F.; Tang, Z.; Li, F.; Lin, H.; Stewart, B. Dielectric properties of bentonite water pastes used for stable loads in microwave thermal processing systems. *J. Food Eng.* **2015**, *161*, 40–47, doi:10.1016/j.jfoodeng.2015.02.014.

56. Icier, F.; Baysal, T. Dielectrical properties of food materials - 1: Factors affecting and industrial uses. *Crit. Rev. Food Sci. Nutr.* **2004**, *44*, 465–471, doi:10.1080/10408690490886692.

57. Moreiras, O.; Carbajal, A.; Cabrera, L.; Cuadrado, C. *Tablas de composición de alimentos (Food Composition Tables)*; 16th ed.; Ed. Pirámide: Madrid, 2013;

58. Guo, W.; Zhu, X.; Liu, H.; Yue, R.; Wang, S. Effects of milk concentration and freshness on microwave dielectric properties. *J. Food Eng.* **2010**, *99*, 344–350, doi:10.1016/j.jfoodeng.2010.03.015.

59. Nunes, A.C.; Bohigas, X.; Tejada, J. Dielectric study of milk for frequencies between 1 and 20 GHz. *J. Food Eng.* **2006**, *76*, 250–255, doi:10.1016/j.jfoodeng.2005.04.049.

Chapter 4

Detection of Anti-Counterfeiting Markers through Permittivity Maps Using a Micrometer Scale near Field Scanning Microwave Microscope

José D. Gutiérrez-Cano [1], José M. Catalá-Civera [1], Pedro J. Plaza-González [1], Felipe L. Peñaranda-Foix [1]

[1] Instituto ITACA. Universitat Politècnica de València. Camino de Vera s/n.46022 Valencia, Spain.

Sensors 2021, 21(16), 5463

Abstract

This paper describes the use of microwave technology to identify anti-counterfeiting markers on banknotes. The proposed method is based on a robust near-field scanning microwave microscope specially developed to measure permittivity maps of heterogeneous paper specimens at the micrometer scale. The equipment has a built-in vector network analyzer to measure the reflection response of a near-field coaxial probe, which makes it a standalone and portable device. A new approach employing the information of a displacement laser and the cavity perturbation technique was used to determine the relationship between the dielectric properties of the specimens and the resonance response of the probe, avoiding the use of distance-following techniques. The accuracy of the dielectric measurements was evaluated through a comparative study with other well-established cavity methods, revealing uncertainties lower than 5%, very similar to the accuracy reported by other more sophisticated setups. The device was employed to determine the dielectric map of a watermark on a 20 EUR banknote. In addition, the penetration capabilities of microwave energy allowed for the detection of the watermark when concealed behind dielectric or metallic layers. This work demonstrates the benefits of this microwave technique as a novel method for identifying anti-counterfeiting features, which opens new perspectives with which to develop optically opaque markers only traceable through this microwave technique.

4.1 Introduction

Even though digitalization is changing today's society, currency counterfeiting or document fraud are still serious threats that weaken economies and allow criminals to have a certain freedom of movement [1]. Anti-counterfeiting techniques are continuously being improved to incorporate innovative solutions to prevent document fraud, such as luminescent nanowire-based papers, invisible photoluminescent inks or chipless-RFID technologies [2–4].

Banknotes, for example, include a vast number of security features to prevent counterfeiting, consisting in the addition of markers that produce traceable properties in a certain range of the electromagnetic spectrum [5–7], such as watermarks, security threads, holograms, optically variable inks, micro lettering, intaglio printing, and infrared (IR), ultraviolet (UV), or magnetic (MG) marks. Among all these elements, watermarks are one of the most widely recognized security features by the common user. These marks are made by the deposition of cellulosic fibers with different densities during the production of the paper sheet, creating images that are visible when viewed against the light and are usually counterfeited by digital printing on the paper [8], which can be hard to detect by only visual means. Concerning the methods for identifying anti-counterfeiting features, watermarks, security threads, holograms, optically variable inks, and micro lettering are commonly detectable in the visible spectrum. Other security features generate a differential mark in the visible spectrum when illuminated with IR or UV light. These and other additional security features are typically employed by anti-counterfeiting machinery used in stores, ATMs, banks and for forensic verification through IR, UV, MG, or X-ray sensors. However, to the best of our knowledge, the microwave part of the electromagnetic spectrum has not been used before to detect any kind of security feature in document or banknote anti-counterfeiting applications.

Microwave spectrum refers to electromagnetic signals between 300MHz and 300 GHz [9]. Microwave signals might outperform existing anti-counterfeiting technologies at different frequency ranges, since electromagnetic radiation at microwave frequencies shows certain penetrability in some materials, such as metals, dielectrics, or semiconductors, allowing for the development of optically opaque markers that are only traceable with microwave detectors.

Permittivity is a fundamental property of dielectric materials describing their interaction with electromagnetic fields [10] and is the most studied parameter at microwave frequencies. Permittivity studies have historically been linked to telecommunications systems [11]; nevertheless, microwave techniques for non-destructive testing and evaluation have also been frequently employed for a good range of industrial and scientific applications [12–16].

Permittivity measurement techniques have usually been designed to fit the specific size and shape of the samples under analysis [10]. For laminate and homogeneous dielectric surfaces, the preferred methodologies are based on stripline or microstripline resonators [17,18], split cylinder resonators [19–21], split-post dielectric resonators [22], or open-ended coupled coaxial probes [23]. However, for heterogeneous planar materials, near-field scanning microwave microscopes (NSMM) can provide dielectric property maps, directly related to the different components of the materials under test (MUT).

NSMM devices can measure the electromagnetic response of materials on a length scale significantly smaller than the wavelength of the emitted signal [24]. This involves a probe tip size (D) shorter than the probe-to-sample distance (r) and far shorter than the wavelength of the electromagnetic wave (λ) in order to ensure near-field radiation ($D \leq r << \lambda$). Thus, the spatial resolution is given by D instead of λ.

The basic design of a typical NSMM comprises a near-field evanescent probe, a microwave source and detector (typically a vector network analyzer, or VNA), and a positioning (X–Y axis) stage to perform the pixel-by-pixel scanning of a sample of planar materials [25]. Even though there is a remarkable diversity of structures utilized as apertures for the evanescent probes, sharp coaxial tips are the most widely employed [24–26]. Two main detection modes are used depending on the probe configuration [24]. The non-resonant mode involves a transmission line section wherein detection is achieved by monitoring the electromagnetic wave reflected or transmitted from the sample. The resonant configuration, on the other hand, tracks the changes in the resonance parameters (resonant frequency and quality factor) caused by variations in the sample properties.

There is also diversity in the way that the measurable quantities—reflection, transmission, or resonance parameters—are related to the physical properties of the materials, including permittivity. These works include procedures such as lumped element models, full-wave analysis, or the cavity perturbation method (CPM) [27–29].

Recent developments in near-field scanning microwave microscopy have focused on increasing the special resolution to the nanoscale level [30]. To achieve such a high resolution, employing a distance-following technique is essential to keep the probe either in soft contact or at a distance of only a few nanometers from the sample [26]. Thus, NSMM devices with nanometer resolution require the support of a different nanoscale microscope technology, such as that of atomic force microscopes (AFM) or scanning tunneling microscopes (STM), to meet the distance-following needs. However, the detection of anti-counterfeiting features, especially watermarks, would require lower resolutions than nanoscale, and can benefit from a micrometer scale NSMM device with a much simpler and compact set-up, wherein permittivity measurements on larger non-homogeneous samples could be performed.

In this work, we describe the unprecedented use of microwave energy (technology) for the identification of markers on anti-counterfeiting applications. We employed a micrometer scale NSMM specially developed to detect the density variations of paper inside a banknote watermark through permittivity maps. In addition, the unique penetration capabilities of electromagnetic waves at microwave frequencies allowed the detection of new opaque markers hidden behind dielectric or metallic layers, only traceable with this microwave technique.

The developed NSMM device allows for the permittivity measurements of heterogeneous planar materials around the ISM microwave frequency of 2 GHz. An in-house vector network analyzer was embedded in the device to measure the response of the near-field probe, thereby avoiding the need for a full-featured VNA and making the instrument portable and easy to use. Unlike previous approaches, the permittivity calculation made use of a displacement laser and an enhanced CPM with calibration coefficients for

different tip-to-sample distances, avoiding the need of distance-following techniques and increasing the robustness of the system.

Additionally, the detection capabilities of the proposed device can provide scientists and industrialist with a convenient tool for a wide range of sensing applications to analyze and characterize heterogeneous planar objects.

4.2 Design of the NSMM

4.2.1 The Near-Field Microwave Probe

Fig. **1** shows a drawing of the near-field evanescent probe implemented in the NSMM. The probe was designed as an open λ/2 coaxial resonator [26]. A section of a standard rigid RG405 coaxial cable was used to manufacture the central section of the resonator.

The near-field radiating end of the coaxial aperture was sharpened to increase the spatial resolution when positioned close to the MUT, around 25 µm [31]. An SMA female connector was fitted to the other end of the RG405 coaxial cable to connect the resonator to the microwave emitter and receiver. Taking this set-up into account, we fixed the length of the cavity to 55.4 mm for an operating frequency of around 1.85 GHz, choosing the first resonant frequency of the coaxial resonator.

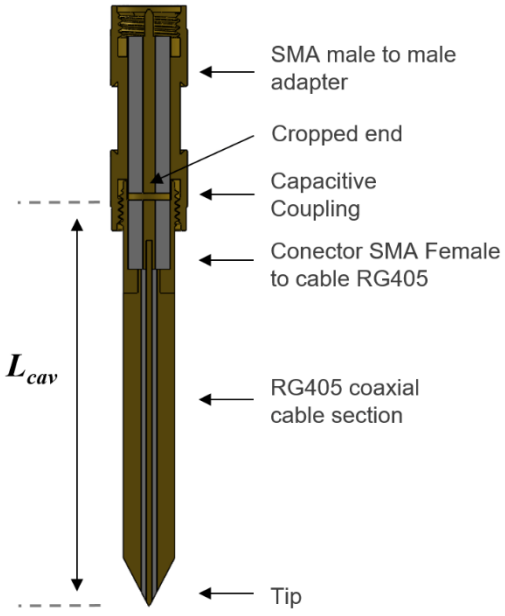

Fig. **1**: Geometry of the coaxial resonator implemented in the near-field microwave microscope, L_{cav} = 55.4 mm and R_{tip} ≈ 25 µm.

The feeding network used to couple the microwave energy into the resonator was a capacitive coupling gap created by bringing the open end of the resonator close to another open-ended section, implemented by cutting the inner conductor of a male–male SMA adapter.

Finally, this SMA adapter was connected to the microwave analyzer that generates the microwave signals required by the evanescent probe to interact with the MUT and receive a response to be able to establish the resonator's resonance parameters.

4.2.2 Single-Port Microwave Analyzer

Fig. **2** depicts a schematic diagram of the electronic module developed to operate the NSMM device. The generation and reception of microwave signals is comprised of four main subsystems: microwave transmitter, microwave receiver, separation network, and control unit.

The microwave transmitter was based on an ADF4113 (Analog Devices) frequency synthesizer, which, together with an external loop filter and a voltage-controlled oscillator (ROS-2500 Mini-Circuits, Brooklyn, NY, USA), formed a complete PLL able to run frequency sweeps around the resonance of the microwave microscope (2 GHz). The separation network included two directional couplers (BDCA 1-7-33+ from Mini-Circuits,

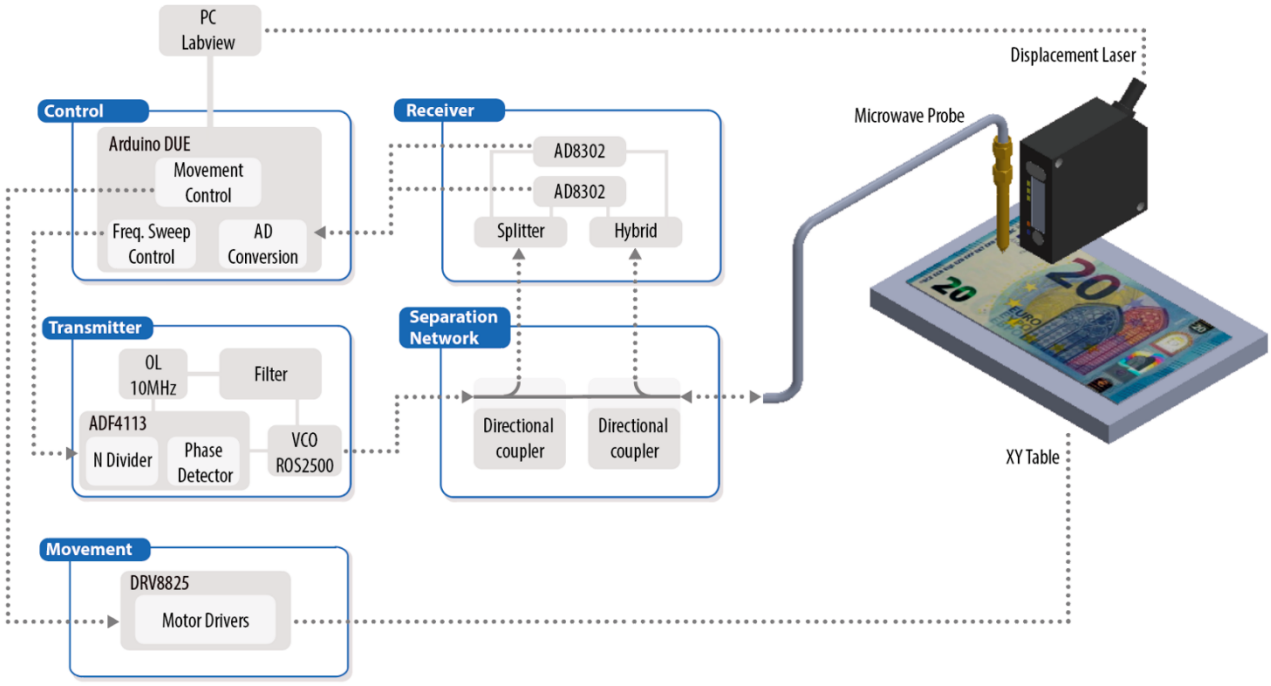

Fig. **2**: Schematic diagram of the in-house vector network analyzer for measuring the reflection (S_{11}) of the near-field microwave microscope.

Brooklyn, NY, USA) that were used to isolate the reference signal from the transmitter and the reflected signal from the near-field coaxial cavity.

These two signals were compared inside the receiver, which was based on an AD8302 RF/IF gain and phase detector (Analog Devices, Norwood, MA, USA) [32], providing analog outputs depending on the magnitude loss ratio and the phase difference between inputs. All the signals were converted to digital by a control unit based upon a microprocessor system and connected to a personal computer for further processing. Together, all these devices made up an in-house affordable single port VNA (reflectometer) similar to the system reported in [33].

In this new design, the PIC16C773 microcontroller of [33] was substituted by an Arduino DUE open-source electronics platform based on a 32-bit ARM core microcontroller. This platform allowed a convenient integration of the microwave devices and the mechanical X–Y positioning system, which thus reduced the latency times associated with the synchronizing of all the parts and increased the scanning speed.

The Arduino board and the LabVIEW-based software controlled the whole measurement process from the output magnitude and phase signals of the receiver to the calculating of the resonance parameters and dielectric properties, as well as displaying the results.

A standard calibration procedure with an OSL calibration kit (85052B Standard Mechanical Calibration Kit-3.5 mm, Keysight Technologies, Santa Rosa, CA, USA) was set from 1.8 to 1.85 GHz to cover the frequency response of the probe (see Section 4.3.1).

4.2.3 Positioning Stage

For the positioning subsystem, we used a commercial XY-stage (KT-70, proxxon) driven by two stepper motors and drivers (DRV8825, Texas Instruments, Dallas, TX, USA), which allowed for a pixel-by-pixel scanning with a maximum scan range of 150 mm × 70 mm and a resolution of 5 µm.

A vacuum table was attached to the XY-stage to fix the documents during the measurement procedure and avoid disturbances from folds in the documents or planar materials under test. The resonant probe was attached to the central axis of the XY-stage, employing a vertical, manually-driven micrometric positioner. A commercial laser displacement sensor (HL-G103-SJ, Panasonic, Osaka, Japan) with a resolution of 0.5 µm was placed close to the aperture of the microwave probe in order to precisely measure the tip-to-sample distance.

The LabVIEW-based software was used to define the scanning parameters (area to scan, frequency sweep configuration…) and load them into the Arduino board. Next, the Arduino firmware autonomously controlled the scan process synchronized with the calculation of microwave parameters. The picture in Figure 3 shows the developed integrated NSMM system that operates as a standalone portable measurement instrument.

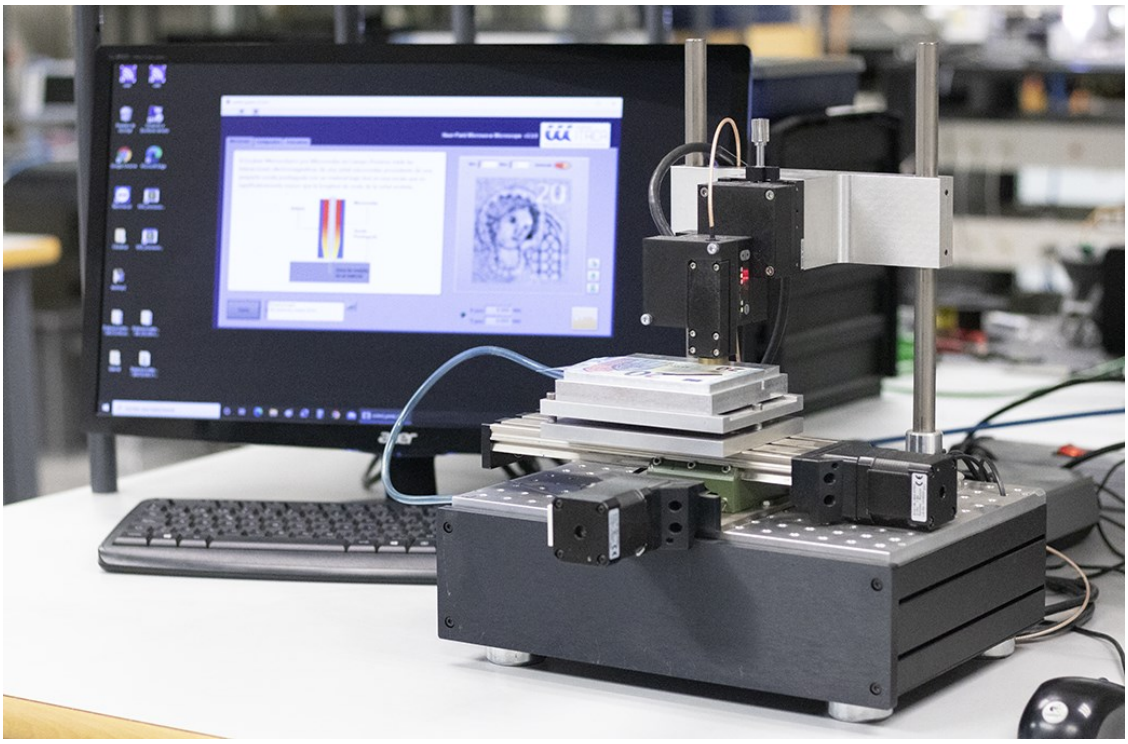

Fig. **3**: Picture of the near-field microwave microscope system.

4.3 Permittivity Measurements with NSMM

4.3.1 Microwave Probe Response

The response of the near-field microwave resonator, described in the previous section, was assessed by measuring the resonant frequency (fr) and Q-factor (Q) parameters of some reference materials, covering a wide range of dielectric properties (see Table 1) as a function of the tip-to-sample distance. The size of the rod-shaped materials (15 mm high and with a diameter of 9.8 mm) was sufficient enough to be considered as infinitely wide and thick materials for the probe tip size and tip-to-sample distances [25,34]. The resonance parameters were determined from the reflection measurements by means of the linear fractional curve fitting procedure published by Kajfez [35,36]. Fig. **4** shows the resonant frequency variation as a function of the tip-to-sample distance for the different materials measured. Because of the radiation characteristic of the open-ended coaxial probe tip, the quality factor calculated from the measurements exhibited small variations for the selected tip-to-sample distances.

The maximum frequency shift between the measurement of air and the material with the highest dielectric constant, Temex E5980 (67.39), occurred for the smaller tip-to-sample distance (see Fig. **4**). For the soft contact distance (0 μm), the maximum detected deviation was 16 MHz. From that point on, the maximum frequency shift decreased exponentially as the tip-to-sample distance increased.

Based on these results, the primary probe-to-sample distance was selected to be 100 μm, leaving the Z stage fixed during the rest of the measurements. At that tip-to-sample distance, the maximum frequency shift was 5 MHz. Even though this variation offered a

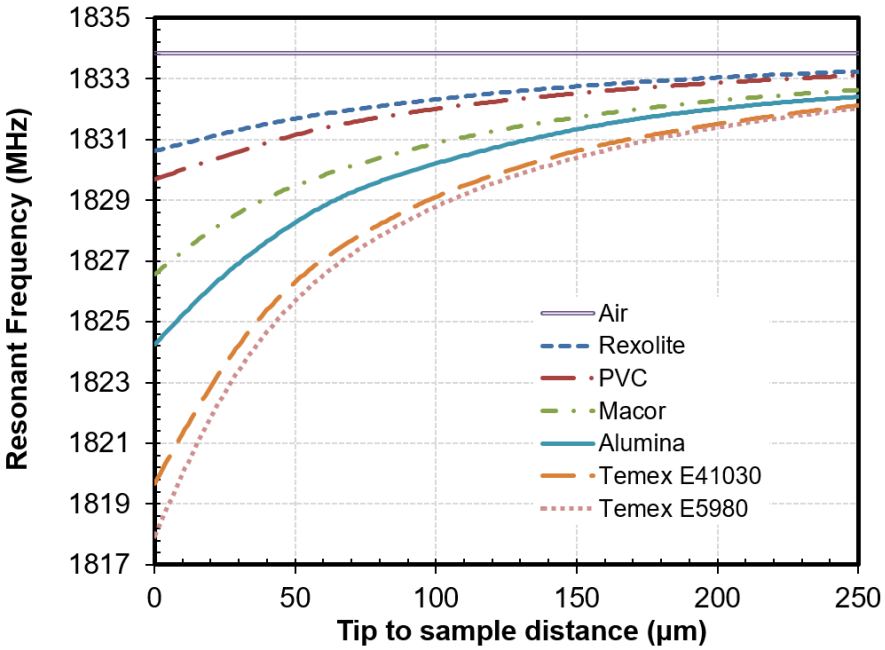

Fig. **4**: Variation of the resonant frequency as a function of the tip-to-sample distance for different reference materials.

good resolution throughout the complete permittivity range, the measurement resolution improved for those materials with lower dielectric constant values. For instance, at 100 µm, the frequency deviation exhibited between Rexolite and PVC, with a dielectric constant of 2.54 and 3.09 respectively, was 0.3 MHz, which is similar to the deviation reached between Temex E41030 and Temex E5980, with dielectric constant values of 28.28 and 67.25, respectively.

4.3.2 Cavity Perturbation Method (CPM)

Cavity perturbation method (CPM) was applied to determine the permittivity of the MUT from the measured resonance parameters. Since the earliest work on this procedure published by Bethe and Schwinger in 1943 [37], CPM has become one of the most widely employed techniques used to calculate dielectric properties using microwave resonators. The method assumes that the electromagnetic field of the resonant cavity is barely perturbed by placing the MUT in the structure. Under this premise, dielectric properties can be calculated using the relative shift of the resonance parameters with and without the MUT.

In an NSMM, the volume of the fields inside the cavity obviously outweighs their volume in the MUT and, thus, the CPM can also be employed to analyze a near-field cavity resonator [24]. Most of the CPM reported in the literature for NSMM structures made use of the theoretical approach proposed by Gao and Xiang [27], who studied the fields inside the sample, assuming an excitation illuminated by a spherical tip. They assumed an

iterative image charge problem and solved the CPM equations to relate the fr and Q shifts to the permittivity of the MUT and other parameters depending on the tip-to-sample distance and the size of the probe. However, some authors have described issues in this model for longer tip-to-samples distances [34] and for some apertures that cannot be described with a spherical tip.

For the specific geometry of Figure 1, we assumed a quasi-static electric field inside the MUT [38] and related the permittivity of the MUT to the relative shift in the resonant frequency and the quality factor according to Khanna et al. [39], with the following formulas:

$$\varepsilon' = 1 + \frac{-\frac{\Delta f}{f}\left(\eta + N\frac{\Delta f}{f}\right) - N\left[\Delta\left(\frac{1}{2Q}\right)\right]^2}{\left(\eta + N\frac{\Delta f}{f}\right)^2 + N^2\left[\Delta\left(\frac{1}{2Q}\right)\right]^2} \quad (1)$$

$$\varepsilon'' = \frac{\eta\Delta\left(\frac{1}{2Q}\right)}{\left(\eta + N\frac{\Delta f}{f}\right)^2 + N^2\left[\Delta\left(\frac{1}{2Q}\right)\right]^2} \quad (2)$$

where ε' = dielectric constant (dimensionless); ε'' = loss factor (dimensionless); f = resonant frequency (s^{-1}); Q = quality factor (dimensionless); η = sample filling factor (dimensionless); N = sample depolarization factor (dimensionless). The relative shifts can be written as follows [40]:

$$\frac{\Delta f}{f} = \frac{f_s - f_0}{f_s} \quad (3)$$

$$\Delta\left(\frac{1}{2Q}\right) = \frac{f_0}{f_s}\cdot\frac{1}{2}\cdot\left(\frac{1}{Q_s} - \frac{1}{Q_0}\cdot\frac{f_s^2}{f_0^2}\right) \quad (4)$$

where f_0 and Q_0 are the resonance frequency and quality factor of the open-air cavity, respectively, and f_s and Q_s are the cavity's parameters with a dielectric material placed near the tip of the probe.

For an infinite size MUT, the parameters N and η depend on several factors, such as the resonant mode, the geometry of the cavity, or the tip-to-sample distance, and are usually calibrated by measuring reference materials of known dielectric properties [41].

Three materials—air, Macor (ε' = 5.68), and Temex E5980 (ε' = 67.25)—were selected for calibrating the N and η parameters at a tip-to-sample distance of 100 µm. Nevertheless, the irregular height of the material, as well as defects in the horizontality of the base that holds the sample, may cause variations in the tip-to-samples distances around the established gap of 100 µm. For this reason, the calibration process was repeated for several tip-to-sample distances using the laser measurement device to fix the distance.

Fig. **5** shows the variation of the CPM *N* and *η* parameters as a function of the tip-to-sample distance. As illustrated, the two smooth curves were thoroughly adjusted with two polynomials of second and third degree, in order to find any value of these parameters that was in the vicinity of 100 µm. With the help of these curves, once the reading of the resonator and the laser had been recorded, the permittivity value of the MUT could be calculated in a straightforward manner for each position from (1) and (2).

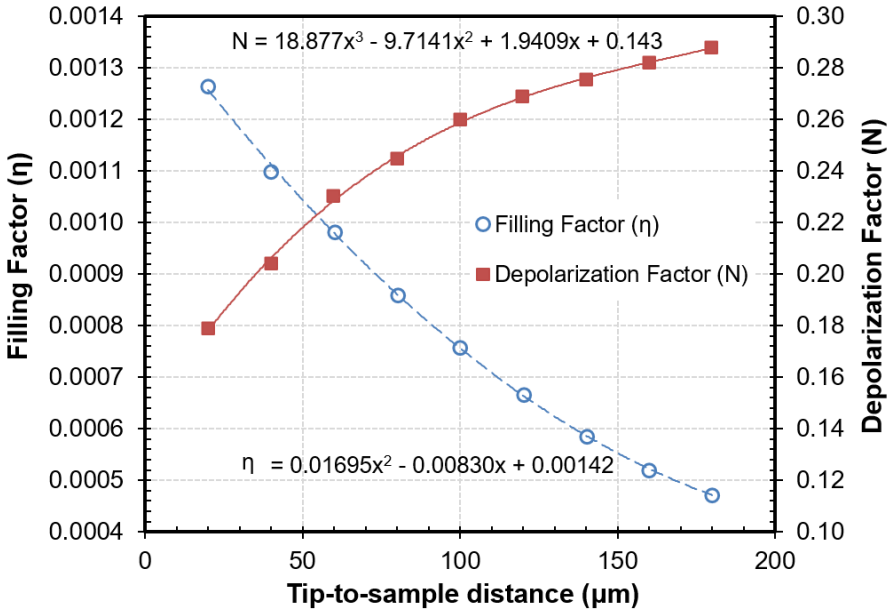

Fig. **5**: Calibration parameters, *η* and *N*, of the cavity perturbation method determined with reference samples as a function of the tip-to-sample distance (referred to as x in the regression equations).

4.4 Experimental Results

4.4.1 Dielectric Measurements

To assess the performance of the proposed NSMM measurement setup and the CPM calibration, the permittivity values of six reference specimens were determined from resonance measurements at different tip-to-sample distances around 100 µm.

The materials employed to undertake this assessment were the set of dielectric materials whose resonant frequencies were measured in Section 4.3.1, covering a broad range of permittivity values. The dielectric materials were placed on the base of the microscope and centered on the axis of the coaxial probe. With the aid of the laser, the Z-axis was moved from the soft-contact point to the studied tip-to-sample distances. From the displayed distance, the *N* and *η* values of each measurement were extrapolated from Figure **5**, and the permittivity values were determined by means of the CPM technique

from the resonance parameters provided by the reflectometer. All measurements were performed at 23 °C.

Table I shows the results of dielectric constant of all considered samples. The loss factor results were omitted from this study because of the weak sensitivity of the quality factor achieved with these materials for this probe size and tip-to-sample distances. To evaluate the accuracy of the results, all dielectric materials were also measured, as references, in a partially loaded cylindrical cavity [42] to evaluate the accuracy of the results.

Table I. Dielectric property results of reference materials and associated standard deviations.

	Tip-to-Sample Distance (μm)												
Material	20	40	60	80	100	120	140	160	180	$\varepsilon'_{mean} \pm StdDev$	$StdDev\%$	ε'_{ref}	$\left\|\frac{\Delta\varepsilon'}{\varepsilon'}\right\|\%$
Air	1.00	1.00	1.00	1.00	1.00	1.00	1.00	1.00	1.00	1.00 ± 0.00	0.00	1.00	0.00
Rexolite	2.52	2.48	2.50	2.52	2.53	2.53	2.54	2.54	2.51	2.52 ± 0.02	0.83	2.53 ± 0.05	0.46
PVC	3.11	3.07	2.98	3.01	3.02	3.03	3.05	3.05	3.01	3.04 ± 0.04	1.30	3.09 ± 0.06	1.70
Macor	5.40	5.51	5.69	5.82	5.79	5.88	5.93	5.92	5.67	5.73 ± 0.18	3.23	5.68 ± 0.11	0.96
Alumina	9.11	9.31	8.59	8.86	9.13	9.27	8.96	8.73	8.77	8.97 ± 0.25	2.82	8.94 ± 0.18	0.33
Temex E41030	29.43	27.80	29.52	28.43	29.34	27.70	29.04	29.07	27.82	28.68 ± 0.75	2.66	28.28 ± 0.56	1.43
Temex E5980	67.10	68.80	67.90	67.43	68.19	66.30	67.62	67.14	66.02	67.39 ± 0.88	1.30	67.25 ± 1.34	0.21

The dielectric constant results agreed very well with the reference values in that all the materials and tip-to-sample distances displayed similar deviations. For short tip-to-sample distances, miss-positioning of the vertical axis caused deviations in the resonant frequency that were compensated for with the higher frequency shifts. On the other hand, for longer tip-to-sample distances, resonance deviations, due to inaccuracies when determining the tip-to-sample distances, became less relevant, but the influence on the dielectric constant increased because of the reduced frequency shifts. The error achieved for each material, defined as the absolute difference between the measured mean value and the reference value ($|\Delta\varepsilon'/\varepsilon'|\%$), was below 2%, and the standard deviation was mostly below 3%. Withal, each individual deviation for each measurement was slightly higher, with all the results falling within 5% of the reference value. This uncertainty is comparable to the uncertainty reported in [34], which achieved accuracies below 10% with a sophisticated tip-to-sample control system and a full-featured VNA as a measurement device.

4.4.2 Watermark Dielectric Maps

The developed NSMM device was used to scan the variations of permittivity of banknote watermarks, one of the most readily recognized security features available to the user for the authentication of banknotes or other public documents, such as passports. In this study, we utilized a second series 20 EUR banknote, which contains a watermark

depicting a portrait of Europa, a figure from Greek mythology, as well as a Gothic-style window and the value numeral of the banknote.

The banknote was placed on the metallic structure of the XY-stage equipped with a suction vacuum table, which fixed the document during the scanning. With the aid of the displacement laser, the tip of the probe was placed at a distance of 100 μm from the surface of the banknote. The XY-stage covered an area of 33 mm × 29 mm with a step of 100 μm. The displacement laser information was employed to retrieve the appropriate CPM parameters for the tip-to-sample distance variations during the scan. Fig. **6**a shows the dielectric image of the watermark area obtained through the CPM calculation of the resonance parameter variations of the scan. For comparison, Fig. **6**c also shows a picture of the measured watermark using transmitted light. To have a numeric reference, dielectric properties of paper money were measured with a split-post dielectric resonator [43], achieving the value: 2.89 ± 0.2 − j0.3 ± 0.02.

The scanned dielectric image allows the watermark to be clearly recognized if compared with the image recovered through optical means. The measured dielectric constant values (from 6 to 18) are higher than the reference value, which indicates that the microwave signal penetrates through the whole banknote thickness and is then reflected by the metal base, influencing measured resonance parameters.

In order to avoid these reflections, the metal base below the banknote was substituted by a PVC (polyvinyl chloride) perforated table, whose permittivity—3.09 ± 0.06 − j0.023 ± 0.002—was fairly similar to the dielectric properties of the bulk banknotes. Figure **6**b shows the dielectric constant response of the NSMM device for the watermark and setup described above, except for the material of the XY-base. The watermark pattern was recovered accurately again, albeit exhibiting a slightly lower sharpness. The dielectric constant values ranged from 2 for the lightest parts of the watermark (lower fiber densities) to 3.5 for the darkest parts (higher fiber densities). These results are in line

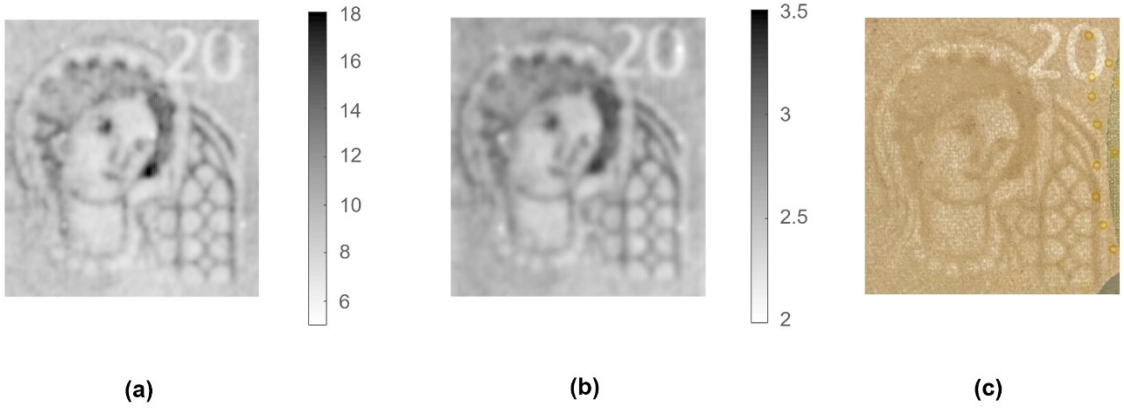

Fig. **6**: Images of the watermark included in a 20 EUR banknote: (a) dielectric image measured with the metallic base, (b) dielectric image measured with the PVC base, and (c) picture of the measured watermark using transmitted light.

with those measured with the split-post dielectric resonator and other values reported in the literature [44,45].

The penetration of microwaves was able to reproduce the density changes inside the papers and therefore NSMM devices could offer an alternative technology to identify anti-counterfeiting watermarks on banknotes. This capability could predict the detection of watermarks even when hidden behind appended layers. Next, we examined two different options to detect optically opaque markers.

In the first experiment, the watermark was partially hidden by a black mark drawn with a felt pen to study the influence of a thin ink coating over the watermark, as depicted in Fig. **7**a. As in the previous experiments, the sample was fixed by means of a vacuum suction system on the XY-table at a distance of 100 μm below the tip of the probe, collecting the microwave response over a 33 mm × 29 mm area. In these trials, we employed the metallic base of the NSMM. Although the values retrieved with the metal arrangement provided an effective dielectric map, the wider response of this setup served to increase its robustness for this specific application.

The obtained response, shown in Fig. **7**b, was very similar to the image shown in Fig. **6**a, with dielectric values ranging from 5 to 18. The mark made on the watermark did not cause any appreciable effect on the permittivity maps, demonstrating that the penetration of the microwave energy was not disturbed by such a thin dielectric coating.

Considering the previous results, in the second experiment, we employed a metallic cover to hide the watermark and complicate any reading by optical means. The mask

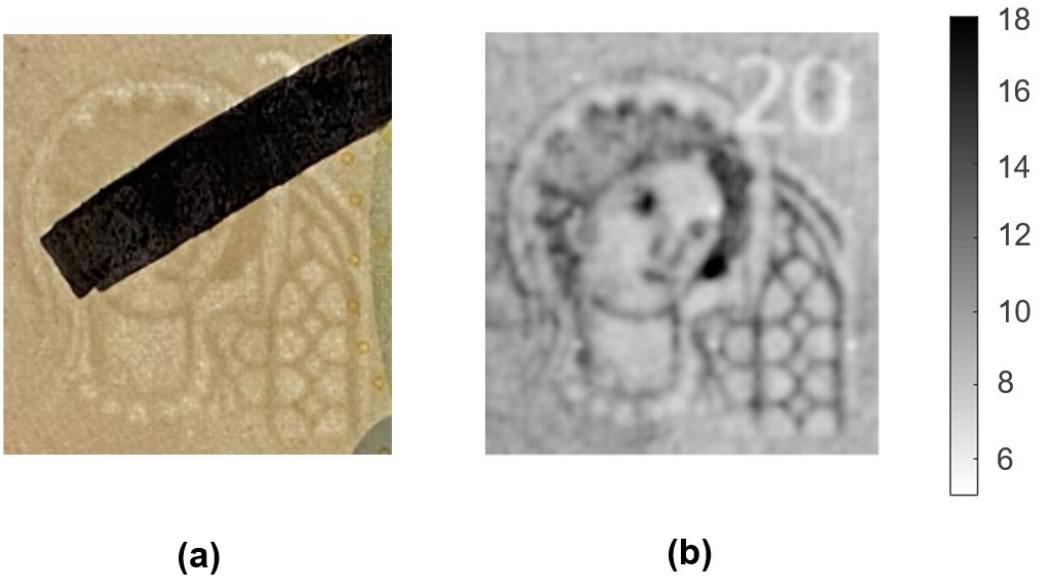

Fig. **7**: Images of the watermark included in a 20 EUR banknote partially covered with a black mark: (a) picture of the studied watermark using transmitted light and (b) dielectric image obtained with the metallic base.

consisted of a piece of a paper sheet (20 g/m2) painted with a layer of silver conductive paint (123-9911, RS Components, Corby, UK). As long as the thickness of the metallic layer was less than the skin depth of the conductive paint at the working frequency (~35 μm) [9], microwave energy could propagate through the mask and detect the changes in the density of the banknote watermark placed beneath it. As in the previous experiments, the tip-to-sample distance was 100 μm, but, in this case, this distance was measured from the surface of the metallic cover, and thus the separation between the watermark and the tip of the probe was slightly higher.

The image recovered from the concealed sample (Fig. **8**b) displayed once again a reliable overall quality, with permittivity values ranging from 8 to 40. The influence of the metallic ink pushed up the dielectric values and extended the dielectric range, due to the saturation in the dielectric response as permittivity increased, as mentioned in Section 4.3.1. However, we observed a reduced spatial resolution due to the attenuation of the microwave signals passing through the metal film and the larger tip-to-sample distance. The non-uniformity of the metallic ink mask could have an influence as well.

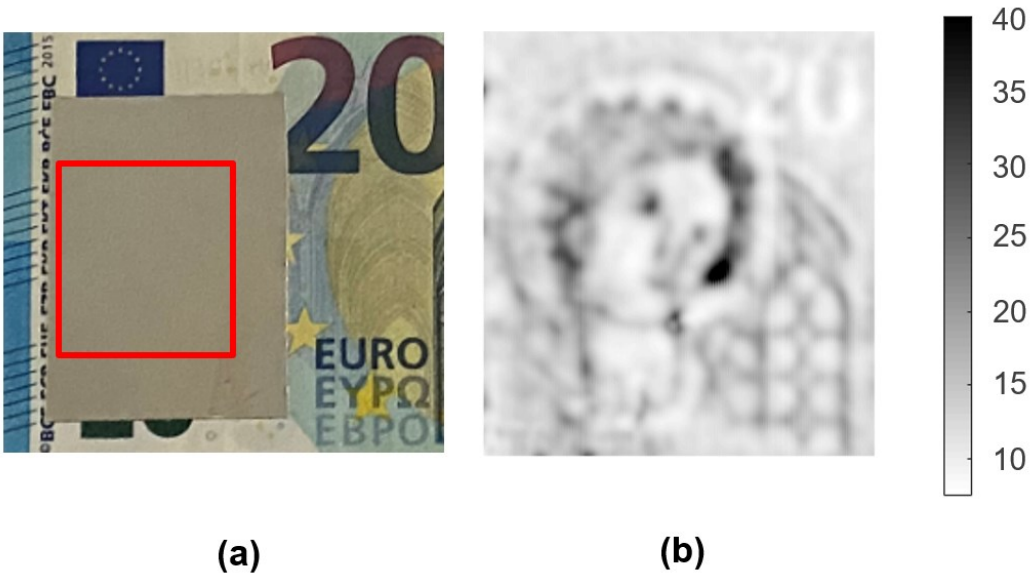

Fig. **8**: Images of the watermark included in a 20 EUR banknote partially covered with a metallic mask: (a) picture of the measured watermark and (b) dielectric image obtained with the metallic base.

4.4.3 Dielectric Scans at Single Frequency

The permittivity maps, represented in previous sections, required a frequency sweep around the resonant peak of the cavity to measure the reflection coefficient, calculate the f_r and Q, and, eventually, to calculate the permittivity values. This process can last around 2 s per sweep, which makes the whole process very time consuming. However, surface scans can significantly reduce the overall scanning time by using the magnitude or phase of the reflection coefficient at a fixed frequency in the slope of the resonance. Although permittivity cannot be calculated with this working procedure, it could nevertheless still be valid for some sensing applications.

Fig. **9**a,b shows the images generated by the NSMM device of the watermarks represented in Figure **7**a and Figure **8**a, respectively, using the magnitude values of the reflection coefficient measured by the reflectometer at a single frequency (f = 1.82 GHz), located on the left side of the resonance peak. In this case, the laser was only employed to fix the central tip-to-sample distance without considering any variation during the scan.

The measurement image of the watermark covered with dielectric ink (Fig. **9**a) was very similar to the permittivity map created with the full frequency sweep (Fig. **7**a). The image had excellent overall quality, and, even at certain points in the darker areas, the image of the dielectric mark improved due to the higher slope of the resonance. It was also observed that the left part of the image had a darker region than the right one, due to a slight non-horizontality of the XY table. The measurement of the watermark covered with metallic ink yielded an image much like the dielectric response shown in Fig. **8**b with the same effects highlighted before.

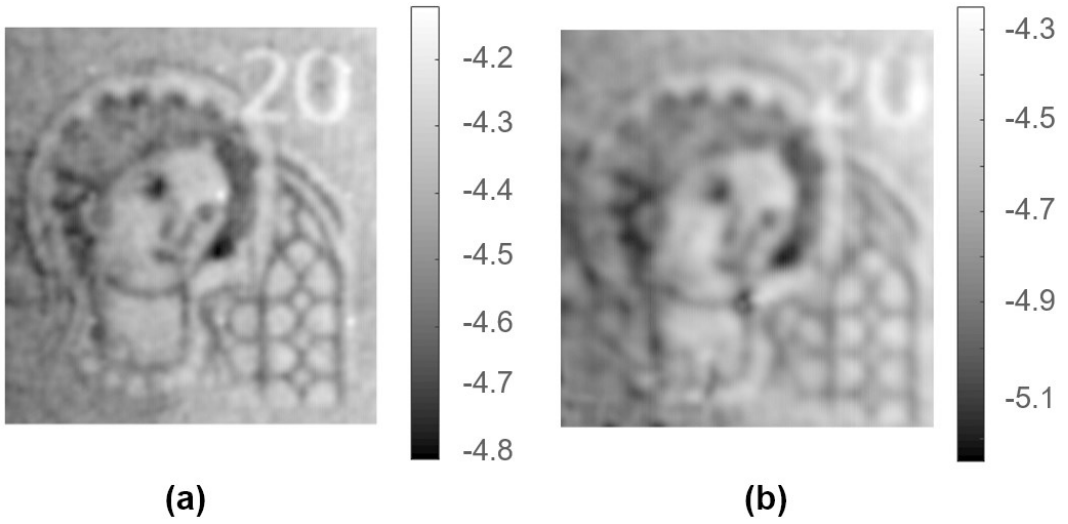

Fig. **9**: Images of the watermark included in a 20 EUR banknote using the magnitude (dB) of the reflection coefficient at a fixed frequency of 1.82 GHz and the metallic base; (a) watermark partially covered with a black mark and (b) partially covered with a metallic mask.

4.5 Conclusions

In this work, we describe for the first time the use of microwave technology for the identification of markers on anti-counterfeiting applications. Microwave detection of banknote watermarks was conducted with a robust, portable, and standalone NSMM device at the micrometer scale, specially developed to determine permittivity maps of heterogeneous banknotes or paper documents around the frequency of 2 GHz.

The near-field microwave probe was designed as an open-ended coaxial resonator with a tapered inner conductor. An in-house microwave reflectometer was developed in the microscope, thus avoiding the need for a full-featured VNA and allowing for standalone

functionality. A micrometer-resolution XY-table and a displacement laser for vertical positioning completed the measurement setup of the NSMM.

A novel methodology, combining the information of the displacement laser and a modification of the CPM theory with calibration coefficients for different tip-to-sample distances was proposed to determine dielectric property maps of banknote watermarks, avoiding the need for more advanced distance-following techniques. Future work will consider finite thickness of laminate materials. Accurate dielectric measurements of reference materials revealed relative errors below 5%, similar to the deviations obtained with much more complex implementations.

The NSMM device was employed to measure the permittivity map of the watermark of a second series 20 EUR banknote under different conditions. The penetration of the microwaves was able to reproduce the density changes inside the papers, offering a practical alternative for the detection of anti-counterfeiting watermarks on banknotes. In addition, the capability of microwave energy to detect markers behind dielectric or even metallic layers was demonstrated, which opens new possibilities to develop more advanced security features such as watermarks concealed behind optically opaque elements, undetectable through traditional optical procedures. The single frequency approach also provided high-quality images with shorter measurement times, and thus highlights the convenience of this procedure for sensing applications.

The developed NSMM could also be employed as a fast and standalone tool to obtain permittivity maps of planar materials in a broad range of sensing applications.

4.6 Funding

This paper has been financially supported through the grant reference BES-2016-077296 of the call Convocatoria de las ayudas para contratos predoctorales para la formación de doctores de 2016 by Ministerio de Economía y Competitividad (MINECO) and by European Social Funds (ESF) of European Union, and the project SEDMICRON—TEC2015-70272-R (MINECO/FEDER) supported by Ministerio de Economía y Competitividad (MINECO) and by European Regional Development Funds (ERDF) of European Union.

4.7 References

1. Interpol Counterfeit currency and security documents Available online: https://www.interpol.int/en/Crimes/Counterfeit-currency-and-security-documents (accessed on May 20, 2021).
2. Yang, R.L.; Zhu, Y.J.; Chen, F.F.; Dong, L.Y.; Xiong, Z.C. Luminescent, Fire-Resistant, and Water-Proof Ultralong Hydroxyapatite Nanowire-Based Paper for Multimode Anticounterfeiting Applications. *ACS Appl. Mater. Interfaces* **2017**, *9*, 25455–25464, doi:10.1021/acsami.7b06835.
3. Abdollahi, A.; Alidaei-Sharif, H.; Roghani-Mamaqani, H.; Herizchi, A. Photoswitchable fluorescent polymer nanoparticles as high-security anticounterfeiting materials for authentication and optical patterning. *J. Mater. Chem. C* **2020**, *8*, 5476–5493, doi:10.1039/d0tc00937g.

4. Herrojo, C.; Paredes, F.; Mata-Contreras, J.; Martín, F. Chipless-RFID: A review and recent developments. *Sensors (Switzerland)* **2019**, *19*, 3385, doi:10.3390/s19153385.

5. European Central Bank Banknotes Denominations Available online: https://www.ecb.europa.eu/euro/banknotes/denominations/html/index.en.html#es2-020 (accessed on May 20, 2021).

6. Bruna, A.; Farinella, G.M.; Guarnera, G.C.; Battiato, S. Forgery detection and value identification of Euro banknotes. *Sensors* **2013**, *13*, 2515–2529, doi:10.3390/s130202515.

7. Lee, J.W.; Hong, H.G.; Kim, K.W.; Park, K.R. A survey on banknote recognition methods by various sensors. *Sensors* **2017**, *17*, 313, doi:10.3390/s17020313.

8. European Central Bank Real or Fake? Available online: https://www.ecb.europa.eu/euro/changeover/lithuania/shared/files/Real_or_Fake_EN.pdf (accessed on May 20, 2021).

9. M. Pozar, D. *Microwave Engineering*; 2nd ed.; John Wiley & Sons, Inc.: New York, NY, 1998; ISBN 0-471-17096-8.

10. Krupka, J. Frequency domain complex permittivity measurements at microwave frequencies. *Meas. Sci. Technol.* **2006**, *17*, R55–R70, doi:10.1088/0957-0233/17/6/R01.

11. *Dielectric Materials for Wireless Communication*; Sebastian, M.T., Ed.; 1st edn.; Elsevier: UK, 2008;

12. García-Baños, B.; Catalá-Civera, J.M.; Canós, A.J.; Peñaranda-Foix, F. Design rules for the optimization of the sensitivity of open-ended coaxial microwave sensors for monitoring changes in dielectric materials. *Meas. Sci. Technol.* **2005**, *16*, 1186–1192, doi:10.1088/0957-0233/16/5/019.

13. Gutiérrez, J.D.; Catalá-Civera, J.M.; Bows, J.; Peñaranda-Foix, F.L. Dynamic measurement of dielectric properties of food snack pellets during microwave expansion. *J. Food Eng.* **2017**, *202*, 1–8, doi:10.1016/j.jfoodeng.2017.01.021.

14. Chavanne, X.; Frangi, J.P. Autonomous sensors for measuring continuously the moisture and salinity of a porous medium. *Sensors* **2017**, *17*, 1094, doi:10.3390/s17051094.

15. Pérez-Campos, R.; Fayos-Fernández, J.; Lozano-Guerrero, A.J.; Martínez-González, A.; Monzó-Cabrera, J.; Mediavilla, I.; Peña-Carro, D.; Esteban-Pascual, L.S. Permittivity measurements for cypress and rockrose biomass versus temperature, density, and moisture content. *Sensors* **2020**, *20*, 4684, doi:10.3390/s20174684.

16. Vergnano, A.; Godio, A.; Raffa, C.M.; Chiampo, F.; Tobon Vasquez, J.A.; Vipiana, F. Open-ended coaxial probe measurements of complex dielectric permittivity in diesel-contaminated soil during bioremediation. *Sensors* **2020**, *20*, 6677, doi:10.3390/s20226677.

17. García-Baños, B.; Cuesta-Soto, F.; Griol, A.; Catalá-Civera, J.M.; Pitarch, J. Enhancement of sensitivity of microwave planar sensors with EBG structures. *IEEE Sens. J.* **2006**, *6*, 1518–1522, doi:10.1109/JSEN.2006.884506.

18. Al-Behadili, A.A.; Mocanu, I.A.; Codreanu, N.; Pantazica, M. Modified split ring

resonators sensor for accurate complex permittivity measurements of solid dielectrics. *Sensors* **2020**, *20*, 6855, doi:10.3390/s20236855.

19. Kent, G. Nondestructive permittivity measurement of substrates. *IEEE Trans. Instrum. Meas.* **1996**, *45*, doi:10.1109/19.481319.

20. Janezic, M.D.; Baker-Jarvis, J. Full-wave analysis of a split-cylinder resonator for nondestructive permittivity measurements. *IEEE Trans. Microw. Theory Tech.* **1999**, *47*, 2014–2020, doi:10.1109/22.795077.

21. Marques-Villarroya, D.; Penaranda-Foix, F.L.; Garcia-Banos, B.; Catala-Civera, J.M.; Gutierrez-Cano, J.D. Enhanced Full-Wave Circuit Analysis for Modeling of a Split Cylinder Resonator. *IEEE Trans. Microw. Theory Tech.* **2017**, *65*, doi:10.1109/TMTT.2016.2637932.

22. Krupka, J.; Gregory, A.P.; Rochard, O.C.; Clarke, R.N.; Riddle, B.; Baker-Jarvis, J. Uncertainty of complex permittivity measurements by split-post dielectric resonator technique. *J. Eur. Ceram. Soc.* **2001**, *21*, 2673–2676, doi:10.1016/S0955-2219(01)00343-0.

23. Hosseini, M.H.; Heidar, H.; Shams, M.H. Wideband Nondestructive Measurement of Complex Permittivity and Permeability Using Coupled Coaxial Probes. *IEEE Trans. Instrum. Meas.* **2017**, *66*, 148–157, doi:10.1109/TIM.2016.2619958.

24. Anlage, S.M.; Talanov, V. V; Schwartz, A.R. Principles of Near-Field Microwave Microscopy. In *Scanning Probe Microscopy: Electrical and Electromechanical Phenomena at the Nanoscale*; Kalinin, S., Gruverman, A., Eds.; Springer New York: New York, NY, 2007; pp. 215–253 ISBN 978-0-387-28668-6.

25. Kleismit, R. a; Kazimierczuk, M.K.; Kozlowski, G. Sensitivity and Resolution of Evanescent Microwave Microscope. *IEEE Trans. Microw. Theory Tech.* **2006**, *54*, 1–9.

26. Imtiaz, A.; Wallis, T.M.; Kabos, P. Near-Field Scanning Microwave Microscopy: An Emerging Research Tool for Nanoscale Metrology. *IEEE Microw. Mag.* **2014**, *15*, 52–64, doi:10.1109/MMM.2013.2288711.

27. Gao, C.; Xiang, X.D. Quantitative microwave near-field microscopy of dielectric properties. *Rev. Sci. Instrum.* **1998**, *69*, 3846–3851, doi:10.1063/1.1149189.

28. Tabib-Azar, M.; Zhang, T.; LeClair, S.R. Self-oscillating evanescent microwave probes for nondestructive evaluations of materials. *IEEE Trans. Instrum. Meas.* **2002**, *51*, 1126–1132, doi:10.1109/TIM.2002.807798.

29. Wu, B.Y.; Sheng, X.Q.; Fabregas, R.; Hao, Y. Full-wave modeling of broadband near field scanning microwave microscopy. *Sci. Rep.* **2017**, *7*, 1–10, doi:10.1038/s41598-017-13937-5.

30. Geaney, S.; Cox, D.; Hönigl-Decrinis, T.; Shaikhaidarov, R.; Kubatkin, S.E.; Lindström, T.; Danilov, A. V.; de Graaf, S.E. Near-Field Scanning Microwave Microscopy in the Single Photon Regime. *Sci. Rep.* **2019**, *9*, 1–7, doi:10.1038/s41598-019-48780-3.

31. Lee, J.; Long, C.J.; Yang, H.; Xiang, X.D.; Takeuchi, I. Atomic resolution imaging at 2.5 GHz using near-field microwave microscopy. *Appl. Phys. Lett.* **2010**, *97*, 10–13, doi:10.1063/1.3514243.

32. Analog Devices RF/IF Gain and Phase Detector AD8302 Available online: https://www.analog.com/media/cn/technical-documentation/evaluation-documentation/AD8302.pdf (accessed on Mar 5, 2021).

33. Gutierrez-Cano, J.D.; Plaza-Gonzalez, P.; Canos, A.J.; Garcia-Banos, B.; Catala-Civera, J.M.; Penaranda-Foix, F.L. A New Stand-Alone Microwave Instrument for Measuring the Complex Permittivity of Materials at Microwave Frequencies. *IEEE Trans. Instrum. Meas.* **2020**, *69*, doi:10.1109/TIM.2019.2941038.

34. Gregory, A.P.; Blackburn, J.F.; Lees, K.; Clarke, R.N.; Hodgetts, T.E.; Hanham, S.M.; Klein, N. Measurement of the permittivity and loss of high-loss materials using a Near-Field Scanning Microwave Microscope. *Ultramicroscopy* **2016**, *161*, 137–145, doi:10.1016/j.ultramic.2015.11.015.

35. Darko Kajfez *Q-Factor*; Vector Fields: Oxford, MS, USA, 1994;

36. Kajfez, D. Linear Fractional Curve Fitting for Measurement of High Q Factors. *IEEE Trans. Microw. Theory Tech.* **1994**, *42*, 1149–1153, doi:10.1109/22.299749.

37. Bethe, H.A.; Schwinger, J. *Perturbation Theory for Cavities*; NDRC: Cornell University, Rpt. D1-117, 1943;

38. Altschuler, H.M. Dielectric constant. In *Handbook of Microwave Measurements*; Sucher, M., Fox, J., Eds.; Polytech. Inst. Brooklyn Press: New York, NY, USA, 1963.

39. Khanna, S.K.; Ehrenfreund, E.; Garito, A.F.; Heeger, A.J. Microwave properties of high-purity tetrathiofulvalene-tetracyanoquinodimethan (TTF-TCNQ). *Phys. Rev. B* **1974**, *10*, 2205–2220, doi:10.1103/PhysRevB.10.2205.

40. Catalá-Civera, J.M.; Canós, A.J.; Plaza-González, P.; Gutiérrez, J.D.; García-Baños, B.; Peñaranda-Foix, F.L. Dynamic Measurement of Dielectric Properties of Materials at High Temperature during Microwave Heating in a Dual Mode Cylindrical Cavity. *IEEE Trans. Microw. Theory Tech.* **2015**, *63*, 2905–2914, doi:10.1109/TMTT.2015.2453263.

41. Roussy, G.; Thiebaut, J.M.; Ename-Obiang, F.; Marchai, E. Microwave broadband permittivity measurement with a multimode helical resonator for studying catalysts. *Meas. Sci. Technol.* **2001**, *12*, doi:10.1088/0957-0233/12/4/321.

42. Penaranda-Foix, F.L.; Janezic, M.D.; Catala-Civera, J.M.; Canos, A.J. Full-wave analysis of dielectric-loaded cylindrical waveguides and cavities using a new four-port ring network. *IEEE Trans. Microw. Theory Tech.* **2012**, *60*, 2730–2740, doi:10.1109/TMTT.2012.2206048.

43. Krupka, J. Precise measurements of the complex permittivity of dielectric materials at microwave frequencies. *Mater. Chem. Phys.* **2003**, *79*, 195–198, doi:10.1016/S0254-0584(02)00257-2.

44. Metaxas, A.C.; Driscoll, J.L. A Comparison of the Dielectric Properties of Paper and Board At Microwave and Radio Frequencies. *J. Microw. Power* **1974**, *9*, 79–89, doi:10.1080/00222739.1974.11688904.

45. Torgovnikov, G.I. Dielectric Properties of Wood-Based Materials. In *Dielectric*

Properties of Wood and Wood-Based Materials; Springer Berlin Heidelberg: Berlin, Heidelberg, 1993; pp. 135–159 ISBN 978-3-642-77453-9.

Chapter 5

High-Resolution Detection of Rock-Forming Minerals by Permittivity Measurements with a Near-Field Scanning Microwave Microscope

José D. Gutiérrez-Cano [1], José M. Catalá-Civera [1], Angel M. López-Buendía [2], Pedro J. Plaza-González [1], Felipe L. Peñaranda-Foix [1]

[1] Instituto ITACA. Universitat Politècnica de València. Camino de Vera s/n.46022 Valencia, Spain.

[2] CEINNMAT Innovaciones, INNCEINNMAT, SL, C/Catedrático Agustín Escardino, 9, 46980 Valencia, Spain

Sensors 2022, 22, 1138

Abstract

The identification of the minerals composing rocks and their dielectric characterization is essential for the utilization of microwave energy in the rock industry. This paper describes the use of a near-field scanning microwave microscope with enhanced sensitivity for non-invasive measurements of permittivity maps of rock specimens at the micrometer scale in non-contact mode. The microwave system comprises a near-field probe, an in-house single-port vectorial reflectometer, and all circuitry and software needed to make a stand-alone, portable instrument. The relationship between the resonance parameters of the near-field probe and the dielectric properties of materials was determined by a combination of classical cavity perturbation theory and an image charge model. The accuracy of this approach was validated by a comparison study with reference materials. The device was employed to determine the permittivity maps of a couple of igneous rock specimens with low-loss and high-loss minerals. The dielectric results were correlated with the minerals comprising the samples and compared with the dielectric results reported in the literature, with excellent agreements.

5.1 Introduction

Identifying the minerals that constitute rocks is a fundamental task in earth sciences, as well as in other engineering and industrial applications. Some techniques can only identify the type and amount of the minerals comprising the rock. However, many techniques can define the position of the heterogeneously distributed minerals within the structure. Particularly noteworthy are polarized light microscopy, X-ray diffraction (XRD), or X-ray fluorescence (XRF) [1–3]. The scientific literature reveals a large number of alternative techniques for this identification process, such as laser-induced breakdown spectroscopy (LIBS), scanning electron microscope supported with energy dispersed spectroscopy (SEM/EDS), or an electron probe microanalyzer (EPMA) [4–7]. In addition, other studies report techniques or algorithms, such as image treatment or neural networks, for the automatic identification of minerals, based on the information retrieved using some of the techniques mentioned above [8–13].

In recent years, there has been a growing interest regarding the utilization of microwave energy as a clean, green, and sustainable methodology for treating materials [14–16]. In the rock industry, microwave energy can contribute to developing more efficient, fast, and eco-friendly processes in various applications, such as fracture, cutting, comminution, leaching, or natural stone processing [17–22].

Complex permittivity describes the materials' behavior in the presence of an electromagnetic field; therefore, it is one of the most relevant parameters to study in a high-power microwave application process [23].

Dielectric characterization provides the absorption capabilities of the rocks and, hence, is directly related to the heating patterns. Likewise, permittivity data provides the needed information for the design of microwave applicators for a specific high-power application. Permittivity measurements can be classified in a large number of techniques [24–29], which can be categorized according to the measurable frequency range and the attributes of the materials to be characterized, such as dielectric losses, shape, or homogeneity [30]. Since rocks are heterogeneous materials, the approaches followed to measure their dielectric properties are very varied.

Some authors have measured the bulk dielectric properties of a certain unidentified volume of the complete rock specimen; hence, the permittivity obtained is a mixture of the permittivity of the different minerals comprising the rock. For instance, Lu et al. [31] measured the permittivity of basalt, gabbro, and granite rocks employing the coaxial transmission line technique, shaping the rocks in the shape of a tube (7 mm outer diameter, 3 mm inner diameter, and 10 mm length) to fill the coaxial airline. Deyab et al. [32] reported the dielectric properties of kimberlite and granite samples through the coaxial probe technique, which retrieves the permittivity of a considerable region surrounding the measurement tip. Similarly, Lovás et al. [33] determined the permittivity of several minerals, such as andesite or magnesite, by a resonance cavity method using rod samples (3 mm diameter and 12 mm length). In addition, some authors have developed methods to employ the bulk changes in dielectric properties (and thus in the resonant parameters) to identify physical changes in building materials [34,35].

On the other hand, some authors measured the permittivity of the homogeneous rock-forming and accessory minerals, in pure form, isolated from the rocks. For instance, Zheng et al. [36] employed a customized rectangular resonant cavity to determine the

dielectric properties of pulverized high-grade minerals, removing the air influence by means of the complex refractive index (CRI) equation. However, with this approach, as rocks are heterogeneous materials, rock-forming materials should be identified, located, isolated, and measured.

Other authors have studied the microwave-absorbing capabilities of rocks and minerals, running heating tests with domestic or industrial microwave systems and analyzing the material behavior over time [19,37]. Accordingly, there is a lack of permittivity measurement techniques that fit the requirements of heterogeneous rock specimens in the scientific literature. Near-field scanning microwave microscopes (NSMM) can fill this gap, as they can achieve permittivity maps of heterogeneous planar materials.

Near-field scanning microwave microscopes (NSMM) are measurement devices able to determine the electromagnetic response of materials on length scales far shorter than the wavelength of the emitted signal [38]. To accomplish near-field radiation, the size of the microwave probe (D) must be smaller than the probe-to-sample distance (r), and both parameters must be far shorter than the wavelength (λ) of the transmitted signal ($D \leq r << \lambda$), achieving spatial resolutions on the range of D. The fundamental element of an NSMM is the near-field microwave probe, which is frequently implemented by a sharp coaxial aperture [39,40]. Additionally, many scientific works explore alternative geometries for that purpose, such as spiral resonators or open-ended circular waveguides [41,42]. An NSMM also comprises a microwave emitter and receptor, usually a vector network analyzer (VNA), and a positioning system [43].

Microwave probes can be configured as resonant or non-resonant structures [38]. A resonant configuration increases sensitivity but decreases measurement bandwidth [44]. Non-resonant configurations relate the changes in the magnitude and phase of the reflection or transmission coefficients to the physical changes of materials. On the other hand, resonant setups employ the shifts in the resonant frequency and quality factor parameters to determine the physical properties of the materials. The relationship between the measurable quantities and the physical parameters can be addressed through several techniques, such as full-wave analysis or lumped-element circuit models [45,46]. The cavity perturbation technique has also been widely used, since the electromagnetic fields inside the sample are much smaller than the fields in the resonator. The theory developed by Gao and Xiang [47] is one of the most used approaches for quantitative microscopy of complex permittivity [40,48–50].

Nowadays, the trend of NSMM devices is moving towards achieving nanometric resolutions, which requires a precise distance-following technique usually performed by means of an additional nanoscale microscope technology, such as scanning tunneling microscopes (STM) or atomic force microscopes (AFM) [51–53]. NSMMs have been used in a broad range of applications, such as dielectric microscopy of substrates, defects identification, or even biological cells imaging [54–56]. Monti et al. [57] already employed a contact-mode NSMM device with sub-micrometric resolution to elucidate the underlying physical processes that control the microwave heating of rocks at a fundamental level of some micrometric hematite inclusions in a gangue matrix (around 10 μm x 10 μm size).

In a previous work [58], we demonstrate the benefits of the NSMM technology at the micrometer scale to identify markers on anti-counterfeiting applications. Similarly, the development of an NSMM device able to determine permittivity maps at the

submicrometric scale without contact between the sample and the probe would improve the applicability of this technology in the rock industry for predicting the heating patterns of samples to be processed under microwave irradiation. Additionally, this device would be interesting to use as an automated system to reduce times in other industrial applications, such as drill core logging, widely used for geological exploration in mining or geotechnics, for lithology, mineral identification, or structures identification [59–61].

In this work, we describe the use of near-field microwave microscopy in obtaining contactless complex permittivity scans of rocks at a sub-millimeter scale. For that purpose, the microscope probe reported in [39] was replaced with a larger probe with a redesigned tip, increasing the sensitivity of the near-field probe for loss factor measurements to fit the specific requirements of this application. The methodology to calculate permittivity values from resonant measurements reported in our previous work was also improved by a combination of classical cavity perturbation theory and an image charge model. The NSMM sensor was employed to determine the permittivity maps of some representative specimens of ornamental rocks and compare the permittivity results with those reported in previous works.

5.2 Materials and Methods

5.2.1 The Near-Field Microwave Microscope

The sensing experiments were carried out in a near-field microwave microscope similar to the system reported in [58] with specific modifications to measure rocks.

Fig. **1** illustrates a schematic diagram of the different parts that constitute the instrument (near-field microwave probe, microwave source and detector, and positioning subsystem) with a zoomed image of the upgraded sensor probe.

The measurement probe consisted of a capacitively fed resonant coaxial cavity with an inner conductor, enlarged and tapered to meet the requirements for near-field radiation ($D \leq r << \lambda$). The response of the probe around the resonance peak S_{11} contains all the information required to determine the permittivity of the material.

In this work, the dimensions of the measurement probe were larger than those in our previous design to increase the sensitivity of the quality factor response and thus the resolution in the loss factor measurements. The size of the resonant coaxial line corresponds to the size of a commercial RG402 line, with a sharp tip of ~50 µm radius. The length of the coaxial line was 53.5 mm to achieve an air resonance frequency close to 2 GHz. Since the study's main objective is to predict the heating patterns of samples to be processed with high-power microwave energy, we employed a resonant frequency value between 915 MHz and 2.45 GHz, the most common frequencies to process materials under high-power microwave irradiation [62].

The microwave source and detector were based on an in-house, single-port vectorial reflectometer design, described in [30] (see Fig. **2**). The microwave source is a frequency synthesizer based on a phase-locked loop (PLL), comprising an external filter,

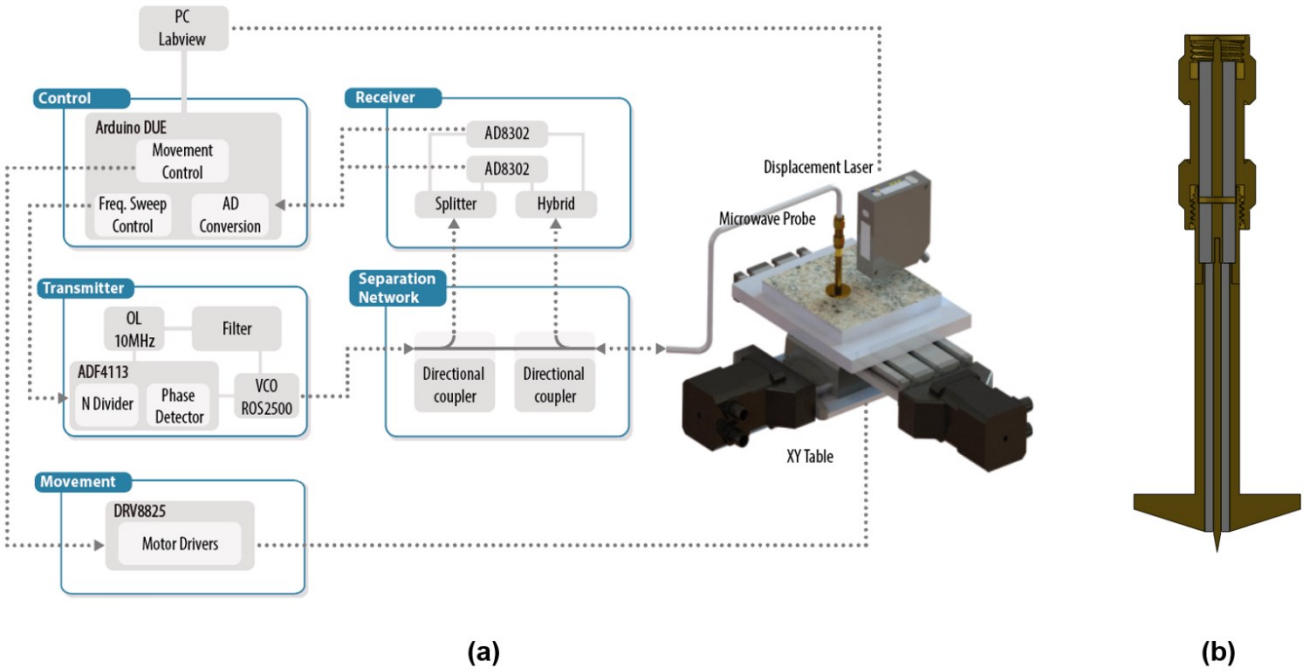

Fig. **1**: Schematic diagram of the near-field microwave microscope: (a) schematic diagram of the in-house vector network analyzer for measuring the reflection (S_{11}) of the near-field microwave microscope; (b) cross-section of the near-field coaxial resonator.

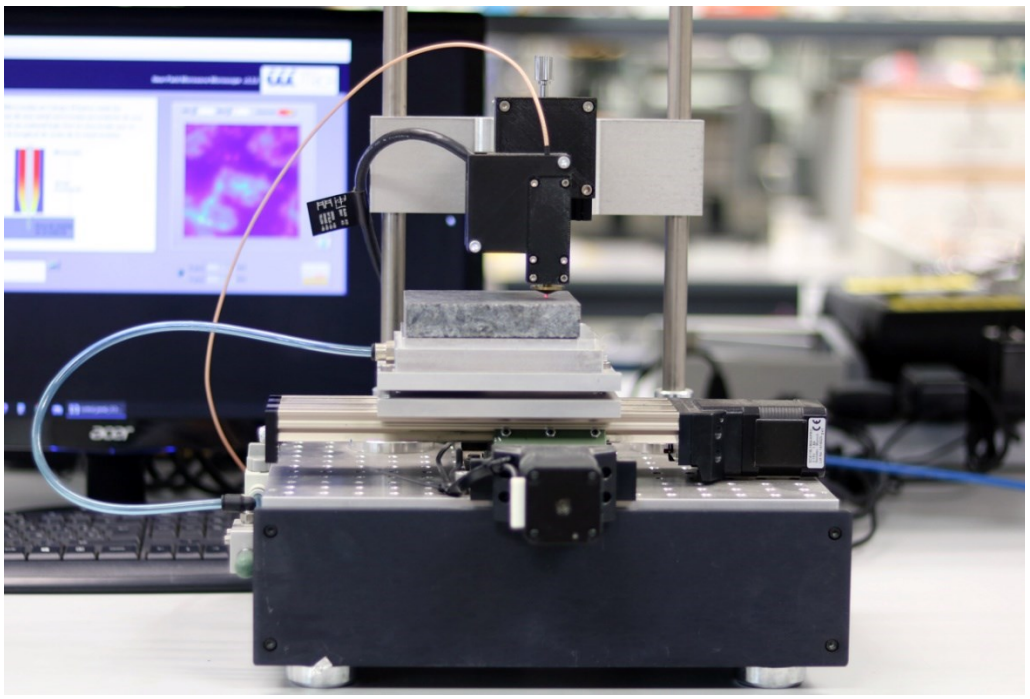

Fig. **2**: The near-field microwave microscope system.

a local oscillator (OL), a voltage-controlled oscillator (ROS-2500, Mini-Circuits, Brooklyn, NY, USA), and an ADF4113 (Analog Devices, Norwood, MA, USA), which includes the divider and the phase detector. The reflection parameter or S_{11} is calculated at the receiver by comparing the PLL's incident signal with the signal reflected at the probe. In this regard, a separation network, comprising two bi-directional couplers (BDCA 1-7-33 +, Mini-Circuits), was employed previously to collect a small amount of those incidents and reflected signals. The receiver was based on the AD8302 RF/IF Gain and Phase Detector (Analog Devices). Since the phase response of this integrated circuit is similar for positive or negative phase differences, two AD8302 units were needed to solve the phase ambiguity (see [30] for further information).

The positioning subsystem comprised an XY-stage (KT-70, proxxon) with a vacuum table attached, driven by two stepper motors and drivers (DRV8825, Texas Instruments, Dallas, TX, USA). The probe was attached in a fixed position over the XY-stage, manually positioned by a micrometric screw. In addition, a displacement laser (HL-G103-SJ, Panasonic, Osaka, Japan) was utilized to precisely determine the tip-to-sample distance. An Arduino board, together with a Labview piece of software running in a computer, control all the elements of the microscope: generating the incident signal, receiving the reflected signal, calculating the reflection coefficient and the resonant parameters, calculating the dielectric properties, plotting the results, moving the XY-stage, and synchronizing the movements with the measurements. Fig. **2** depicts the stand-alone NSMM system.

The single-port vectorial reflectometer was allowed to stabilize for one hour before measurements. Subsequently, a standard OSM calibration procedure was carried out from 1930 to 1970 MHz employing the 85052 B Standard Mechanical Calibration Kit (3.5 mm, Keysight Technologies, Santa Rosa, CA, USA).

5.2.2 Dielectric Characterization

As described in Section 5.2.1, the near-field sensor was configured as a resonator; thus, the permittivity is related to the resonance frequency (fr) and the quality factor (Q) of the microwave structure. The fr and unloaded Q values were calculated from the reflection coefficient measurements through the linear, fractional curve-fitting procedure reported by Kajfez [63,64].

Fig. **3** shows the response of the near-field resonant probe (f_r and Q) for a set of rod-shaped materials as a function of the tip-to-sample distance (g). These materials were selected to cover a wide range of both dielectric constant (ε') and loss factor (ε'') values, with a sample size sufficient to be considered as infinite dielectric materials (15 mm height, 9.8 mm diameter) [40,65]. The f_r curves exhibited similar trends to those shown by the smaller probe reported in our previous work [58]. Nevertheless, the Q sensitivity increased substantially due to the improvements.

The operating range of the probe was centered between 50 µm and 250 µm, seeking a balance between the probe's sensitivity and the robustness against uncertainties in the determination of g. Below 50 µm, the sensitivity of the probe would increase remarkably, but the uncertainties in the determination of g would lead to significant uncertainties in the retrieved permittivity results. In addition, the minor imperfections in the surface of the

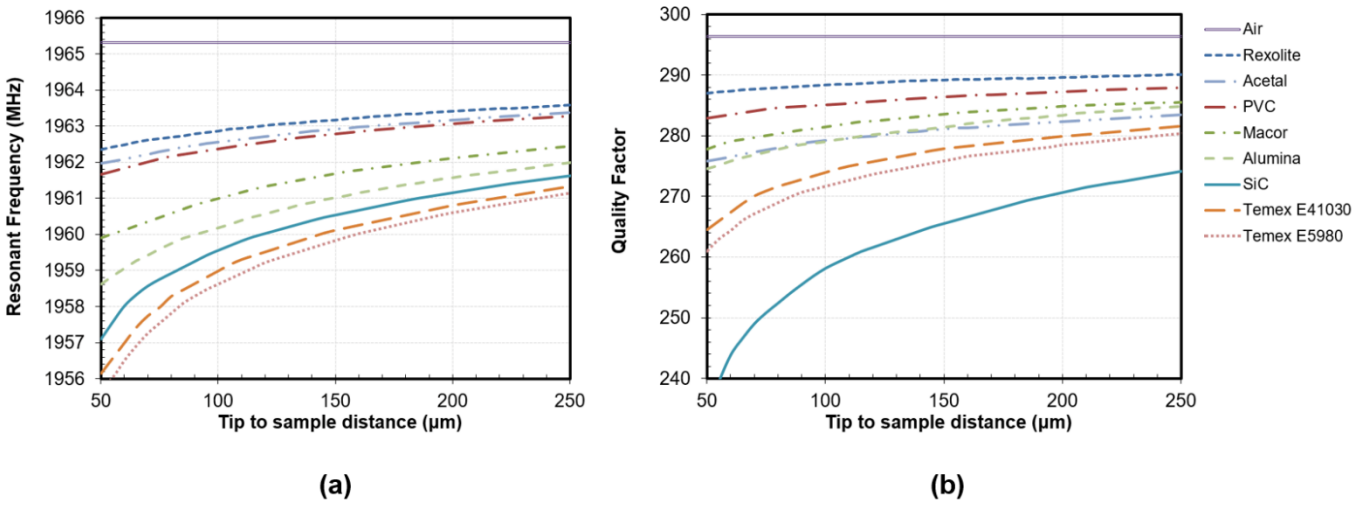

Fig. **3**: Response of the sensor as a function of the tip-to-sample distance for different reference materials: (a) resonant frequency; (b) unloaded quality factor.

materials and the non-horizontality of the base could cause the probe tip to touch the material and be damaged. Above 250 μm, the probe's response would be more robust against errors in the determination of g, but the sensitivity of both f_r and Q parameters would decrease.

All microwave scans were performed at a central g of 150 μm. Nonetheless, the permittivity model should include the influence of the tip-to-sample distance to account for possible variations of this parameter during the scan because of irregularities in the height of the material and uneven horizontality of the material surface when placed over the microscope's base. At 150 μm, the maximum f_r shift, presented between air (ε'= 1) and Temex E5980 (ε' = 67.39), was around 6 MHz. The response of the probe compresses as the dielectric constant of the MUT increases; thus, the f_r shift between air (ε'= 1) and Rexolite (ε'= 2.57) is similar to the shift observed between Rexolite and Macor (ε'= 5.68), and higher than the deviation exhibited between alumina (ε'= 9) and Temex E5980 (ε' = 67.39). Regarding the behavior of the quality factor, the maximum deviation, observed between air (ε'' = 0) and SiC (ε'' = 2.07), was around 30. However, it is noteworthy that, for a given g, the Q of materials with similar loss levels decreases as ε' increases (f_r decreases). Thus, Rexolite (ε'' = 0.0008, $tan\ \delta$ = 3 × 10−4) and Temex 41030 (ε'' = 0.0007, $tan\ \delta$ = 2·10−5), materials with similar dielectric losses, have considerably divergent Qs, 289.17 and 277.85, respectively: for a given loss factor, the resonance widens with increasing dielectric constant.

In our previous work [58], the determination of the dielectric properties was addressed using the microwave cavity perturbation technique (MCPT). In the near-field zone, with evanescent waves, the field distribution can be considered as a static problem where phase and retardation need not be considered [50]. Then, assuming a quasi-static electric field inside the MUT [66], we employed Khanna et al. [67] to relate the shifts in f_r and Q with permittivity. For convenience, we reproduce the below formulas:

$$\varepsilon' = 1 + \frac{-\frac{\Delta f}{f}\left(\eta + N\frac{\Delta f}{f}\right) - N\left[\Delta\left(\frac{1}{2Q}\right)\right]^2}{\left(\eta + N\frac{\Delta f}{f}\right)^2 + N^2\left[\Delta\left(\frac{1}{2Q}\right)\right]^2} \quad (1)$$

$$\varepsilon'' = \frac{\eta\Delta\left(\frac{1}{2Q}\right)}{\left(\eta + N\frac{\Delta f}{f}\right)^2 + N^2\left[\Delta\left(\frac{1}{2Q}\right)\right]^2} \quad (2)$$

$$\frac{\Delta f}{f} = \frac{f_s - f_0}{f_s} \quad (3)$$

$$\Delta\left(\frac{1}{2Q}\right) = \frac{f_0}{f_s}\cdot\frac{1}{2}\cdot\left(\frac{1}{Q_s} - \frac{1}{Q_0}\cdot\frac{f_s^2}{f_0^2}\right) \quad (4)$$

where ε' = dielectric constant (dimensionless); ε'' = loss factor (dimensionless); η = sample-filling factor (dimensionless); N = sample-depolarization factor (dimensionless); f_0 = resonant frequency (Hz) of the open-air cavity; f_s = resonant frequency (Hz) with a dielectric material near the tip; Q_0 = quality factor (dimensionless) of the open-air cavity; Q_s = quality factor (dimensionless) with a dielectric material near the tip.

However, this model did not conform precisely to the response measured with the higher size probe employed in this work, mainly due to the aforementioned widening of the resonance with the increase in the dielectric constant. However, it is well known from the literature that the determination of the dielectric constant in NSMM measurement systems is independent of the Q changes (see Equations (5) and (6)). Hence, the parameters η and N needed to determine the dielectric constant values from the f_r measurement as a function of g can be obtained by removing Q's influence ($Q_s = Q_0$) on Equation (1) (see Figure **4**). To obtain these curves, three materials were employed: air, Macor ($\varepsilon' = 5.68$), and Temex E41030 ($\varepsilon' = 28.28$). However, this model (Equation (2)) did not accurately reproduce all the dielectric losses of the analyzed materials.

Considering quasi-static fields, Gao and Xiang [47] developed a model for the case of a conducting spherical tip radiating over a dielectric material employing an image charge model and the MCPT. The relationship between the dielectric constant and the f_r shift for the case of soft contact ($g = 0$) was determined as follows:

$$\frac{\Delta f}{f_0} = -A\left(\frac{\ln(1-b)}{b} + 1\right) \quad (5)$$

where $b = (\varepsilon' - 1)/(\varepsilon' + 1)$, and A is a constant to be minimized, related to the geometry of the near-field probe. For our specific case, where there is an air gap between the dielectric sample and the probe's tip ($g > 0$), the equations became an iterative problem, as follows:

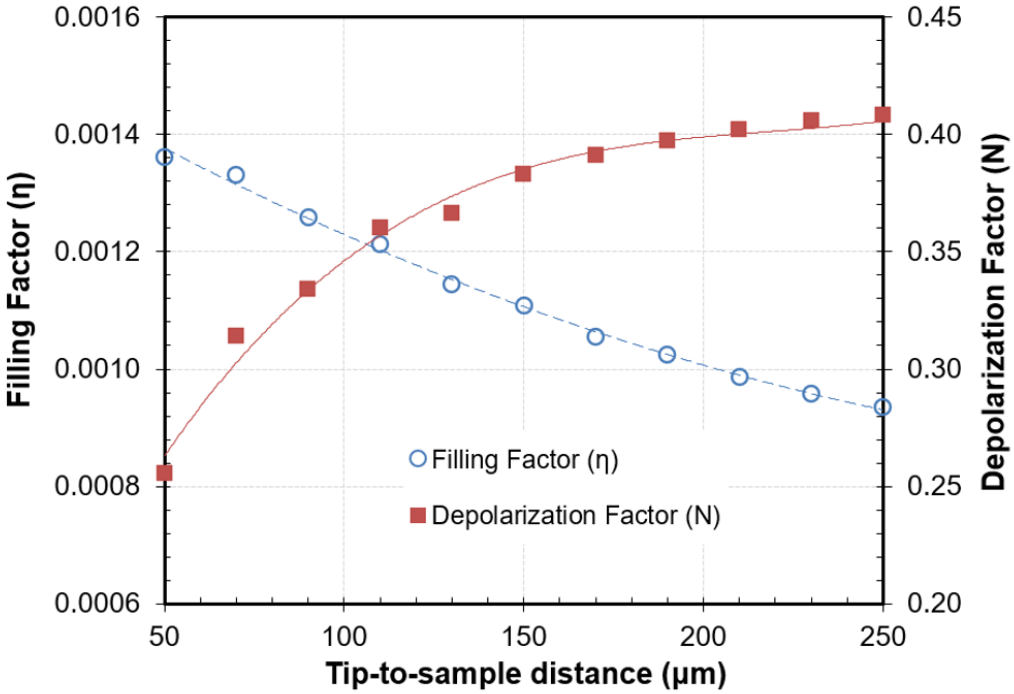

Fig. **4**: Calibration parameters, η and N, of the cavity perturbation method determined with reference samples as a function of the tip-to-sample distance.

$$\frac{\Delta f_s}{f_s} = -A\sum_{n=1}^{\infty}\frac{bt_n}{a_1' + a_n'} \tag{6}$$

$$a_n' = 1 + a' + \frac{1}{1 + a' + a_{n-1}'},\ t_n = \frac{b}{1 + a' + a_{n-1}'}t_{n-1} \tag{7}$$

where $\Delta f_s = f_s - f_0$. The initial conditions were as follows: $a' = g/R_0$, being g the tip-to-sample distance and R_0 the tip radius; $a_1' = 1 + a'$; and $t_1 = 1$. For both configurations, the dielectric losses were determined to be related to the f_r and Q shifts, as follows:

$$\Delta\left(\frac{1}{Q}\right) = \frac{1}{Q_s} - \frac{1}{Q_0} = -(B + \tan\delta)\frac{\Delta f_s}{f_s} \tag{8}$$

B is a constant to be minimized and $tan\delta = \varepsilon''/\varepsilon'$. Over the years, some scientific works have tried to improve the accuracy of this model, especially concerning dielectric losses, adding new constants or quadratic terms to Equation (8) [48–50]. Finally, Gregory et al. [40] reported the use of Equation (6) with the complex resonant frequency (f_s^* in Equation (9)) to avoid the use of Equation (8).

$$f_S^* = f_S\left(1 + \frac{j}{2Q}\right) \tag{9}$$

The increase in the size of the probe and the geometry of this tip has allowed the use of Equation (6) with the complex resonance parameter (Equation (9)) to model the response of this new probe with the improved sensitivity of *Q*. However, the parameters minimized showed certain dependence with frequency or dielectric constant, as reported in previous works [48,49] for the parameters determined in the dielectric loss equation. Figure **5** shows the dependence of *A* with the logarithm of the dielectric constant of some reference materials (Rexolite, Acetal, PVC, Alumina, SiC, and Temex E5980). This result would preclude the use of this method to calculate the complex permittivity from the relative shifts of f_r and *Q* in our case, since it would require prior knowledge of the dielectric constant value of the measured material. To overcome this limitation, Equation (1) (with $Q_s = Q_0$) was employed with the parameters interpolated in Fig. **4** to determine the dielectric constant values. This value was employed to determine *A* from Figure **5**, and the loss factor values were calculated using Equation (6) with the complex resonant frequency concept (Equation (9)).

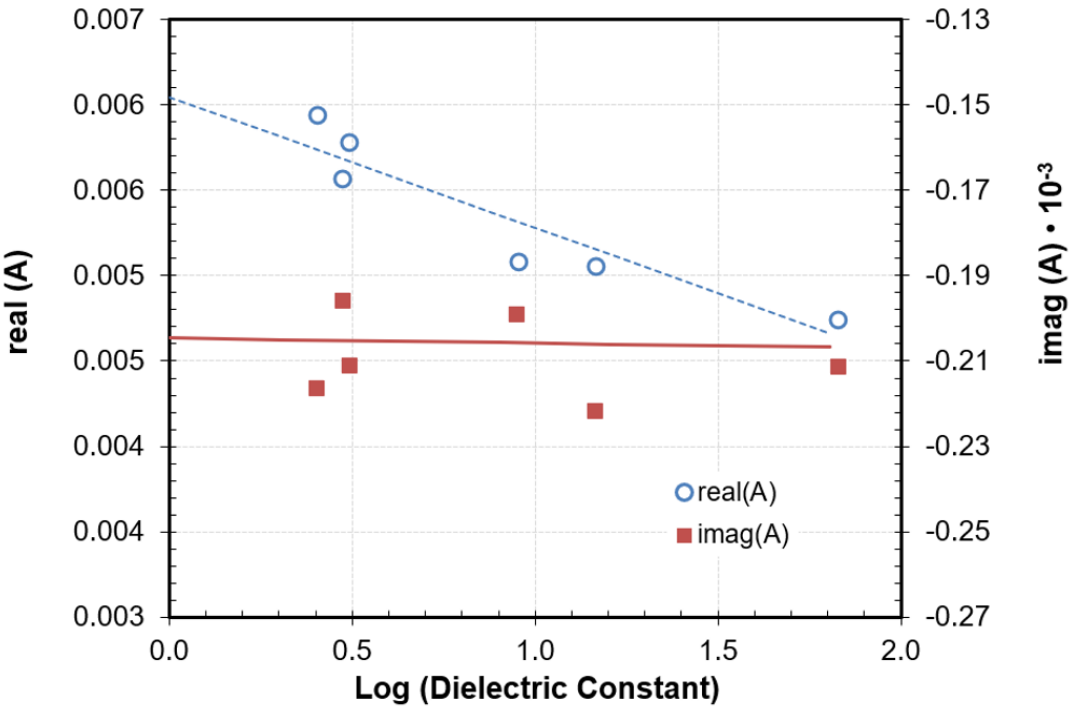

Fig. **5**: Calibration parameter A of the image charge model determined with reference samples as a function of the dielectric constant.

5.2.3 Rock Samples

Two rock specimens were selected to test the proposed microscopy technique. The selected rocks, representing felsic and mafic families, are used widely in ornamental material construction as natural stones.

Rocks pieces were cut in sections of 10 × 10 × 2 cm with the surface polished to improve the readability of the system. The mineral composition of the rock specimens depicted in

Fig. **6** was determined by petrographic polarized light microscopy, chemical microanalysis EDX in a scanning electron microscope (SEM), and X-ray analysis of the bulk sample and the magnetic fraction. Table I summarizes the dielectric properties references of the rock-forming minerals found in this analysis.

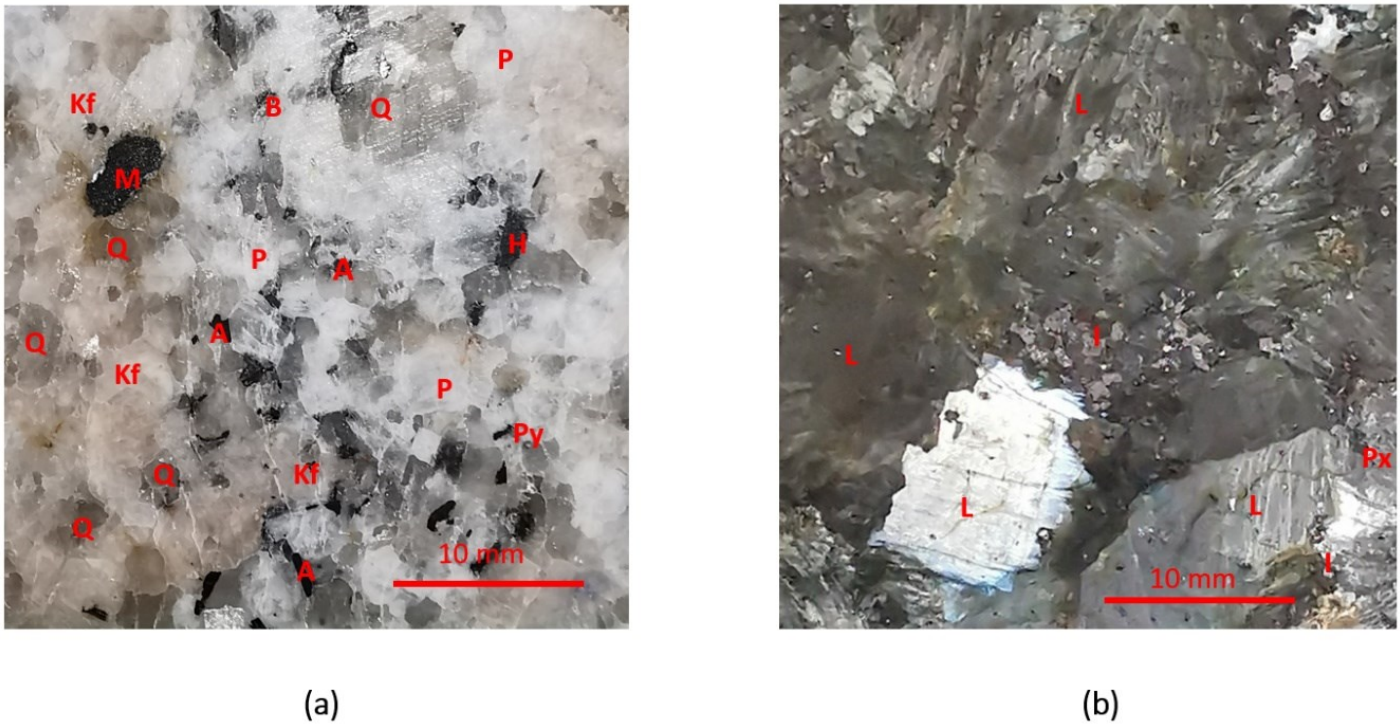

Fig. **6**: Microscope images of two types of rock: (a) gneiss (Q—quartz; Kf—potassium feldspar; P—plagioclase; B—biotite; A—aegirine-augite pyroxene; H—hornblende; M—magnetite; Py—pyrite); and (b) anorthosite (L—labradorite plagioclase; Px—pyroxene; I—ilmenite)

Table I. Dielectric property results of reference materials and associated standard deviations.

Material	Frequency (GHz)	Permittivity	Reference
k-Feldspars	2.00	5.18-j0.023	[68]
	9.37	5.12-j0.011	[69]
	9.37	4.75-j0.044	[69]
Biotite	1.00	5.9-j0.002	[70]
Plagioclase (Labradorite)	2.45	6.01-j0.09	[71]
Plagioclase	2.45	3.49-j0.020	[37]
Plagioclase (albite)	2.45	5.62-j0.039	[36]
Pyroxene (augite)	2.45	6.80-j0.182	[36]
Hornblende	2.45	14.45-j0.324	[36]
	2.45	8.91-j0.233	[37]
	2.45	7.37-j0.026	[71]
Magnetite	2.45	14.5-j2.5	[72]
Pyrite (Shanxi Lu'an)	2.45	8-j0.75	[73]
Ilmenite	2.45	3.75-j0.24	[72]
	2.45	23.6-j11.2	[71]

The felsic rock selected was a high-grade granitic gneiss. The analysis of the rock identified quartz, potassium feldspar (microcline), and alkaline plagioclase as major components, pyroxene (aegirine-augite) and biotite as secondary, and associate minerals represented by amphibole (hornblende), tourmaline, and opaque minerals. These opaque minerals were mainly magnetite (Fe_3O_4) (that appeared in aggregates with apparent inter-crystalline porosity and occasionally pyrrhotite (S_xFe_{1-x})-associated) and dispersed pyrite (FeS_2).

The mafic rock selected was anorthosite, a peralkaline gabbro with blueish and greenish-grey color. The rock was composed massively by macroscopic Na–Ca plagioclase of labradorite type domain and minor content of pyroxene and biotite. In addition, the rock was composed by a significant amount of oxide ores, mainly ilmenite ($FeTiO_3$) with some magnetite (Fe_3O_4) associated.

5.3 Experimental Results and Discussion

5.3.1 Dielectric Measurements of Reference Materials

The complex permittivity of the reference samples, employed to determine the response of Figure **3**, were measured to verify the accuracy of the procedure described in Section 5.2.2. Each dielectric sample was positioned on the microscope base centered in the axis of the near-field probe. From the point of soft contact, the Z-axis was moved upwards to three different tip-to-sample distances (100 µm, 150 µm, and 200 µm), measuring the reflection parameter employing the reflectometer and determining the resonance parameters, fr and Q. The parameters *N* and *η* corresponding to each *g* were determined to calculate the dielectric constant of the measurements. With the results obtained, the appropriate *A* parameter was interpolated to obtain the loss factor. All measurements were retrieved at a room temperature of 23 °C (see Table II).

Table II. Dielectric property results of reference materials and associated standard deviations.

Material	Dielectric Constant							Loss Factor						
	g (µm)			Mean	Std Dev	Reference	Error (%)	g (µm)			Mean	Std Dev	Reference	Error (%)
	100	150	200					100	150	200				
Air	1.00	1.00	1.00	1.00	0.00	1.00	0.00	0.000	0.000	0.000	0.000	0.000	0.000	0.00
Rexolite	2.55	2.57	2.57	2.56	0.01	2.53 ± 0.05	1.23	0.000	0.002	0.007	0.003	0.003	0.001 ± 0.000	>10
Acetal	2.88	2.90	2.92	2.90	0.02	2.96 ± 0.05	2.06	0.105	0.113	0.123	0.114	0.009	0.120. ± 0.006	5.65
PVC	3.09	3.07	3.12	3.09	0.03	3.09 ± 0.06	0.11	0.024	0.027	0.031	0.027	0.004	0.025 ± 0.001	9.75
Macor	5.69	5.63	5.66	5.66	0.03	5.68 ± 0.11	0.35	0.020	0.026	0.031	0.026	0.005	0.024 ± 0.001	7.44
Alumina	8.97	9.10	8.93	9.00	0.09	8.94 ± 0.18	0.68	0.012	0.025	0.020	0.019	0.006	0.006 ± 0.000	>10
SiC	14.53	14.74	14.69	14.66	0.11	14.53 ± 0.41	2.20	2.134	2.077	2.128	2.113	0.031	2.092 ± 0.105	1.09
Temex E41030	29.19	28.32	29.56	29.02	0.64	28.28 ± 0.56	2.63	0.068	0.000	0.130	0.066	0.065	0.001 ± 0.000	>10
Temex E5980	69.88	72.19	65.79	69.28	3.24	67.25 ± 1.34	3.02	0.000	0.000	1.014	0.338	0.585	0.018 ± 0.006	>10

To assess the accuracy of the results, the permittivity of the reference materials was also measured in a closed TM_{010} cylindrical cavity (98 mm diameter, 20 mm height) analyzed by the mode-matching technique described in [74]. The error (measurement bias), also reported in Table II, provides a complete image of the device's performance and

corresponds to the absolute difference between the measured mean value and the reference value. The reported standard deviation values provide information mainly related to the uncertainties in the height positioning and the stability of the electronics.

The determination of the dielectric constant revealed an excellent accuracy, with errors constrained below 3%, in comparison with the reference values.

The standard deviation values also exhibited little variability as a function of the tip-to-sample distance. However, the error increased slightly with the dielectric constant increment due to the compression in the resonant frequency response discussed in Section 5.2.2.

From the discrepancies observed in the results concerning the reference values, the accuracy of the loss factor measurement was below 10% within the range from 10^{-2} to 10^{1}, a noticeable result considering the large tip-to-sample distances employed in this work. Below 10^{-2}, even though the percentage errors were above 10%, the system is valid to determine whether it is a low-loss or a high-loss material. The standard deviation of the loss factor values revealed low figures with g variations for most materials. However, the compression effect of Q shifts was noticeable for high dielectric constant materials. For instance, the loss factor results calculated for Temex 5980 revealed fluctuations between 10^{-3} and 10^{0}. Nevertheless, it is important to highlight that the common use of the loss tangent definition ($\varepsilon''/\varepsilon'$) would mitigate this issue.

5.3.2 Permittivity Maps of Rock Specimens

The rock specimens were placed on the base of the microscope and fixed with the aid of the suction vacuum table. The tip-to-sample distance was set to 150 µm by means of the displacement laser and the Z-axis stage. Microwave scans explored a surface area of 33 mm × 33 mm with a spatial step of 100 µm. For each point of the surface scan, the dielectric properties were calculated from the information collected from the microwave reflectometer and the displacement laser, using the approach described in Section 5.2.2. All measurements were performed at a room temperature of 23 °C.

5.3.2.1 Gneiss

Fig. **7** shows the dielectric mark of the gneiss rock specimen. The dielectric pattern of both dielectric constant and loss factor results was very similar, agreeing with the mineral classification reported in [36]. Fig. **7**a shows a large area with moderate dielectric constant values ranging between 4 and 6 and a specific area in the left top corner, in which the values were above 10. Concerning the loss factor response, Fig. **7**b shows that most rock areas had low loss factor values and, therefore, had a reduced ability to absorb electromagnetic energy. However, other small regions disseminated throughout the specimen did exhibit moderate or high loss factor values.

From the petrographic analysis shown in Fig. **6**a, it was possible to correlate the rock's mineral composition with the measured permittivity. First, we found a large quantity of quartz mineral, a material commonly employed as a microwave inert element for microwave processing applications [75]. In these areas, the dielectric constant was around 4 with loss factor values below 10^{-2}, which indicated the low capacity of quartz

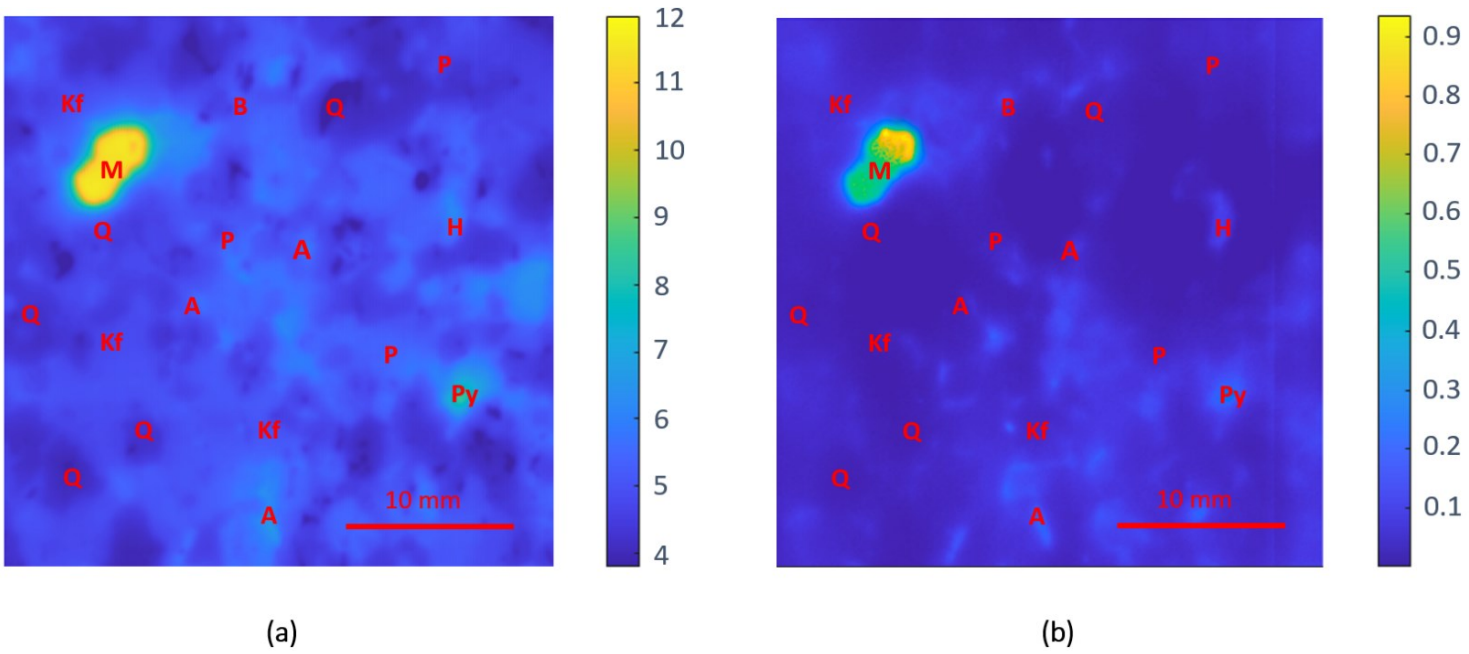

Fig. **7**: Microscope images of two types of rock: (a) gneiss (Q—quartz; Kf—potassium feldspar; P—plagioclase; B—biotite; A—aegirine-augite pyroxene; H—hornblende; M—magnetite; Py—pyrite); and (b) anorthosite (L—labradorite plagioclase; Px—pyroxene; I—ilmenite)

to absorb microwave energy as exhibited in the heating experiments reported in [76] and in other related reports [70]. The petrographic analysis also determined a significant presence of K-feldspars (microcline). In these areas, the permittivity obtained was between 4 and 5 for the real part and in the range of 10^{-2} for the imaginary part, with the results agreeing well with those reported in [68,69].

Sorting the materials by their permittivity results, the area with dielectric constant values between 5 and 6 and loss factor in the range from 10^{-2} to 0.1 corresponds to the biotite and plagioclase content. These results agree closely with those obtained in [70,71] and differ from those reported in [37]. Following, we found the pyroxene aegirine-augite and hornblende content, with dielectric constant results ranging from 6 to 7 and dielectric losses between 0.1 and 0.2. These results agree well with the permittivity reported of augite pyroxene in [36]. Again, the data reported in the literature provides dissimilar results for hornblende, with dielectric constant values ranging from 7 to 14.45 and loss factor values ranging from 0.02 to 0.32 [36,37,71]. Nevertheless, the dielectric loss of pyroxene and hornblende appears to be higher than those of the surrounding materials (quartz, feldspar, biotite, or plagioclase) since the content of this mineral is easily distinguished in the loss factor map. However, regarding the dielectric constant, the calculated values were lower than those in the literature, probably due to the penetration capabilities of electromagnetic waves at microwave frequencies [58] and the small size of the crystals of these minerals in this rock specimen observed in the petrographic analysis of the sample.

Finally, we can find the oxide ores magnetite and pyrite. The complex permittivity calculated for the aggregated magnetite content, located in the left top corner, was close to 12-j1. This value was very similar to the results reported in [72] at 2.45 GHz. The loss

factor results showed certain variability within this aggregate, maybe due to the apparent inter-crystalline porosity observed during the petrographic analysis. The permittivity determined for the pyrite content (8-j0.3) was slightly lower to the values described in [73], presumably due to the small size of the grains dispersed through the sample.

5.3.2.2 Anorthosite

Fig. **8** shows the dielectric mark of the anorthosite rock specimen. The dielectric pattern of both the dielectric constant and the loss factor responses was similar to that which happened in the rock analysis described in Section 5.3.2.1. Figure **8**a presents an area with moderate values of dielectric constant in the range of 6, which correspond to the zone of moderate–low losses in the range of 0.1, shown in Figure **8**b. The rest of the rock was composed of minerals with high permittivity, both in dielectric constant and loss factor.

The area with moderate permittivity values corresponds mainly to the Na–Ca plagioclase of labradorite composition. The dielectric constant determined for this mineral is around 6-j0.1, which is in complete agreement with that reported in [71]. The dielectric response of the small quantities of pyroxene exhibited a permittivity slightly higher than that of the labradorite plagioclase, as reported in [36].

The area with high permittivity values corresponds to the ilmenite metal oxide. Previous

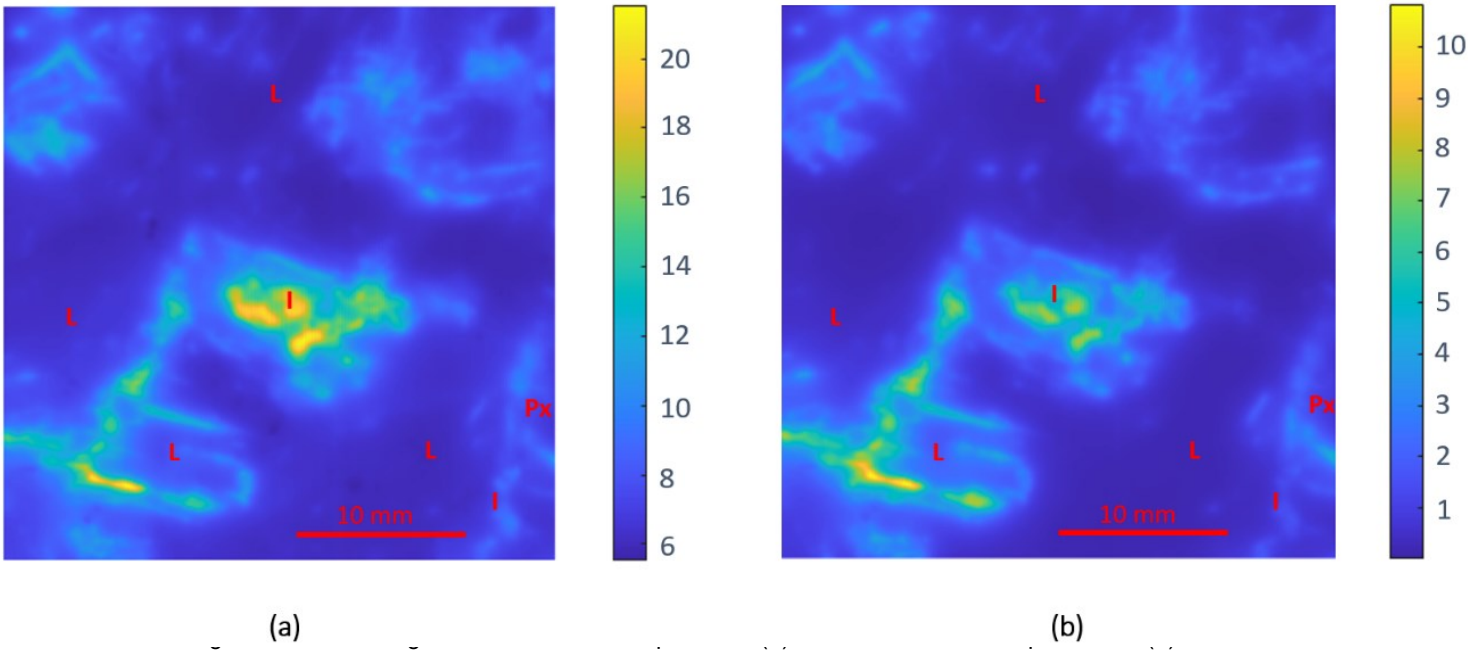

results (L—labradorite plagioclase; Px—pyroxene; I—ilmenite).

studies in the literature reported permittivity values of this mineral with significant variability. For instance, at 2.45 GHz permittivity of ilmenite was reported to be 3.75-j0.24 in [72] and 23.6-j11.2 in [71]. Apart from the significant differences found, most of the works agree that this metal oxide have high permittivity in both the real and imaginary parts. With these permittivity values, the processing of this area with microwave energy would be excellent: the high dielectric constant values would focus the electromagnetic field in these zones of the rock, and the dielectric losses would allow microwave heating.

Indeed, there is some variability in the permittivity values of the minerals analyzed, both in our work and in those reported by other authors, probably due to the diverse composition of the minerals and their purity, the texture of the measured material (micro- or macro-crystals, powder) [71,77], the influence of the surrounding components, or the uncertainties of the different methods [36]. Nevertheless, our system has been shown to agree well with the results reported in most of the previously published studies, thus validating the applicability of the non-contact near-field microwave microscope developed for the dielectric characterization of rocks, as well as for identifying and spotting the minerals that compose them.

5.4 Conclusions

In this work, we describe the use of a near-field scanning microwave microscope as a new device for the non-contact dielectric characterization of rock specimens at the micrometer scale.

The measurement instrument includes an in-house microwave reflectometer to allow autonomous performance and additional hardware and software elements to make the measurement procedure simple and straightforward.

To allow contactless loss factor measurements, we developed a near-field sensor with enhanced quality factor sensitivity and, thus, increased loss factor resolution. The response of this near-field microwave cavity as a function of the tip-to-sample distance was modeled through a combination of the classical MCPT with an image charge theory. A comparative measurement campaign of dielectric materials with other well-established instruments was carried out to validate the proposed measurement technique. The dielectric constant accuracy was within the range of 3%, and the error in the loss factor was constrained below 10% within the range 10^{-2} to 10^{1}, a remarkable result for the high tip-to-sample distances employed in the measurements.

Two types of rock with felsic and mafic compositions were selected to be analyzed with the developed sensor. Dielectric maps showed that the gneiss sample had low absorption capabilities, except in specific points disseminated throughout the rock. On the other hand, the permittivity response of the anorthosite specimen depicted moderate and high dielectric losses, and hence, presents excellent capabilities to be processed under microwave irradiation. The results obtained were found to agree well with the results reported in the literature, thus validating the performance of the proposed non-contact near-field microwave microscope.

This method will allow the identification of minerals and their dielectric characterization in the actual state in which they are found in the rock under study. In addition, the developed NSMM with enhanced sensitivity could also be employed as a stand-alone

tool to determine permittivity maps of planar materials at microwave frequencies in a broad range of sensing applications.

5.5 Funding

This paper has been financially supported through the grant reference BES-2016-077296 of the call Convocatoria de las ayudas para contratos predoctorales para la formación de doctores de 2016 by Ministerio de Economía y Competitividad (MINECO) and by European Social Funds (ESF) of European Union, and the project SEDMICRON—TEC2015-70272-R (MINECO/FEDER) supported by Ministerio de Economía y Competitividad (MINECO) and by European Regional Development Funds (ERDF) of European Union.

5.6 References

1. Susilowati, Y.; Rahyuwibowo, H.; Mengko, T.R. Characteristic of interference color in rock forming mineral images. *IEEE Asia-Pacific Conf. Circuits Syst. Proceedings, APCCAS* **2002**, *2*, 265–268, doi:10.1109/APCCAS.2002.1115223.
2. Povarov, V.G.; Kopylova, T.N.; Sinyakova, M.A.; Rudko, V.A. Quantitative Determination of Trace Heavy Metals and Selected Rock-Forming Elements in Porous Carbon Materials by the X-ray Fluorescence Method. *ACS Omega* **2021**, *6*, 24595–24601, doi:10.1021/acsomega.1c03217.
3. Zhou, X.; Liu, D.; Bu, H.; Deng, L.; Liu, H.; Yuan, P.; Du, P.; Song, H. XRD-based quantitative analysis of clay minerals using reference intensity ratios, mineral intensity factors, Rietveld, and full pattern summation methods: A critical review. *Solid Earth Sci.* **2018**, *3*, 16–29, doi:10.1016/j.sesci.2017.12.002.
4. Senesi, G.S. Laser-Induced Breakdown Spectroscopy (LIBS) applied to terrestrial and extraterrestrial analogue geomaterials with emphasis to minerals and rocks. *Earth-Science Rev.* **2014**, *139*, 231–267, doi:10.1016/j.earscirev.2014.09.008.
5. El Haddad, J.; de Lima Filho, E.S.; Vanier, F.; Harhira, A.; Padioleau, C.; Sabsabi, M.; Wilkie, G.; Blouin, A. Multiphase mineral identification and quantification by laser-induced breakdown spectroscopy. *Miner. Eng.* **2019**, *134*, 281–290, doi:10.1016/j.mineng.2019.02.025.
6. Lanari, P.; Vho, A.; Bovay, T.; Airaghi, L.; Centrella, S. Quantitative compositional mapping of mineral phases by electron probe micro-analyser. *Geol. Soc. Spec. Publ.* **2019**, *478*, 39–63, doi:10.1144/SP478.4.
7. Srivastava, P.K.; Krishna, A.P.; Jawed, S.; Sarkhel, P. Quantitative Minerological Analysis of Some Granite Rocks of Deoghar Jharkhand. *Earth Sci. Res.* **2020**, *9*, 30, doi:10.5539/esr.v9n2p30.
8. Zhang, Y.; Li, M.; Han, S.; Ren, Q.; Shi, J. Intelligent identification for rock-mineral microscopic images using ensemble machine learning algorithms. *Sensors* **2019**, *19*, doi:10.3390/s19183914.
9. Köse, C.; Alp, I.; Ikibaş, C. Statistical methods for segmentation and quantification of minerals in ore microscopy. *Miner. Eng.* **2012**, *30*, 19–32,

doi:10.1016/j.mineng.2012.01.008.

10. Aligholi, S.; Khajavi, R.; Razmara, M. Automated mineral identification algorithm using optical properties of crystals. *Comput. Geosci.* **2015**, *85*, 175–183, doi:10.1016/j.cageo.2015.09.014.
11. Asmussen, P.; Conrad, O.; Günther, A.; Kirsch, M.; Riller, U. Semi-automatic segmentation of petrographic thin section images using a “seeded-region growing algorithm” with an application to characterize wheathered subarkose sandstone. *Comput. Geosci.* **2015**, *83*, 89–99, doi:10.1016/j.cageo.2015.05.001.
12. Izadi, H.; Sadri, J.; Bayati, M. An intelligent system for mineral identification in thin sections based on a cascade approach. *Comput. Geosci.* **2017**, *99*, 37–49, doi:10.1016/j.cageo.2016.10.010.
13. Liu, C.; Li, M.; Zhang, Y.; Han, S.; Zhu, Y. An enhanced rock mineral recognition method integrating a deep learning model and clustering algorithm. *Minerals* **2019**, *9*, doi:10.3390/min9090516.
14. Dąbrowska, S.; Chudoba, T.; Wojnarowicz, J.; Łojkowski, W. Current trends in the development of microwave reactors for the synthesis of nanomaterials in laboratories and industries: A review. *Crystals* **2018**, *8*, doi:10.3390/cryst8100379.
15. Priecel, P.; Lopez-Sanchez, J.A. Advantages and Limitations of Microwave Reactors: From Chemical Synthesis to the Catalytic Valorization of Biobased Chemicals. *ACS Sustain. Chem. Eng.* **2019**, *7*, 3–21, doi:10.1021/acssuschemeng.8b03286.
16. Llompart, M.; Celeiro, M.; Dagnac, T. Microwave-assisted extraction of pharmaceuticals, personal care products and industrial contaminants in the environment. *TrAC - Trends Anal. Chem.* **2019**, *116*, 136–150, doi:10.1016/j.trac.2019.04.029.
17. Wei, W.; Shao, Z.; Zhang, Y.; Qiao, R.; Gao, J. Fundamentals and applications of microwave energy in rock and concrete processing – A review. *Appl. Therm. Eng.* **2019**, *157*, 113751, doi:10.1016/j.applthermaleng.2019.113751.
18. Kahraman, S.; Canpolat, A.N.; Fener, M. The influence of microwave treatment on the compressive and tensile strength of igneous rocks. *Int. J. Rock Mech. Min. Sci.* **2020**, *129*, 104303, doi:10.1016/j.ijrmms.2020.104303.
19. Lu, G.M.; Feng, X.T.; Li, Y.H.; Zhang, X. The Microwave-Induced Fracturing of Hard Rock. *Rock Mech. Rock Eng.* **2019**, *52*, 3017–3032, doi:10.1007/s00603-019-01790-z.
20. Wang, J. peng; Jiang, T.; Liu, Y. jing; Xue, X. xin Influence of microwave treatment on grinding and dissociation characteristics of vanadium titano-magnetite. *Int. J. Miner. Metall. Mater.* **2019**, *26*, 160–167, doi:10.1007/s12613-019-1720-1.
21. Guo, L.; Lan, J.; Du, Y.; Zhang, T.C.; Du, D. Microwave-enhanced selective leaching of arsenic from copper smelting flue dusts. *J. Hazard. Mater.* **2020**, *386*, 121964, doi:10.1016/j.jhazmat.2019.121964.
22. López-Buendía, A.M.; Guillem, C.; Cuevas, J.M.; Mateos, F.; Montoto, M. Natural stone reinforcement of discontinuities with resin for industrial processing.

Eng. Geol. **2013**, *166*, 39–51, doi:10.1016/j.enggeo.2013.09.004.

23. Krupka, J. Frequency domain complex permittivity measurements at microwave frequencies. *Meas. Sci. Technol.* **2006**, *17*, R55–R70, doi:10.1088/0957-0233/17/6/R01.

24. García-Baños, B.; Cuesta-Soto, F.; Griol, A.; Catalá-Civera, J.M.; Pitarch, J. Enhancement of sensitivity of microwave planar sensors with EBG structures. *IEEE Sens. J.* **2006**, *6*, 1518–1522, doi:10.1109/JSEN.2006.884506.

25. Pitarch, J.; Contelles-Cervera, M.; Pêaranda-Foix, F.L.; Catalá-Civera, J.M. Determination of the permittivity and permeability for waveguides partially loaded with isotropic samples. *Meas. Sci. Technol.* **2006**, *17*, 145–152, doi:10.1088/0957-0233/17/1/024.

26. Pérez-Campos, R.; Fayos-Fernández, J.; Lozano-Guerrero, A.J.; Martínez-González, A.; Monzó-Cabrera, J.; Mediavilla, I.; Peña-Carro, D.; Esteban-Pascual, L.S. Permittivity measurements for cypress and rockrose biomass versus temperature, density, and moisture content. *Sensors* **2020**, *20*, 4684, doi:10.3390/s20174684.

27. Neira, L.M.; Mays, R.O.; Sawicki, J.F.; Schulman, A.; Harter, J.; Wilke, L.G.; Behdad, N.; Van Veen, B.D.; Hagness, S.C. A pilot study of the impact of microwave ablation on the dielectric properties of breast tissue. *Sensors* **2020**, *20*, 1–15, doi:10.3390/s20195698.

28. González-Teruel, J.D.; Jones, S.B.; Soto-Valles, F.; Torres-Sánchez, R.; Lebron, I.; Friedman, S.P.; Robinson, D.A. Dielectric spectroscopy and application of mixing models describing dielectric dispersion in clay minerals and clayey soils. *Sensors (Switzerland)* **2020**, *20*, 1–18, doi:10.3390/s20226678.

29. Oliveira, J.G.D.; Junior, J.G.D.; Pinto, E.N.M.G.; Neto, V.P.S.; D'Assunção, A.G. A new planar microwave sensor for building materials complex permittivity characterization. *Sensors (Switzerland)* **2020**, *20*, 1–15, doi:10.3390/s20216328.

30. Gutierrez-Cano, J.D.; Plaza-Gonzalez, P.; Canos, A.J.; Garcia-Banos, B.; Catala-Civera, J.M.; Penaranda-Foix, F.L. A New Stand-Alone Microwave Instrument for Measuring the Complex Permittivity of Materials at Microwave Frequencies. *IEEE Trans. Instrum. Meas.* **2020**, *69*, doi:10.1109/TIM.2019.2941038.

31. Lu, G.; Zhou, J.; Li, Y.; Zhang, X.; Gao, W. The influence of minerals on the mechanism of microwave-induced fracturing of rocks. *J. Appl. Geophys.* **2020**, *180*, 104123, doi:10.1016/j.jappgeo.2020.104123.

32. Deyab, S.M.; Rafezi, H.; Hassani, F.; Kermani, M.; Sasmito, A.P. Experimental investigation on the effects of microwave irradiation on kimberlite and granite rocks. *J. Rock Mech. Geotech. Eng.* **2021**, *13*, 267–274, doi:10.1016/j.jrmge.2020.09.001.

33. Lovás, M.; Kováčová, M.; Dimitrakis, G.; Čuvanová, S.; Znamenáčková, I.; Jakabský, Š. Modeling of microwave heating of andesite and minerals. *Int. J. Heat Mass Transf.* **2010**, *53*, 3387–3393, doi:10.1016/j.ijheatmasstransfer.2010.03.012.

34. Pittella, E.; Angrisani, L.; Cataldo, A.; Piuzzi, E.; Fabbrocino, F. Embedded Split Ring Resonator Network for Health Monitoring in Concrete Structures. *IEEE*

Instrum. Meas. Mag. **2020**, *23*, 14–20, doi:10.1109/MIM.2020.9289070.

35. D'Alvia, L.; Pittella, E.; Rizzuto, E.; Piuzzi, E.; Del Prete, Z. A portable low-cost reflectometric setup for moisture measurement in cultural heritage masonry unit. *Meas. J. Int. Meas. Confed.* **2021**, *189*, 110438, doi:10.1016/j.measurement.2021.110438.

36. Zheng, Y.L.; Zhao, X.B.; Zhao, Q.H.; Li, J.C.; Zhang, Q.B. Dielectric properties of hard rock minerals and implications for microwave-assisted rock fracturing. *Geomech. Geophys. Geo-Energy Geo-Resources* **2020**, *6*, doi:10.1007/s40948-020-00147-z.

37. Zheng, Y.; Sun, T. A method to derive the dielectric loss factor of minerals from microwave heating rate tests. *Meas. J. Int. Meas. Confed.* **2021**, *171*, 108788, doi:10.1016/j.measurement.2020.108788.

38. Anlage, S.M.; Talanov, V. V; Schwartz, A.R. Principles of Near-Field Microwave Microscopy. In *Scanning Probe Microscopy: Electrical and Electromechanical Phenomena at the Nanoscale*; Kalinin, S., Gruverman, A., Eds.; Springer New York: New York, NY, 2007; pp. 215–253 ISBN 978-0-387-28668-6.

39. Vlahacos, C.P.; Black, R.C.; Anlage, S.M.; Amar, A.; Wellstood, F.C. Near-field scanning microwave microscope with 100 μm resolution. *Appl. Phys. Lett.* **1996**, *69*, 3272–3274, doi:10.1063/1.118033.

40. Gregory, A.P.; Blackburn, J.F.; Lees, K.; Clarke, R.N.; Hodgetts, T.E.; Hanham, S.M.; Klein, N. Measurement of the permittivity and loss of high-loss materials using a Near-Field Scanning Microwave Microscope. *Ultramicroscopy* **2016**, *161*, 137–145, doi:10.1016/j.ultramic.2015.11.015.

41. Ramzi, M.R.; Abou-Khousa, M.; Prayudi, I. Near-field microwave imaging using open-ended circular waveguide probes. *IEEE Sens. J.* **2017**, *17*, 2359–2366, doi:10.1109/JSEN.2017.2669301.

42. Xie, Z.; Li, Y.; Sun, L.; Wu, W.; Cao, R.; Tao, X. A simple high-resolution near-field probe for microwave non-destructive test and imaging. *Sensors (Switzerland)* **2020**, *20*, 1–15, doi:10.3390/s20092670.

43. Imtiaz, A.; Wallis, T.M.; Kabos, P. Near-Field Scanning Microwave Microscopy: An Emerging Research Tool for Nanoscale Metrology. *IEEE Microw. Mag.* **2014**, *15*, 52–64, doi:10.1109/MMM.2013.2288711.

44. Paulson C.A.; Van Der Weide D.W. Near-Field High-Frequency Probing. In *Scanning Probe Microscopy*; Kalinin S., G.A., Ed.; Springer New York: New York, NY, 2007; pp. 315–345 ISBN 978-0-387-28668-6.

45. Tabib-Azar, M.; Zhang, T.; LeClair, S.R. Self-oscillating evanescent microwave probes for nondestructive evaluations of materials. *IEEE Trans. Instrum. Meas.* **2002**, *51*, 1126–1132, doi:10.1109/TIM.2002.807798.

46. Wu, B.Y.; Sheng, X.Q.; Fabregas, R.; Hao, Y. Full-wave modeling of broadband near field scanning microwave microscopy. *Sci. Rep.* **2017**, *7*, 1–10, doi:10.1038/s41598-017-13937-5.

47. Gao, C.; Xiang, X.D. Quantitative microwave near-field microscopy of dielectric properties. *Rev. Sci. Instrum.* **1998**, *69*, 3846–3851, doi:10.1063/1.1149189.

48. Gao, C.; Hu, B.; Takeuchi, I.; Chang, K.S.; Xiang, X.D.; Wang, G. Quantitative

scanning evanescent microwave microscopy and its applications in characterization of functional materials libraries. *Meas. Sci. Technol.* **2005**, *16*, 248–260, doi:10.1088/0957-0233/16/1/033.

49. Cheng, H.F.; Chen, Y.C.; Lin, I.N. Evanescent microwave probe study on dielectric properties of materials. *J. Eur. Ceram. Soc.* **2006**, *26*, 1801–1805, doi:10.1016/j.jeurceramsoc.2005.09.034.

50. Kimber, D.P.; Pullar, R.C.; Alford, N.M.N. The effects of dielectric loss and tip resistance on resonator Q of the scanning evanescent microwave microscopy (SEMM) probe. *Meas. Sci. Technol.* **2008**, *19*, 2–6, doi:10.1088/0957-0233/19/11/115502.

51. Geaney, S.; Cox, D.; Hönigl-Decrinis, T.; Shaikhaidarov, R.; Kubatkin, S.E.; Lindström, T.; Danilov, A. V.; de Graaf, S.E. Near-Field Scanning Microwave Microscopy in the Single Photon Regime. *Sci. Rep.* **2019**, *9*, 1–7, doi:10.1038/s41598-019-48780-3.

52. Tselev, A.; Yu, P.; Cao, Y.; Dedon, L.R.; Martin, L.W.; Kalinin, S. V.; Maksymovych, P. Microwave a.c. conductivity of domain walls in ferroelectric thin films. *Nat. Commun.* **2016**, *7*, 1–9, doi:10.1038/ncomms11630.

53. Gangwar, A.K.; Kanika; Kedawat, G.; Papanai, G.S.; Gupta, B.K. Single excitable dual emissive novel luminescent pigment to generate advanced security features for anti-counterfeiting applications. *J. Mater. Chem. C* **2019**, *7*, 13867–13877, doi:10.1039/c9tc04492b.

54. Tai, T.; Ghamsari, B.G.; Bieler, T.R.; Tan, T.; Xi, X.X.; Anlage, S.M. Near-field microwave magnetic nanoscopy of superconducting radio frequency cavity materials. *Appl. Phys. Lett.* **2014**, *104*, 6–10, doi:10.1063/1.4881880.

55. Hoffmann, J.; Gramse, G.; Niegemann, J.; Zeier, M.; Kienberger, F. Measuring low loss dielectric substrates with scanning probe microscopes. *Appl. Phys. Lett.* **2014**, *105*, 1–5, doi:10.1063/1.4886965.

56. Farina, M.; Jin, X.; Fabi, G.; Pavoni, E.; Di Donato, A.; Mencarelli, D.; Morini, A.; Piacenza, F.; Al Hadi, R.; Zhao, Y.; et al. Inverted scanning microwave microscope for in vitro imaging and characterization of biological cells. *Appl. Phys. Lett.* **2019**, *114*, 8–11, doi:10.1063/1.5086259.

57. Monti, T.; Tselev, A.; Udoudo, O.; Ivanov, I.N.; Dodds, C.; Kingman, S.W. High-resolution dielectric characterization of minerals: A step towards understanding the basic interactions between microwaves and rocks. *Int. J. Miner. Process.* **2016**, *151*, 8–21, doi:10.1016/j.minpro.2016.04.003.

58. Gutiérrez-Cano, J.D.; Catalá-Civera, J.M.; Plaza-González, P.J.; Peñaranda-Foix, F.L. Detection of anti-counterfeiting markers through permittivity maps using a micrometer scale near field scanning microwave microscope. *Sensors* **2021**, *21*, doi:10.3390/s21165463.

59. Caja, M.Á.; Peña, A.C.; Campos, J.R.; Diego, L.G.; Tritlla, J.; Bover-Arnal, T.; Martín-Martín, J.D. Image processing and machine learning applied to lithology identification, classification and quantification of thin section cutting samples. *Proc. - SPE Annu. Tech. Conf. Exhib.* **2019**, *2019-Septe*, doi:10.2118/196117-ms.

60. Acosta, I.C.C.; Khodadadzadeh, M.; Tusa, L.; Ghamisi, P.; Gloaguen, R. A

Machine learning framework for drill-core mineral mapping using hyperspectral and high-resolution mineralogical data fusion. *IEEE J. Sel. Top. Appl. Earth Obs. Remote Sens.* **2019**, *12*, 4829–4842, doi:10.1109/JSTARS.2019.2924292.

61. Harraden, C.L.; Cracknell, M.J.; Lett, J.; Berry, R.F.; Carey, R.; Harris, A.C. Automated core logging technology for geotechnical assessment: A study on core from the Cadia East porphyry deposit. *Econ. Geol.* **2019**, *114*, 1495–1511, doi:10.5382/econgeo.4649.

62. Metaxas, A.C. Microwave heating. *Power Eng. J.* **1991**, *5*, 237–247, doi:10.1049/pe:19910047.

63. Kajfez, D. Linear Fractional Curve Fitting for Measurement of High Q Factors. *IEEE Trans. Microw. Theory Tech.* **1994**, *42*, 1149–1153, doi:10.1109/22.299749.

64. Darko Kajfez *Q-Factor*; Vector Fields: Oxford, MS, USA, 1994;

65. Kleismit, R. a; Kazimierczuk, M.K.; Kozlowski, G. Sensitivity and Resolution of Evanescent Microwave Microscope. *IEEE Trans. Microw. Theory Tech.* **2006**, *54*, 1–9.

66. Altschuler, H.M. Dielectric constant. In *Handbook of Microwave Measurements*; Sucher, M., Fox, J., Eds.; Polytech. Inst. Brooklyn Press: New York, NY, USA, 1963.

67. Khanna, S.K.; Ehrenfreund, E.; Garito, A.F.; Heeger, A.J. Microwave properties of high-purity tetrathiofulvalene-tetracyanoquinodimethan (TTF-TCNQ). *Phys. Rev. B* **1974**, *10*, 2205–2220, doi:10.1103/PhysRevB.10.2205.

68. Mao, W.; Wu, L.; Qi, Y. Impact of Compressive Stress on Microwave Dielectric Properties of Feldspar Specimen. *IEEE Trans. Geosci. Remote Sens.* **2020**, *58*, 1398–1408, doi:10.1109/TGRS.2019.2946155.

69. Zheng, Y.; Wang, S.; Feng, J.; Ouyang, Z.; Li, X. Measurement of the complex permittivity of dry rocks and minerals: Application of polythene dilution method and Lichtenecker's mixture formulae. *Geophys. J. Int.* **2005**, *163*, 1195–1202, doi:10.1111/j.1365-246X.2005.02718.x.

70. Church, R.H.; Webb, W.E.; Salsman, J.B. *Dielectric Properties of Low-Loss Minerals. Vol. 9194*; 1988;

71. Nelson, S.; Lindroth, D.; Blake, R. Dielectric properties of selected and purified minerals at 1 to 22 GHz. *J. Microw. Power Electromagn. Energy* **1989**, *24*, 213–220, doi:10.1080/08327823.1989.11688096.

72. Harrison, P.C. A fundamental study of the heating effect of 2.45 GHz microwave radiation on minerals, University of Birmingham, 1997.

73. Zhang, B.; Yan, G.; Zhao, Y.; Zhou, C.; Lu, Y. Coal pyrite microwave magnetic strengthening and electromagnetic response in magnetic separation desulfurization process. *Int. J. Miner. Process.* **2017**, *168*, 136–142, doi:10.1016/j.minpro.2017.10.004.

74. Penaranda-Foix, F.L.; Janezic, M.D.; Catala-Civera, J.M.; Canos, A.J. Full-wave analysis of dielectric-loaded cylindrical waveguides and cavities using a new four-port ring network. *IEEE Trans. Microw. Theory Tech.* **2012**, *60*, 2730–2740, doi:10.1109/TMTT.2012.2206048.

75. Duarte, F.A.; Waechter, S.R.; Pedrotti, M.F.; Pardinho, R.B.; Flores, E.M.M.; Barin, J.S. Microwave-Induced Combustion in Disposable Vessels: A Novel Perspective for Sample Digestion. *Anal. Chem.* **2020**, *92*, 8058–8063, doi:10.1021/acs.analchem.0c01017.

76. Lu, G. ming; Li, Y. hui; Hassani, F.; Zhang, X. The influence of microwave irradiation on thermal properties of main rock-forming minerals. *Appl. Therm. Eng.* **2017**, *112*, 1523–1532, doi:10.1016/j.applthermaleng.2016.11.015.

77. Pandey, C.S.; Jodlauk, S.; Schreuer, J. Correlation between dielectric properties and chemical composition of the tourmaline single crystals. *Appl. Phys. Lett.* **2011**, *99*, 6–9, doi:10.1063/1.3646912.

Chapter 6

General Discussion

6.1 A stand-alone, portable, and easy-to-use dielectrometer

One of the main objectives of the thesis was to develop measurement cells to cover the dielectric characterization needs of the project SEDMICRON. The characterization of the materials to be used as hidden markers was out of the scope of this work. Nevertheless, the objective of this thesis was to identify alternative applications that could benefit from the techniques developed for the project. Thus, I aimed to adapt some of these cells to different environments, either by devising easy-to-use versatile systems, or by adjusting these cells for specific applications. The publications presented in chapters 2 and 3 cover these objectives.

The paper in Chapter 2 [1] describes the development of a portable, easy-to-use, and stand-alone device for complex permittivity characterization. The features of this design allow straightforward use by non-specialized personnel and provide versatility in many situations.

The main element of the device is the microwave cell, a reentrant cavity similar to the concept reported in [2,3] and modified to house pyrex tubes passing through its central axis. The tube configuration allows the measurement of materials in different forms, such as liquids, semisolids, powders, granular, and solid materials at room temperature. The structure is very sensitive because it maximizes the field intensity in the capacitance gap [4]. The single-mode employed in the proposed implementation exhibited a frequency shift from 1900MHz to 2500MHz for materials with a dielectric constant ranging from 1 to 100, a remarkable result considering the small amount of material inside the cavity. In addition, the study of the strong feeding network employed in the cavity enables the characterization of low, moderate, and high-loss materials with the same setup. These features make this microwave cavity perfect to be used in a wide range of situations.

The geometry of this reentrant cavity has significant potential. During this doctoral work, I employed this geometry as a basis for other works not included in this thesis dissertation.

In [5], we designed two cavities with the same reentrant geometry as the cavity reported in chapter 2 but with different dimensions to allow broadband measurements utilizing multiple modes with both cavities (see Fig. **1**. Five resonant modes were analyzed in the large cavity, covering a discrete bandwidth from 170MHz to 2.3 GHz. The cavity with the smaller size covered a frequency range from 1.3 to 8.6GHz through four different modes.

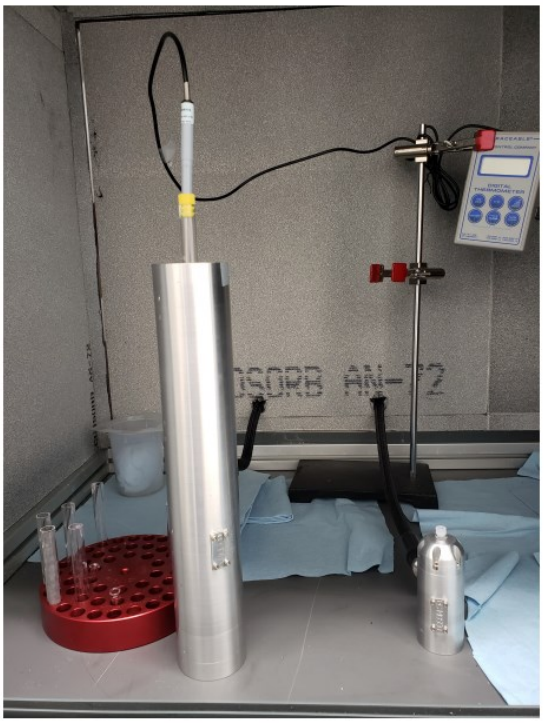

Fig. **1**: Multipoint reentrant cavities employed to determine the permittivity spectrum of low-loss liquid and powder geomaterials.

In this work, quartz tubes were employed to allow measurements as a function of temperature. The probes were used to measure permittivity values of medium-grade crude oil at 25ºC and 50ºC. Besides, the permittivity values of kerogen and cement powders with medium to high losses were also determined. The measurement procedure was more complex compared to the work reported in chapter 2 due to the difficulty of proper mode identification, as remarked in the Introduction (Chapter 1).

The second work worth mentioning at this point is a new method for broadband permittivity measurements of medium to high losses materials (see Fig. **2**). This technique is among the probes developed in this doctoral work within the framework of the SEDMICRON project. Still, the publication was not completed when writing this document, so it could not be included. The microwave probe is based again on the single reentrant coaxial cavity of chapter 2, adapted to measure as a non-resonant cell to allow broadband measurements. In the measurement campaign carried out to prepare the manuscript to be submitted for a future publication, the method's performance was assessed by a comparative analysis with well-known alcohols and saline solutions with good agreements with the reference data.

The following essential aspect in Chapter 2 is the technique to analyze the microwave structure, the approach to relate the measurable quantities to the permittivity values. The works described in this thesis dissertation used circuit analysis and mode-matching [6,7] or the cavity perturbation method [8–10]. The first technique was employed in the papers described in chapters 2 and 3. Itaca-Dimas group has extensive experience analyzing

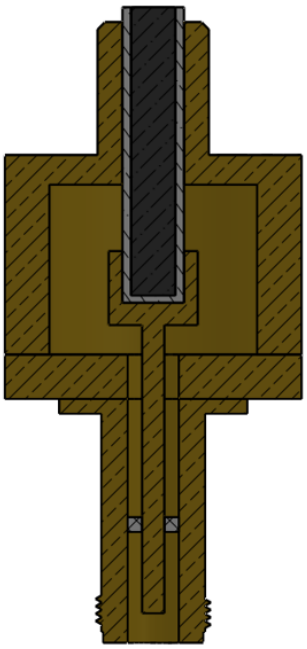

Fig. **2**: Schematic of the microwave cell based on the bi-reentrant geometry with appropriate modifications as a reflection probe for wideband permittivity measurements of lossy materials.

structures using this technique and has developed Matlab libraries to evaluate complex microwave geometries quickly and straightforwardly. Besides, the numerical method allows an exhaustive analysis of the measurement uncertainty because it considers all the variables of the microwave cell geometry.

As discussed in chapter 1, one of the most critical reasons for the limited spread of microwave sensors is the high cost of this technology, mainly the price of the measurement devices [11]. To overcome this drawback, this device includes a portable vector reflectometer that operates around the ISM frequency band of 2.45GHz. The microwave signal generator is composed of a PLL frequency synthesizer. The receiver compares the magnitude and the phase of the forward and reflected signals in the microwave cavity employing two gain and phase receiver units to solve the phase ambiguity, as explained in the corresponding chapter. Finally, a microprocessor digitalizes the transmitted and received signals and establishes communication to a computer via a serial link.

A specific objective of the thesis was to develop solutions for measuring dielectric properties that non-specialized users could straightforwardly operate. To that end, a user-friendly LabVIEW-based software was developed to control the measurement process, determine the resonant frequency and quality factor from the reflection measurement, remove the influence of the coupling network, compute the permittivity from the resonant parameters, and display the results. In addition, the cavity and all circuitry were assembled in a compact and portable housing to achieve an easy-to-use and stand-alone measurement solution. The results obtained with this final setup showed

outstanding accuracy, within the range of 1.5% for the dielectric constant and constrained around 5% for loss factor values ranging from 10^{-3} to 10^{1}.

6.2 Permittivity characterization of food products at RF

Chapter 3 presents a less generic device, adapted to be used in a specific application, based in a coaxial probe with good accuracy for permittivity measurements of lossy food products at RF frequencies.

As discussed in chapter 1, the food industry is one of the principal users of microwave and RF techniques to improve its production processes. In the early stages of these doctoral studies, I was involved in other works to study the dielectric properties of starch-based food pellets during microwave expansion. This study aimed to provide information to improve the overall design of starch-based food pellets to enhance the expansion process under microwaves irradiation. The results of this work were published in two scientific papers [12,13]. Although these papers also include permittivity methods adapted to a particular environment or application, they have not been included in the chapters of this dissertation because they are not directly related to the SEDMICRON project. Both papers utilized the dual-mode cylindrical cavity depicted in Fig. **2** that allows simultaneous microwave heating and dielectric characterization. In the first publication [12], this system was adapted to account for the unique shape and behavior of the pellet.

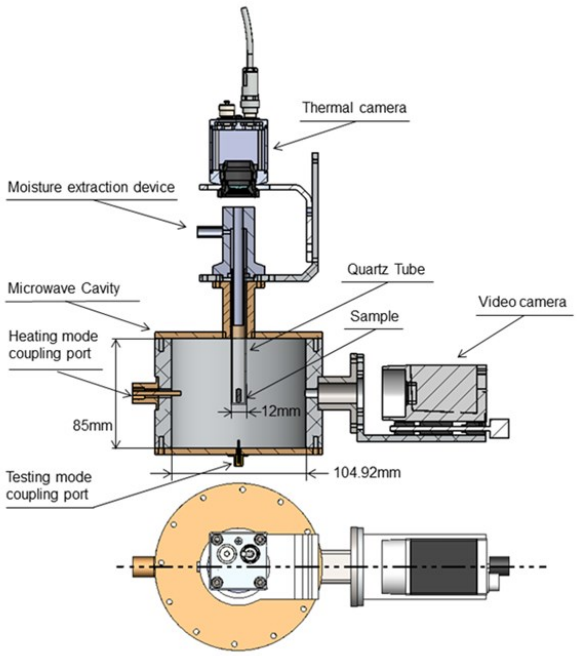

Fig. **3**: Number of scientific papers published in the period from 2000 to 2021 identified when searching for the words "dielectric properties" and "permittivity". Source: ScienceDirect

The method developed to include the volume changes during microwave heating in the permittivity values was quite challenging and worth mentioning. In the second publication [13], we assessed the effect of moisture on the expansion dynamics of similar starch-based food pellets by studying their dielectric properties.

Permittivity depends on many parameters, the most critical being frequency, material dielectric losses, and temperature [14]. Thus, the choice of the appropriate measurement method plays a relevant role in the accuracy of the permittivity results. It is well known that keysight coaxial probes (formerly HP and Agilent) are possibly the most widely used method for the dielectric characterization of materials. However, it is not the best measurement technique for all situations. In a bibliographic review, I observed that many scientific papers reported permittivity of lossy food products below 200MHz employing that probe and a VNA [15–18]. Considering the high demand for permittivity measurements with temperature at RF frequencies in this field, we decided to adapt one of our probes for this specific environment, highlighting the high uncertainty of many published results on this topic.

The text fixture comprised a coaxial line connected to a cylindrical vessel to place the sample. Some elements of the test fixture had to be specially designed to withstand temperatures up to 120ºC. The coaxial bead was made of a material with a negligible coefficient of linear thermal expansion and stable dielectric behavior. A coaxial line with a built-in heat sink was designed to cool down and protect the connection to the VNA, simultaneously avoiding calibration drifts. The seal of the cylindrical vessel employed a piston and O-rings to prevent air bubbles and withstand the pressure at high temperatures. Finally, specific elements were included to protect the end user from burns.

As reported in the paper in chapter 2, circuit analysis and mode-matching were utilized again to model the cell's response in this publication. This model was first used to optimize the cell's dimensions to maximize the sensitivity of the electromagnetic response at RF frequencies. Once the structure was manufactured, it was employed to retrieve permittivity values from reflection coefficient measurements. This analysis had certain advantages. First, since metal walls confined the coaxial aperture, we avoided some assumptions typically made when analyzing open-ended coaxial probes [19–21] and considered the transition between the coaxial and the loaded cylindrical waveguide. Second, the whole geometry was studied avoiding the need for calibration with known materials, as it is usually done with this type of probe [22].

The electromagnetic model was also used to present the probe's response to different dielectric materials and perform a comprehensive analysis of the measurement uncertainty. For comparison purposes, the response of the Agilent coaxial probe was also reproduced. In my study, the probe covered an area of the Smith Chart six times larger than the area covered by the small coaxial cell for the same frequency and set of materials. This higher sensitivity was also highlighted in the uncertainty study. The analysis revealed an uncertainty below 5% for dielectric constant values between 20 and 100 and below 2% for the loss factor values above 250. For the same set of materials, the uncertainty of the small probe was above 20% for the dielectric constant and around 10% for the loss factor. The good performance of our probe was confirmed by measurements of saline solutions with different salt content.

This development was used to determine the dielectric properties of lossy food products at 40.68 MHz up to 120 °C. The comparison of the results with those reported by other authors was discrepant in some cases, which highlighted the relevance of using cells adapted to the specific conditions of the material and considering the frequency limitations of the measurement technique.

6.3 Detection of anti-counterfeiting markers through a near-field scanning microwave microscope.

Chapter 4 presents the development of a near-field scanning microwave microscope (NSMM) for the authentication of markers in document security applications, the published document describing the specific work of this thesis performed to meet the main objectives of the SEDMICRON project. The following specific goals were addressed to achieve these goals.

First, we considered the tasks needed to meet the objective of creating the NSMM and its different subsystems. An NSMM device usually includes a near-field probe, a VNA, and a positioning stage [23]. These tasks were described thoroughly in chapter 4, but I will briefly summarize them below.

The design of near-field probe includes the development of the aperture and the microwave structure in which it is included. There are many solutions to address both aspects [23–25]. The most common setup was chosen for our development, a sharp coaxial tip included in a resonant structure. Regarding the VNA device, I tried again to achieve stand-alone and easy-to-use functionality. For that purpose, an in-house single port reflectometer similar to the device described in chapter 2 was enmployed, but with some improvements conducted to include the control of the positioning stage to increase the system's speed. For the positioning subsystem, a vacuum table was mounted over an XY-stage for pixel-by-pixel scanning.

The vertical positioning of the sensor was performed through a manually-driven micrometric positioner. In the initial stages of the project, this element was considered sufficient to achieve the project's objectives. To some extent, this was true, as demonstrated in section 4.4.3 of chapter 4, where a good detection of the marker was shown without the need for additional elements. However, the measurement reveals certain imperfections due to the non-horizontality of the XY table. The resonant frequency retrieved for a specific material is strongly influenced by the tip-to-sample distance, as depicted in Figure 4 of chapter 4. Accordingly, I needed to include an element to track the tip-to-sample distance to measure dielectric properties. An additional microscope, such as atomic force microscopes (AFM) or scanning tunneling microscopes (STM), is required to achieve very low spatial resolutions in the typical soft-contact setups [26–28]. However, aiming for robustness, we tried to employ probe-to-sample distances around 100um, avoiding soft contact. To that end, a commercial laser displacement sensor was used to track the tip-to-sample distance and thus be able to perform permittivity measurements.

All subsystems were integrated into a compact and stand-alone housing. A LabVIEW software and the Arduino board control the scanning process, capture the laser reading, and perform the reflection coefficient measurement. Then, the LabVIEW software

determines all the necessary parameters to calculate and display the dielectric mark of the material under test.

In contrast to the work presented in Chapters 2 and 3, where circuit analysis and mode matching were employed to model the cell's response, the cavity perturbation method (CPM) was used in this work since the electromagnetic fields inside the sample are much smaller than the fields in the resonator. In addition, the field distribution can be considered a static problem in the near-field zone, and phase and retardation need not be considered [29]. The model parameters were calculated by measuring reference materials of known dielectric properties. Regression curves relating these parameters with the tip-to-sample distances were determined to account for the tip-to-sample variations during scans. The response of this probe showed a limited sensitivity to loss factor variations; thus, only the dielectric constant values of the materials under test were determined in this work. The dielectric characterization of materials with known permittivity was determined to assess the capabilities of the NSMM device. This study revealed errors below 5%.

Diverse security features detectable at different wavelengths are included to protect official documents, such as passports or banknotes [30]. Watermarks are among the best-known security features and are usually detected in the visible spectrum. In my work, the use of microwave energy to detect anti-counterfeiting markers was described for the first time by measuring the dielectric mark of banknote watermarks, which covers the thesis's objective in this regard. In these trials, the developed NSMM was able to trace the density changes inside the banknote watermarks. Besides, watermarks were detected even hidden behind a dielectric or metallic layer, exploiting the penetration depth of microwaves, opening new possibilities for developing optically opaque security features untraceable by optical means.

In the last section of chapter 4, I analyzed the single frequency approach. This concept was the solution considered in the earliest stages of the project due to its simplicity and speed. However, the dielectric characterization of materials would be complex since this technique did not retrieve the full resonance. Therefore, it is the ideal solution for sensing and detection works. This approach may be the best solution for an application developed to detect anti-counterfeiting markers through microwave technology, but it is not a suitable option for permittivity characterization.

6.4 Complex permittivity maps of planar samples and its use in petrography studies

The final aim of the thesis was to increase the functionality of the microscope to allow measurements of complex permittivity of planar materials on a micrometric scale and identify applications that can benefit from the use of this device. Chapter 5 presents the last paper included in this dissertation, describing the work carried out to accomplish these objectives. I report the improvements made to provide capabilities to measure complex permittivity and the use of this device in the field of petrography.

The quality factor response of the probe in chapter 4 showed poor sensitivity to changes in the dielectric losses of the materials. Thus, the probe was redesigned to increase the sensitivity of the quality factor. The analysis of the response of the new probe exhibited similar curves for the resonant frequency. Nevertheless, the curves of the quality factor

revealed measurable variations reflecting changes in the loss factor of the dielectric materials, which would allow loss factor measurements.

The cavity perturbation method employed in chapter 4 could not model the response of the redesigned probe. Therefore, I turned to the most widely used technique to describe the behaviour of this type of probe, a method developed by Gao and Xiang [31]. However, we found a variation of the model parameters depending on the dielectric constant of the measured material. A combination of the classical CPM with an evolution of the Gao and Xiang model proposed by Gregory et al. [32] was finally employed to analyse the behavior of this probe. The performance of the NSMM with enhanced sensitivity for permittivity characterization was addressed by a comparative analysis with other well-established instruments validating the proposed measurement technique. The NSMM device was now ready to perform contactless permittivity measurements of planar materials, achieving this particular goal aimed in the thesis objectives.

The development of a stand-alone device capable of measuring the dielectric properties of heterogeneous planar materials is a significant achievement that can be employed in a broad range of microwave applications. In the work reported in chapter 5, I utilize these capabilities in the field of petrography.

As in other fields of knowledge, the rock industry is paying growing attention to microwave technology to improve its processes [33,34]. Thus, permittivity characterization is needed to ascertain the potential of rocks to absorb microwave energy and design the microwave applicators properly. Since rocks are heterogeneous materials, the developed NSMM was appropriate to determine the permittivity maps of some representative specimens of ornamental rocks in the actual state in which they are found in the material. In this study, a traditional petrographic analysis was used to correlate the permittivity marks with the rock's mineral composition. Then, I was able to compare the permittivity values obtained for each mineral with the references found in different research works, with good agreement.

6.5 References

1. Gutierrez-Cano, J.D.; Plaza-Gonzalez, P.; Canos, A.J.; Garcia-Banos, B.; Catala-Civera, J.M.; Penaranda-Foix, F.L. A New Stand-Alone Microwave Instrument for Measuring the Complex Permittivity of Materials at Microwave Frequencies. *IEEE Trans. Instrum. Meas.* **2020**, *69*, doi:10.1109/TIM.2019.2941038.

2. Xi, W.; Tinga, W.R.; Voss, W.A.G.; Tian, B.Q. New Results for Coaxial Re-Entrant Cavity with Partially Dielectric Filled Gap. *IEEE Trans. Microw. Theory Tech.* **1992**, *40*, 747–753, doi:10.1109/22.127525.

3. Baker-Jarvis, J.; Riddle, B.F. *Dielectric Measurements Using a Reentrant Cavity: Mode-Matching Analysis*; 1996;

4. Clarke, R.; Gregory, A.; Cannell, D.; Patrick, M.; Wylie, S.; Youngs, I.; Hill, G. *A Guide to characterisation of dielectric materials at RF and microwave frequencies*; Institute of Measurement and Control and National Physical Laboratory: London, 2003; ISBN 0 904457 38 9.

5. Alvarez, J.O.; Penaranda-Foix, F.L.; Catala-Civera, J.M.; Gutierrez-Cano, J.D.

Permittivity Spectrum of Low-Loss Liquid and Powder Geomaterials Using Multipoint Reentrant Cavities. *IEEE Trans. Geosci. Remote Sens.* **2020**, *58*, doi:10.1109/TGRS.2019.2948052.

6. Peñaranda-Foix, F.L.; Catalá-Civera, J.M. Circuital Analysis of Cylindrical Structures Applied to the Electromagnetic Resolution of Resonant Cavities. In *Passive Microwave Components and Antennas*; Vitaliy Zhurbenko, Ed.; IntechOpen, 2010.

7. Penaranda-Foix, F.L.; Janezic, M.D.; Catala-Civera, J.M.; Canos, A.J. Full-wave analysis of dielectric-loaded cylindrical waveguides and cavities using a new four-port ring network. *IEEE Trans. Microw. Theory Tech.* **2012**, *60*, 2730–2740, doi:10.1109/TMTT.2012.2206048.

8. Bethe, H.A.; Schwinger, J. *Perturbation Theory for Cavities*; NDRC: Cornell University, Rpt. D1-117, 1943;

9. Altschuler, H.M. Dielectric constant. In *Handbook of Microwave Measurements*; Sucher, M., Fox, J., Eds.; Polytech. Inst. Brooklyn Press: New York, NY, USA, 1963.

10. Khanna, S.K.; Ehrenfreund, E.; Garito, A.F.; Heeger, A.J. Microwave properties of high-purity tetrathiofulvalene-tetracyanoquinodimethan (TTF-TCNQ). *Phys. Rev. B* **1974**, *10*, 2205–2220, doi:10.1103/PhysRevB.10.2205.

11. Kraszewski, A.W. Microwave Aquametry -Needs and Perspectives. *IEEE Trans. Microw. Theory Tech.* **1991**, *39*, 828–835, doi:10.1109/22.79110.

12. Gutiérrez, J.D.; Catalá-Civera, J.M.; Bows, J.; Peñaranda-Foix, F.L. Dynamic measurement of dielectric properties of food snack pellets during microwave expansion. *J. Food Eng.* **2017**, *202*, 1–8, doi:10.1016/j.jfoodeng.2017.01.021.

13. Gutiérrez-Cano, J.D.; Hamilton, I.E.; Catalá-Civera, J.M.; Bows, J.; Peñaranda-Foix, F.L. Effect of water content on the dynamic measurement of dielectric properties of food snack pellets during microwave expansion. *J. Food Eng.* **2018**, *232*, 21–28, doi:10.1016/j.jfoodeng.2018.03.018.

14. Piyasena, P.; Dussault, C.; Koutchma, T.; Ramaswamy, H.S.; Awuah, G.B. Radio Frequency Heating of Foods: Principles, Applications and Related Properties - A Review. *Crit. Rev. Food Sci. Nutr.* **2003**, *43*, 587–606, doi:10.1080/10408690390251129.

15. Guo, W.; Wu, X.; Zhu, X.; Wang, S. Temperature-dependent dielectric properties of chestnut and chestnut weevil from 10 to 4500 MHz. *Biosyst. Eng.* **2011**, *110*, 340–347, doi:10.1016/j.biosystemseng.2011.09.007.

16. Ling, B.; Guo, W.; Hou, L.; Li, R.; Wang, S. Dielectric Properties of Pistachio Kernels as Influenced by Frequency, Temperature, Moisture and Salt Content. *Food Bioprocess Technol.* **2015**, *8*, 420–430, doi:10.1007/s11947-014-1413-8.

17. Zhu, X.; Guo, W.; Jia, Y. Temperature-Dependent Dielectric Properties of Raw Cow's and Goat's Milk from 10 to 4,500 MHz Relevant to Radio-frequency and Microwave Pasteurization Process. *Food Bioprocess Technol.* **2014**, *7*, 1830–1839, doi:10.1007/s11947-014-1255-4.

18. Yang, R.L.; Zhu, Y.J.; Chen, F.F.; Dong, L.Y.; Xiong, Z.C. Luminescent, Fire-Resistant, and Water-Proof Ultralong Hydroxyapatite Nanowire-Based Paper for

Multimode Anticounterfeiting Applications. *ACS Appl. Mater. Interfaces* **2017**, *9*, 25455–25464, doi:10.1021/acsami.7b06835.

19. Baker-Jarvis, J.; Janezic, M.D.; Domich, P.D.; Geyer, R.G. Analysis of an Open-Ended Coaxial Probe with Lift-Off for Nondestructive Testing. *IEEE Trans. Instrum. Meas.* **1994**, *43*, 711–718, doi:10.1109/19.328897.

20. Bakhtiari, S.; Qaddoumi, N.; Ganchev, S.I.; Zoughi, R. Microwave Noncontact Examination of Disbond and Thickness Variation in Stratified Composite Media. *IEEE Trans. Microw. Theory Tech.* **1994**, *42*, 389–395, doi:10.1109/22.277431.

21. Blackham, D. V.; Pollard, R.D. An improved technique for permittivity measurements using a coaxial probe. *IEEE Trans. Instrum. Meas.* **1997**, *46*, 1093–1099, doi:10.1109/19.676718.

22. Keysight Technologies *Keysight 85070E Dielectric Probe Kit 200 MHz to 50 GHz*; 2014;

23. Kleismit, R. a; Kazimierczuk, M.K.; Kozlowski, G. Sensitivity and Resolution of Evanescent Microwave Microscope. *IEEE Trans. Microw. Theory Tech.* **2006**, *54*, 1–9.

24. Imtiaz, A.; Wallis, T.M.; Kabos, P. Near-Field Scanning Microwave Microscopy: An Emerging Research Tool for Nanoscale Metrology. *IEEE Microw. Mag.* **2014**, *15*, 52–64, doi:10.1109/MMM.2013.2288711.

25. Anlage, S.M.; Talanov, V. V; Schwartz, A.R. Principles of Near-Field Microwave Microscopy. In *Scanning Probe Microscopy: Electrical and Electromechanical Phenomena at the Nanoscale*; Kalinin, S., Gruverman, A., Eds.; Springer New York: New York, NY, 2007; pp. 215–253 ISBN 978-0-387-28668-6.

26. Tai, T.; Ghamsari, B.G.; Bieler, T.R.; Tan, T.; Xi, X.X.; Anlage, S.M. Near-field microwave magnetic nanoscopy of superconducting radio frequency cavity materials. *Appl. Phys. Lett.* **2014**, *104*, 6–10, doi:10.1063/1.4881880.

27. Hoffmann, J.; Gramse, G.; Niegemann, J.; Zeier, M.; Kienberger, F. Measuring low loss dielectric substrates with scanning probe microscopes. *Appl. Phys. Lett.* **2014**, *105*, 1–5, doi:10.1063/1.4886965.

28. Gangwar, A.K.; Kanika; Kedawat, G.; Papanai, G.S.; Gupta, B.K. Single excitable dual emissive novel luminescent pigment to generate advanced security features for anti-counterfeiting applications. *J. Mater. Chem. C* **2019**, *7*, 13867–13877, doi:10.1039/c9tc04492b.

29. Kimber, D.P.; Pullar, R.C.; Alford, N.M.N. The effects of dielectric loss and tip resistance on resonator Q of the scanning evanescent microwave microscopy (SEMM) probe. *Meas. Sci. Technol.* **2008**, *19*, 2–6, doi:10.1088/0957-0233/19/11/115502.

30. European Central Bank Banknotes Denominations Available online: https://www.ecb.europa.eu/euro/banknotes/denominations/html/index.en.html#es2-020 (accessed on May 20, 2021).

31. Gao, C.; Xiang, X.D. Quantitative microwave near-field microscopy of dielectric properties. *Rev. Sci. Instrum.* **1998**, *69*, 3846–3851, doi:10.1063/1.1149189.

32. Gregory, A.P.; Blackburn, J.F.; Lees, K.; Clarke, R.N.; Hodgetts, T.E.; Hanham, S.M.; Klein, N. Measurement of the permittivity and loss of high-loss materials

using a Near-Field Scanning Microwave Microscope. *Ultramicroscopy* **2016**, *161*, 137–145, doi:10.1016/j.ultramic.2015.11.015.

33. Lu, G.M.; Feng, X.T.; Li, Y.H.; Zhang, X. The Microwave-Induced Fracturing of Hard Rock. *Rock Mech. Rock Eng.* **2019**, *52*, 3017–3032, doi:10.1007/s00603-019-01790-z.

34. Guo, L.; Lan, J.; Du, Y.; Zhang, T.C.; Du, D. Microwave-enhanced selective leaching of arsenic from copper smelting flue dusts. *J. Hazard. Mater.* **2020**, *386*, 121964, doi:10.1016/j.jhazmat.2019.121964.

Chapter 7

Conclusions

The thesis studies a series of devices for measuring dielectric properties adapted to different environments. The thesis work had covered some tasks for the correct development of the SEDMICRON project. This project aimed to the use of microwave technology to detect and authenticate markers in document security applications through a near-field scanning microwave microscope (NSMM). Thus, the main goal of the project and the thesis was to develop such a system and utilize it to detect markers in official documents, such as passports or banknotes. In parallel to this objective, a great effort was made to develop methods for the permittivity characterization of markers. This thesis aimed to go beyond this application and adapt some of these techniques to diverse environments and applications. The publications included in this thesis dissertation endorse the thesis work and cover all the objectives set for the development of this thesis. The most relevant results, developments, and advances obtained in this thesis dissertation are summarized below.

A versatile, standalone, portable, and easy-to-use device for complex permittivity characterization was developed.

- The device is based in a reentrant cavity with specific modifications to allow sensitive measurements of materials placed inside a pyrex tube.
- The system includes an affordable in-house reflectometer avoiding the use of more sophisticated and expensive vector network analyzer devices.
- The features of this design allow straightforward use by non-specialized personnel in a wide range of fields and scientific applications.

A specific test fixture was developed to perform temperature-dependent permittivity measurements of lossy food products.

- The coaxial cell allows sensitive measurements of lossy food products at RF frequencies at temperatures up to 120ºC.
- An uncertainty analysis exhibited the increased accuracy of the used cell compared to other approaches employed in the literature.
- The test fixture can withstand temperatures up to 120ºC.
- The analysis technique avoids the need for infinite flange assumptions and calibration with known liquids, the typical methodology of coaxial probes.

A Near Field Scanning Microwave Microscope at the micrometer scale was developed and employed in different environments.

- The NSMM device included all the necessary elements for standalone and portable performance: a near-field resonant probe; an XY positioning system; a laser to track the tip-to-sample distance; an in-house microwave reflectometer to generate and detect microwave signals; and a LabVIEW software to integrate all the subsystems and perform the calculations and representations.
- The viability of microwave technology for identifying markers in anti-counterfeiting applications was demonstrated.
- The advantages of the penetration depth of microwaves in detecting markers hidden behind dielectric or metallic layers were exhibited.
- The single frequency approach provided high-quality images in shorter measurement times. Thus, it is the preferable option for sensing applications.
- Permittivity maps of watermarks in banknotes were determined.
- The measurement capabilities of the developed NSMM were enhanced to allow contactless complex permittivity measurements thanks to a near-field probe with enhanced sensitivity and a combination of analysis techniques based on the cavity perturbation method of resonant cavities.
- Permittivity scans of rocks were obtained to demonstrate the applicability of this technology in the rock industry.

As described throughout this thesis dissertation, the scope of microwave sensors and dielectric characterization techniques is enormous and continues to grow. Many applications demand the continuous development of new microwave cells or the adaptation of existing probes to solve new challenges. Therefore, the future lines follow the journey started with this work, looking for new applications to use the described cells and developing new cells and devices adapted for diverse environments. In all these designs, we will continue to emphasize the development of portable and easy-to-use dielectric characterization systems adapted for a non-specialist audience in the field of dielectric characterization and microwave monitoring.

In addition, we will continue the dissemination work. First, we will submit for publication the work performed on the creation and validation of the single reentrant coaxial probe for broadband measurements of lossy materials inside tubes described in section 6.1. In addition, in the light of the potential proven by the developed systems, we intend to give a broader diffusion to those methods and their uses in congresses, new scientific publications, and web pages.

Chapter 8

List of Scientific Contributions

1. Gutiérrez, J.D.; Catalá-Civera, J.M.; Bows, J.; Peñaranda-Foix, F.L. Dynamic measurement of dielectric properties of food snack pellets during microwave expansion. *J. Food Eng.* **2017**, *202*, doi:10.1016/j.jfoodeng.2017.01.021.

2. Marques-Villarroya, D.; Penaranda-Foix, F.L.; Garcia-Banos, B.; Catala-Civera, J.M.; Gutierrez-Cano, J.D. Enhanced Full-Wave Circuit Analysis for Modeling of a Split Cylinder Resonator. *IEEE Trans. Microw. Theory Tech.* **2017**, *65*, doi:10.1109/TMTT.2016.2637932.

3. Marques-Villarroya, D.; Penaranda-Foix, F.L.; Garcia-Banos, B.; Catala-Civera, J.M.; Gutierrez-Cano, J.D. Fast and accurate determination of the complex resonant frequency of a multilayer circular cavity using Chebyshev's root-finder. *Prog. Electromagn. Res. M* **2017**, *58*, doi:10.2528/PIERM17020904.

4. Gutiérrez-Cano, J.D.; Catalá-Civera, J.M.; Bows, J.; Plaza-González, P.J.; Llorens-Vallés, G. Dielectric characterization of third generation snacks processed by microwave energy. In Proceedings of the 16th International Conference on Microwave and High Frequency Heating (AMPERE 2017); Delft (The Netherlands).

5. García-Baños, B.; Gutiérre-Cano, J.D.; Jiménez-Reinosa, J.; Fernández-Lozano, J.F. Evaluation of microwave susceptors performance through in situ dielectric characterization up to 1100ºC. In Proceedings of the 16th International Conference on Microwave and High Frequency Heating (AMPERE 2017); Delft (The Nederlands).

6. Marques-Villarroya, D.; Penaranda-Foix, F.; Garcia-Banos, B.; Catala-Civera, J.M.; Daniel Gutierrez-Cano, J. Analysis of an overmoded re-entrant cavity. In Proceedings of the Proceedings of the 47th European Microwave Conference; 2017.

7. Gutiérrez-Cano, J.D.; Hamilton, I.E.; Catalá-Civera, J.M.; Bows, J.; Peñaranda-Foix, F.L. Effect of water content on the dynamic measurement of dielectric properties of food snack pellets during microwave expansion. *J. Food Eng.* **2018**, *232*, doi:10.1016/j.jfoodeng.2018.03.018.

8. Gutiérrez-Cano, J.D.; Catalá-Civera, J.M.; Plaza-González, P.; Llorens-Vallés, G.; Peñaranda-Foix, F.L. Estudio de la geometría de una apertura coaxial para su uso en un microscopio por microondas escáner en campo próximo. In Proceedings of the XXXIII SIMPOSIUM NACIONAL DE LA UNIÓN CIENTÍFICA INTERNACIONAL DE RADIO (URSI 2018); Granada (Spain).

9. Llorens-Vallés, G.; Manno, R.; Sebastián, V.; Mallada, R.; Santamaría, J.; Marín,

A.J.C.; José D. Gutiérrez-Cano Dielectric properties changes during microwave heating of reagents for the synthesis of silver nanoparticles. In Proceedings of the 17th International Conference on Microwave and High Frequency Heating (AMPERE 2019); Valencia (Spain).

10. Gutiérrez-Cano, J.D.; Buendía, Á.L.; Urquiola, M.; Catalá-Civera, J.M. Petrography analysis using a Near-Field Scanning Microwave Microscope. In Proceedings of the 17th International Conference on Microwave and High Frequency Heating (AMPERE 2019); Valencia (Spain).

11. Gutierrez-Cano, J.D.; Plaza-Gonzalez, P.; Canos, A.J.; Garcia-Banos, B.; Catala-Civera, J.M.; Penaranda-Foix, F.L. A New Stand-Alone Microwave Instrument for Measuring the Complex Permittivity of Materials at Microwave Frequencies. *IEEE Trans. Instrum. Meas.* **2020**, *69*, 3595–3605, doi:10.1109/TIM.2019.2941038.

12. Alvarez, J.O.; Penaranda-Foix, F.L.; Catala-Civera, J.M.; Gutierrez-Cano, J.D. Permittivity Spectrum of Low-Loss Liquid and Powder Geomaterials Using Multipoint Reentrant Cavities. *IEEE Trans. Geosci. Remote Sens.* **2020**, *58*, doi:10.1109/TGRS.2019.2948052.

13. Gutiérrez-Cano, J.D.; Catalá-Civera, J.M.; Plaza-González, P.J.; Peñaranda-Foix, F.L. Detection of anti-counterfeiting markers through permittivity maps using a micrometer scale near field scanning microwave microscope. *Sensors* **2021**, *21*, doi:10.3390/s21165463.

14. Gutiérrez-Cano, J.D.; Catalá-Civera, J.M.; López-Buendía, A.M.; Plaza-González, P.J.; Penaranda-Foix, F.L. High-Resolution Detection of Rock-Forming Minerals by Permittivity Measurements with a Near-Field Scanning Microwave Microscope. *Sensors* **2022**, *22*, doi:10.3390/s22031138.

15. Penaranda-Foix, F.L.; Catala-Civera, J.M.; Gutierrez-Cano, J.D.; Garcia-Banos, B. Directional Coupler Calibration for Accurate Online Incident Power Measurements. *IEEE Microw. Wirel. Components Lett.* **2021**, *31*, doi:10.1109/LMWC.2021.3070788.

16. Gutiérrez-Cano, J.D.; Catalá-Civera, J.M.; Penaranda-Foix, F.L.; Plaza-González, P.J. Improved open-ended coaxial probe for temperature-dependent permittivity measurements of foodstuff at radio frequencies. *J. Food Eng.* **2022**, *316*, doi:10.1016/j.jfoodeng.2021.110823.

17. Peñaranda-Foix, F.L.; Catalá-Civera, J.M.; Gutiérrez-Cano, J.D.; García-Baños, B. On-line power measurements with directional coupler. In Proceedings of the 18th International Conference on Microwave and High Frequency Heating (AMPERE 2021); Gothenburg (Sweden).